STARS

Electronic Theses and Dissertations, 2004-2019

2018

A Modeling Framework of Brittle and Ductile Fractures Coexistence in Composites

Yangyang Qiao
University of Central Florida

A MODELING FRAMEWORK OF BRITTLE AND DUCTILE FRACTURES

COEXISTENCE IN COMPOSITES

by

YANGYANG QIAO

M.S. University of Central Florida, 2015

B.S. Hohai University, China, 2012

A dissertation submitted in partial fulfillment of the requirements
for the degree of Doctor of Philosophy
in the Department of Mechanical and Aerospace Engineering
in the College of Engineering and Computer Science
at the University of Central Florida
Orlando, Florida

Spring Term
2018

Major Professor: Yuanli Bai

ABSTRACT

In order to reduce the weight of automobiles and aircrafts, lightweight materials, such as aluminum alloy, advanced high strength steel, composite materials, are widely used to replace the traditional materials like mild steel. Composite materials are complicated in material mechanical properties and less investigated compared to metallic materials. Engineering composites can be categorized into polymer matrix composites (PMCs), metal matrix composites (MMCs) and ceramic matrix composites (CMCs) according to their matrix materials.

A set of mechanical experiments ranging from micro scale (single fiber composite and thin film composite) to macro scale (PMCs and MMCs) were conducted to fully understand the material behavior of composite materials. Loading conditions investigated includes uniaxial tension, three-point bending, uniaxial compression, simple shear, tension combined with shear, and compression combined with shear.

For single fiber composite and thin-film composite, details of each composition are modelled. For the PMCs and MMCs which have plenty of reinforcements like fibers and particles, the details of the composition of structures cannot be modelled due to the current limitations of computing power. A mechanics framework of composite materials including elasticity, plasticity, failure initiation and post failure softening is proposed and applied to two types of composite materials.

Uniaxial tension loading is applied to several single fiber composites and thin film composites. A surprising phenomenon, controllable and sequential fragmentation of the brittle fiber to produce uniformly sized rods along meters of polymer cladding, rather than the expected random or

chaotic fragmentation, is observed with a necking propagation process. A combination of necking propagation model, fiber cracking model and interfacial model are proposed and applied to the finite element simulations. Good predictions of necking propagation and uniform fragmentation phenomenon are achieved. This modeling method of the micro-scale phenomenon reveals the physics inside composites in micro scale and helps the understanding of the process of nano fragmentation.

Unidirectional carbon fiber composites were tested under multi-axial loading conditions including tensile/compression/shear loadings along and perpendicular to the fiber direction. Compression dominated tests showed a brittle fracture mode like local kicking/buckling, while tension dominated tests showed a fracture mode like delamination and fiber breakage. Simple shear tests with displacement control showed matrix material hardening and softening before total failure. The proposed modeling framework is successfully applied to the PMCs. A new parameter ψ was introduced to represent different loading conditions of PMCs. Numerical simulations using finite element method well duplicated the anisotropic elasticity and plasticity of this material. Failure features like delamination was simulated using cohesive surface feature. It is also applied to carbon fiber composite laminates to further validate the proposed model.

A round of experimental study on high volume fraction of metallic matrix nano composites was conducted, including uniaxial tension, uniaxial compression, and three-point bending. The example materials were two magnesium matrix composites reinforced with 10 and 15% vol. SiC particles (50nm size). Brittle fracture mode was exhibited under uniaxial tension and three-point bending, while shear dominated ductile fracture mode (up to 12% fracture strain) was observed under uniaxial compression. Transferring the Modified Mohr Coulomb (MMC) ductile fracture

model to the stress based MMC model (sMMC), the proposed modeling framework is applied to this material. This model has been demonstrated to be capable of predicting the coexistence of brittle and ductile fracture modes under different loading conditions for MMCs. Numerical simulations using finite element method well duplicated the material strength, fracture initiation sites and crack propagation modes of the Mg/SiC nano composites with a good accuracy.

KEYWORDS: Composites Modeling Framework, Unsymmetric Elasticity, Coexistence of Brittle and Ductile Fractures, Finite Element Analysis, Single Fiber Composites, Polymer Matrix Composites, Metal Matrix Composites

ACKNOWLEDGMENTS

Finally, I would express my deepest gratitude to my family and friends for their support in this memorable journey.

TABLE OF CONTENTS

LIST OF FIGURES

xiii

LIST OF TABLES

CHAPTER 1 INTRODUCTION

1.1 Composites Overview

In recent years, global warming and climate change has drawn great attention. It is found that greenhouse effect should be responsible for this issue. The greenhouse effect is the process by which absorption and emission of infrared radiation by gases in a planet's atmosphere warm its lower atmosphere and surface. Human activity since the Industrial Revolution has increased the amount of greenhouse gases in the atmosphere, leading to increased radiative forcing from CO_2, methane, tropospheric ozone and nitrous oxide. Governments have taken actions to reduce the fossil fuel usage and the Corporate Average Fuel Economy (CAFE) standards have been enacted by U.S. Congress. In order to reduce the weight of automobile and aircraft, lightweight materials, such as aluminum alloy, high strength steel, composite material, are widely used as lightweight materials to replace the traditional materials like mild steel (Jambor & Beyer, 1997; Jia & Bai, 2016a, 2016b; Jia, Long, Wang, & Bai, 2013).

Composite materials find increasing applications in automobile and aircraft industries due to their material properties. Composites materials are usually stronger, lighter or less expensive compared to traditional materials and composites can achieve properties that are not available for single phase materials (Berthelot, 2012; P. Liu & Zheng, 2010; Wang, Jiang, Zhou, Gou, & Hui, 2017; Wang, Sparkman, & Gou, 2017; wang, xu, Zhou, & Gou, 2017) Composite can be categorized into polymer matrix composites (PMCs), metal matrix composites (MMCs) and ceramic matrix composites (CMCs) according to their matrix material. Compared to metals, composites have many advantages. Generally speaking, composites are light in weight compared

to metals. In addition, composites can be designed to be far stronger than aluminum or steel. Therefore, composites have the highest strength-to-weight ratios in structures today. Composites have high corrosion resistance which resist damage from the weather and from harsh chemicals. High impact strength of composites leads to the usage in bulletproof vests and panels. Composites can be molded into complicated shapes more easily than most other materials which indicates design flexibility. Other advantages like dimensional stability, radar transparent, low thermal conductivity and less maintenance greatly enlarges their range of application (Canaday, 2015; Chawla, 2012; CompositesGroup).

In order to better apply the composites materials into industry, tough challenges need to be overcome. One of the most complicated problems is the failure mechanisms which are quite different from metallic materials. Lots of researchers have been dedicated to developing models for predicting the behavior of composites especially failure features. The following sections are brief introductions of the composites modeling methods. The materials studied are single fiber composite (SFC), thin-film composite (TFC), polymer matrix composites (PMCs) and metal matrix composites (MMCs).

1.2 Single Fiber Composite and Thin-film Composite

The single-fiber composite test is an important method in both the theoretical and experimental study of the failure process in fibrous composites (Shia, Hui, & Phoenix, 2000). In such a test, a single brittle fiber is embedded in ductile matrix. The matrix usually has a much larger cross-sectional area and larger strain to failure than the fiber. As the overall strain increased in the SFC specimen, the fiber fails progressively and randomly along the fiber into small segments. The SFC tests has many applications in determining the material properties. One is to estimate the

respective Weibull shape and scale parameters for the strength of fibers (Clough & McDonough, 1996; Shioya & Takaku, 1995). Another is to estimate the interfacial shear strength (Fraser, Ancker, DiBenedetto, & Elbirli, 1983; Netravali, Henstenburg, Phoenix, & Schwartz, 1989; Zhandarov, Pisanova, & Dovgyalo, 1992).

Statistical theories for the SFC test have been developed and most of the statistical theories developed for fiber fragmentation in an SFC are based on simple shear-lag model of Cox (1952), considering a constant interfacial shear stress τ inside the fiber unloading zone. The constant interfacial shear stress assumption works for some cases (Hui, Shia, & Berglund, 1999). However, it cannot adequately reflect observed features from experimental (Drzal & Rich, 1985; Netravali, Schwartz, & Phoenix, 1989; Ohsawa, Nakayama, Miwa, & Hasegawa, 1978; Varna, Joffe, & Berglund, 1996).

Conditions beyond the assumption of constant interfacial shear stress take place around the breaking areas (Figure 1). As the applied stress is increased on an SFC, a matrix yield zone will develop and propagates near a break as a thin hollow cylinder around the fiber. A debond zone will form afterwards along the interface with increasing strain. These phenomena have been studied using plasticity model and finite simulations (A. Johnson, Hayes, & Jones, 2005; Okabe, Takeda, Kamoshida, Shimizu, & Curtin, 2001). In addition, sometimes a transverse matrix crack can be formed around a break (Netravali, Henstenburg, et al., 1989). This phenomenon is usually not considered since it makes the condition more complex.
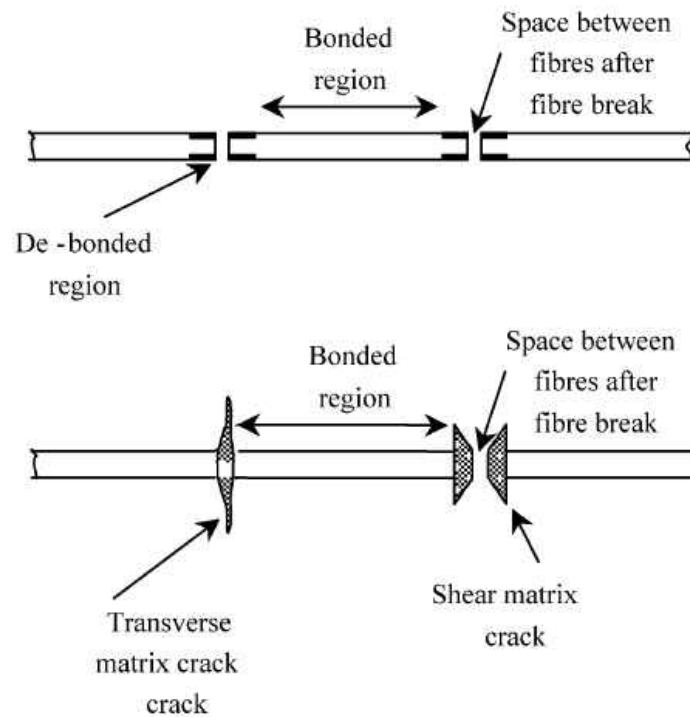
Figure 1: Different types of failure modes accompanying fiber fracture in a single fiber fragmentation test (reprint from (A. Johnson et al., 2005))

Film fragmentation is an extension of fiber fragmentation in a 2D plane (Figure 2). For film fragmentations, the general configuration involves a brittle film adhered on a ductile substrate. With increasing applied strain, the brittle film fails progressively producing an increasing number of strips. Film, substrate and interface properties greatly influence this process.
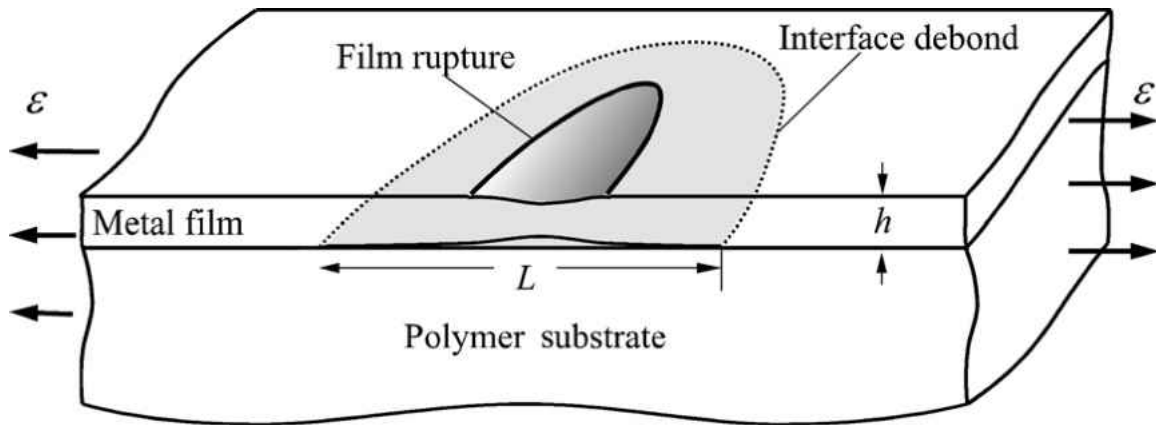
Figure 2: A film fragmentation process showing film necking and the interfacial debonding (reprint from (T. Li & Suo, 2007))

For the behavior of brittle films, the effects of grain boundary adhesion, grain size and film thickness on ductility and failure strain of film are reported (Lu, Suo, & Vlassak, 2010; Z. Zhang & Li, 2008). For the ductile substrate, the phenomena like plastic yielding, residual strain and residual stress have been investigated (Beuth & Klingbeil, 1996; B. Chen, Hwang, Yu, & Huang, 1999; Yanaka, Tsukahara, Nakaso, & Takeda, 1998). Film/substrate interface plays an important role in the process of film cracking. Experimental methods on measuring interfacial properties have been studied by many researchers (Bagchi, Lucas, Suo, & Evans, 1994; Volinsky, Moody, & Gerberich, 2002). Analytical models and finite element analysis have been used to study the interfacial shear stress (B. Chen, Hwang, Chen, Yu, & Huang, 2000; T. Li et al., 2005). Film rupture strain is shown to be dependent on adhesion of the metal/polymer interface (T. Li & Suo, 2007; Xiang, Li, Suo, & Vlassak, 2005).

To summarize, the film fragmentation research is more focused on the parameters influencing fragmentation process like the film properties, substrate geometry and interface compliance. A model considering all the above effects is absent which could be a direction for more research.

5

Geometry bring in more complexity into this area and therefore more complexity of the physics lying under the film fragmentation.

1.3 Polymer Matrix Composites

Polymer matrix composites (PMCs) materials have been used as aircraft primary structures due to their good performance. It is reported that more than 50% of the primary structure of the Boeing 787 Dreamliner is made of carbon fiber reinforced plastic and other composites (Company, 2008). Carbon fiber composites have advantages over metals in many aspects. High strength to weight ratio is one of the most valuable advantages since it reduces weight and therefore increases fuel efficiency. Good corrosion resistance is another one which requires less maintenance. In addition, PMCs also have high impact strength which absorb more impact energies. Moreover, composites have longer durability since they show good fatigue properties. However, there are still tough challenges in the industrial applications of PMCs. One of the most complicated problems is the failure mechanisms which are quite different from metallic materials.

The failure mechanisms of PMCs are complex because the modes of failure depend upon stress state, specimen geometry, fiber direction, material property and manufacturing defects. In addition, local failure initiations, which followed by damage evolution, occur way before final failure. During the stage of damage evolution, the material can still sustain more load before catastrophic fracture, which introduces more difficulties to the failure theories. Lots of researchers have been dedicated to developing models for predicting the behavior of PMCs especially failure features.

The modeling of PMCs behavior can be classified into several catalogs, which include failure criterion method, continuum damage mechanics method and plasticity method. The failure criterion method mainly considers the initial or final failure locus of PMCs while the continuum damage mechanics method takes degradation of modulus into account. The plasticity method considers the material non-linearity to be plasticity.

Some phenomenological failure criteria describing initial failure of composite laminate have been postulated based on material strength. Some of the most known ones are Maximum stress/strain, Tsai-Hill (Tsai, 1968), Hoffman (Hoffman, 1967), Franklin-Marin (Franklin, 1968), Tsai-Wu (Tsai & Wu, 1971) and Hashin (Hashin & Rotem, 1973) criteria. These criteria can be further classified into two groups, non-interactive failure criteria and interactive criteria. If a criterion has no interaction between stress or strain components, it is defined as a non-interactive failure criterion which compares individual stress or strain component with the corresponding material strength. The maximum stress/strain criterion is one of non-interactive failure criteria which has lower accuracy. On the contrary, most of the phenomenological criteria like Tsai-Hill, Hoffman, Franklin-Marin, Tsai-Wu and Hashin belong to interactive failure criteria, which have more parameters and with higher accuracy. Failure criteria can also be classified based on whether it is associated with failure modes or not. Some of the failure criteria utilize stress or strain polynomial expressions to describe the failure locus, such as Tsai-Hill, Tsai-Wu and Hoffman. These criteria did not distinguish between different failure modes. Other criteria like maximum stress/strain, Hashin, Yamada and Sun (1978), Hart-Smith (H. T. Hahn & Tsai, 1973) and Puck (Puck & W, 1969) specify particular failure modes for different loading conditions.

Continuum damage mechanics (CDM) models are based on the observation that as the failure evolution of fiber reinforced composites, continuous stiffness degradation is shown in materials. CDM uses internal variables to describe the progressive loss of rigidity. Kachanov (1958) firstly developed a continuum damage mechanics framework to study the creep rupture of metals. Schapery (1990), Murakami and Kamiya (1997), Hayakawa, Murakami, and Liu (1998), Olsson and Ristinmaa (2003) and Maimí, Camanho, Mayugo, and Dávila (2007). proposed stiffness degradation and damage evolution models using a second or fourth order damage tensor. The damage tensors are related to damage mechanisms and dissipation energy which controls the evolution of damage state. Kwon and Liu (1997), Matzenmiller, Lubliner, and Taylor (1995), Schipperen (2001), Maa and Cheng (2002) and Camanho, Maimí, and Dávila (2007) proposed thermodynamic models to describe the progressive failure properties. These thermodynamic models were limited to plane structures. Pinho, Iannucci, and Robinson (2006) proposed a three-dimensional failure criterion for laminated fiber-reinforced composites based on the physical model for each failure mode. Donadon, De Almeida, Arbelo, and de Faria (2009) developed a fully three-dimensional failure model to predict damage in composite structures subjected to multi-axial loading.

The plasticity method is mainly used for composite materials that exhibit ductile behavior like boron/aluminum, graphite/PEEK and other thermoplastic composites. Vaziri, Olson, and Anderson (1991) proposed an orthotropic plane stress material model that combines the classical flow theory of plasticity with a failure criterion. Vyas, Pinho, and Robinson (2011) presents an elasto-plastic model framework which incorporated a non-associative flow rule for unidirectional plies. A 3-D plastic potential function was proposed to describe the nonlinear behavior in

anisotropic fiber composites by Sun and Chen (1989). Xie and Adams (1995) developed a three-dimensional plasticity model to describe the plastic response of unidirectional composites. A three-dimensional finite element analysis demonstrated the application of Xie and Adams's model on compression and short-beam shear tests. Car, Oller, and Oñate (2000) proposed a generalized anisotropic elasto-plastic constitutive model for large strain analysis of fiber-reinforced composite with the frame of mixing theories.

P. Liu and Zheng (2010) pointed out that the elastic/damage coupling constitutive model may be insufficient in order to accurately describe the damage initiation and evolution of laminated fiber-reinforced composites. Some damage/plasticity coupled nonlinear models were also introduced to describe the interactive effect of plastic deformations with damage properties. Chow and Yang (1997) outlined a constitutive model for mechanical response in inelastic composite materials due to damage. Lin and Hu (2002) developed an elasticity-plasticity/damage coupled constitutive model together with a mixed failure criterion for single lamina. Barbero and Lonetti (2002) also presented a damage/plasticity model for an individual lamina and then assembled it to describe the behavior of polymer matrix composite laminates.

Delamination is an important mode of failure inside a ply or between plies. Numerous number of criteria have been proposed to predict the initiation and propagation of delamination. These criteria use different combinations of transverse tension, shear and sometimes tension along fiber direction, in a linear or quadratic form. Maximum stress criterion sets transverse tensile strength, and two shear strengths as the limit to predict failure initiation. Hashin (1980) used a quadratic form that incorporated the transverse tensile stress and two shear stresses. Lee (1982) proposed a model similar to maximum stress criterion which combines two shear stresses in a quadratic

9

form. Brewer and Lagace (1988) utilized compressive stress as well to predict the delamination initiation. Tong (1997) included tensile stress along fiber direction in either linear or quadratic forms. Curve fitting was also introduced in delamination prediction by Goyal, Johnson, and Davila (2004).

Delamination propagation is another concern in model prediction. Criteria have been proposed mainly based on the three crack separation modes and their corresponding critical strain energy release rate G_c. The simplest mode assumes no interaction between three crack separation modes and that delamination grows when any one of the three strain energy release rate reaches its corresponding limit (Orifici, Herszberg, & Thomson, 2008). H. Hahn (1983) proposed a criterion which considers the interaction between mode I and mode II crack. H. Hahn and Johannesson (1984), Donaldson (1985), Hashemi, Kinloch, and Williams (1990) and Benzeggagh and Kenane (1996) incorporated parameters which need curve fitting to describe the delamination propagation.

World-Wide Failure Exercises (WWFE) (M. J. Hinton, Kaddour, & Soden, 2004) have been conducted to evaluate the postulated models. Plenty of models have been applied to predict the failure of fiber-reinforced-polymer composites. It is recognized that there is no universal definition for what constitutes failure initiation of a composite structure. Very few current failure theories can be considered to be credible for practical engineering applications.

<u>1.4</u> <u>Metal Matrix Composites</u>

It is well known that mechanical properties of metallic materials can be effectively enhanced by incorporating hard nano ceramic particles to form so-called metallic matrix nano composites

(MMNCs). MMNCs have attracted great engineering interest for decades because of their super material properties, for example high strength and light weight, low coefficient of thermal expansion, etc. (I.A. Ibrahim, F.A. Mohamed, & E.J. Lavernia, 1991; Lloyd, 1994; Miracle, 2005; Mortensen & Llorca, 2010). In particular, particulate-reinforced lightweight metal matrix (e.g. aluminum and magnesium) composites have attracted extensive attention because of their potential applications in automotive, aerospace, and defense industries (Ashby, 1971; Clyne & Withers, 1995; Fishman, 1986; Flom & Arsenault, 1985; I. A. Ibrahim, F. A. Mohamed, & E. J. Lavernia, 1991). Mechanical behavior of MMNCs is determined by their microstructural parameters such as the size (d) and the volume fraction (f_v) of the particles, and inter-particle spacing (λ). These three parameters are not independent, but related to each other through (Ravichandran, 1994)

$$\lambda = d\left(\frac{1}{f_v^{1/3}} - 1\right). \tag{1}$$

This relationship can be graphically described (see Figure 3)(Prabhu, Suryanarayana, An, & Vaidyanathan, 2006). According to their microstructural features, MMNCs can be classified into three fundamentally different categories, as marked as areas 1, 2 and 3 in Figure 3. Previous work on MMNCs was primarily focused on the materials in area 1, where large ceramic particles (a few to a couple of hundred micrometers) were used as reinforcements (Arsenault & Shi, 1986; Arsenault, Wang, & Feng, 1991; Flom & Arsenault, 1985; Gustafson, Panda, Song, & Raj, 1997; Hong, Kim, Huh, Suryanarayana, & Chun, 2003; Kamat, Rollett, & Hirth, 1991; Kouzeli & Mortensen, 2002; Kouzeli, Weber, Marchi, & Mortensen, 2001; Mummery & Derby, 1991; Nan & Clarke, 1996; Prangnell, Downes, Stobbs, & Withers, 1994; Shi & Arsenault, 1994), thus the resultant inter-particle spacing λ was also at micrometer scale. These materials showed much

higher yield strength, but poorer ductility and lower fracture toughness than monolithic alloys. It has been well understood that the reinforcing mechanism of these materials was due to the geometrical necessary dislocations (GND) resulting from the difference in the coefficient of thermal expansion between the metal matrix and ceramic reinforcements (Flom & Arsenault, 1985; Kouzeli & Mortensen, 2002). On the other hand, the materials in area 2 have also been studied by several groups (Hesabi, Simchi, & Reihani, 2006; Kang & Chan, 2004; X. Li, Yang, & Weiss, 2008; Mula, Padhi, Panigrahi, Pabi, & Ghosh, 2009; Tang, Hagiwara, & Schoenung, 2005; Wu & Li, 2000; Yang, Lan, & Li, 2004; Yang & Li, 2007; Yar, Montazerian, Abdizadeh, & Baharvandi, 2009; H. Zhang, Maljkovic, & Mitchell, 2002). For these materials, a small amount (<5 vol.%) of nanometer-sized particles (<100 nm) was used as the reinforcements; the resultant inter-particle spacing is at nanometer scale, but much larger than the particle size d. Compared to the materials in area 1, the materials in area 2 not only showed improvement in yield strength, but also exhibited relatively good ductility with fracture strains of up to 8% (Kang & Chan, 2004; Yang & Li, 2007). Several reinforcing mechanisms were identified for the materials including grain refinement, Taylor effect, and Orowan strengthening, with a major contribution from Orowan pinning effect (Kang & Chan, 2004).
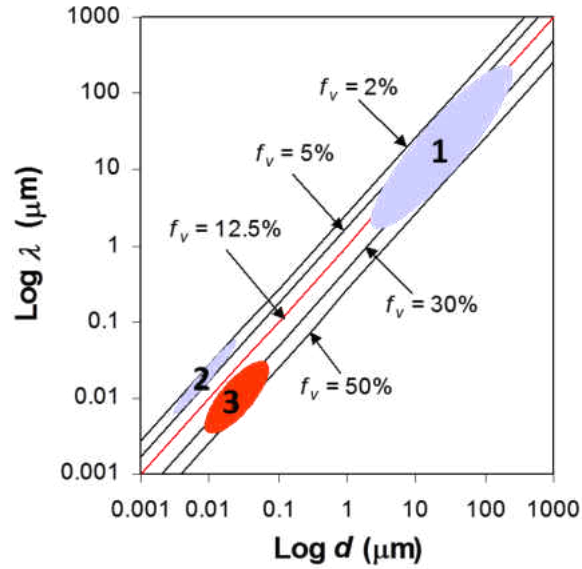
Figure 3: Relationship between inter-particle spacing (λ), particle size (d) and volume fraction (f_v) of the reinforcement phase, based on Eq. (1). Note that at volume fractions greater than 12.5% (red line), λ becomes smaller than d.

However, the composites in area 3, which contain a high volume fraction (>12.5 vol.%) of nano-sized reinforcements (<100 nm), have not been well investigated yet. Compared to materials in areas 1 and 2, the materials in area 3 possess a unique microstructure, where the inter-particle spacing is not only at nanometer scale, but also less than the particle size itself. Some results revealed that this new class of materials could exhibit unique and superior properties as compared to their counterparts in areas 1 and 2. For example, aluminum reinforced with 15 vol.% of 50 nm alumina particles showed excellent wear resistance with wear rate even lower than stainless steel (An et al., 2011). The new material of Mg/SiC nano composite around area 3 will be studied in this paper.

Accurate characterization of plasticity and fracture for nano composites is a necessary step when these materials go to application. It is known that an arbitrary stress tensor $[\sigma_{ij}]$ can be simplified to three principal stresses ($\sigma_1, \sigma_2, \sigma_3$) by coordinate system rotation. It has been shown that a

13

stress direction or loading condition can be uniquely described by two dimensionless parameters, stress triaxiality η (mean stress σ_m normalized by equivalent stress $\bar{\sigma}$) and Lode angle parameter $\bar{\theta}$ (the normalized third deviatoric stress invariant), which are defined as follows (Bai & Wierzbicki, 2008).

$$\eta = \frac{\sigma_m}{\bar{\sigma}} \tag{2}$$

$$\bar{\theta} = 1 - \frac{2}{\pi}\arccos\left(\left(\frac{r}{\bar{\sigma}}\right)^3\right) \tag{3}$$

Here, r is the third invariant of the deviatoric stress tensor $[S] = [\sigma] - \sigma_m[I]$, and

$$r = \left(\frac{9}{2}[S] \cdot [S]:[S]\right)^{1/3} = \left[\frac{27}{2}(\sigma_1 - \sigma_m)(\sigma_2 - \sigma_m)(\sigma_3 - \sigma_m)\right]^{1/3}. \tag{4}$$

Uniaxial tension or compression were often used to study the mechanical properties of MMNCs, for example $A359/SiC_p$ composites (Y Li, Ramesh, & Chin, 2000; Yulong Li, Ramesh, & Chin, 2004) and copper/carbon nanotube composites (Barai & Weng, 2011; Kyung Tae Kim, Cha, Hong, & Hong, 2006; K. T. Kim, Eckert, Menzel, Gemming, & Hong, 2008; Long, Bai, Algarni, Choi, & Chen, 2015). Vasudevan, Richmond, Zok, and Embury (1989) experimentally investigated the pressure dependence on material plasticity for 2014 Al/SiC composites. It was found that this composite has higher flow stress in compression than tension. It was also shown that the material stress-strain curves were increased under confined hydrostatic pressures in tensile tests. Large amount of strength difference among tension, compression and other loading conditions were also confirmed (H. Zhang, Ramesh, & Chin, 2005) using unit cell finite element simulation. For MMNCs, damage/fracture mechanism like brittle cracking of the particles, decohesion at the interface of particle and matrix and failure of the matrix were studied in details

with this representative volume element method (Shao, Xiao, Wang, Ma, & Yang, 2011; Xu & Qu, 2015; Yuan, Yang, Li, Heng, & Li, 2012). The test data of Vasudevan et al. (1989) were revisited by H. Zhang, Ramesh, and Chin (2008) using the Mises-Schleicher model (Mises, 1913; Schleicher, 1926), which considers the effect of hydrostatic pressure on material yielding. Azizi, Legarth, and Niordson (2013) derived an anisotropic pressure dependent yield function based on strain gradient plasticity. An associated and decomposed flow rule was postulated to determine the deviatoric and dilatational deformation (H. Zhang et al., 2008). Lei and Lissenden (2007) studied the pressure sensitive 6092 Al/SiC composites using the Drucker-Prager yield function and a non-associated Prandtl-Reuss flow rule. All the research above has shown the pressure dependence on yield locus of MMNCs.

In ductile fracture/damage mechanics of uncracked bodies, the equivalent plastic strain to fracture ($\bar{\varepsilon}_f$) can be used as a measurement of material ductility. If the stress states are described by two dimensionless parameters (η and $\bar{\theta}$) stated above, then the material fracture limit will be a function of these two parameters, which naturally becomes a 3D fracture locus $\bar{\varepsilon}_f(\eta, \bar{\theta})$. The dependence of fracture strain on stress triaxiality has been investigated in the community of fracture mechanics for decades. Theoretical analysis attributes this phenomenon to void growth, nucleation, coalescence and linkage (A. L. Gurson, 1975; A.L. Gurson, 1977; McClintock, 1968; Rice & Tracey, 1969; Viggo Tvergaard, 1989; Viggo Tvergaard & Hutchinson, 2002; V. Tvergaard & Needleman, 1984). An extended Gurson-Tvergaard-Needleman (GTN) model is proposed with an improvement within low level of stress triaxiality(Malcher, Pires, & De Sá, 2014). Another extension of GTN model has been proposed to predict the pressure dependency of the limit stress for porous metals(Fritzen, Forest, Böhlke, Kondo, & Kanit, 2012). Several

criteria including continuum damage mechanics based Lemaitre model and GNT model are applied into numerical simulations and evaluated (H. Li, Fu, Lu, & Yang, 2011). The size effect on ductile fracture in micro-scaled plastic deformation has been studied (Ran, Fu, & Chan, 2013). Void growth and coalescence in ductile material is studied with a two stage strain hardening (Lecarme, Tekog, & Pardoen, 2011). It was determined that ductile fracture is affected by the hydrostatic pressure. Numerous tensile test results on smooth/notched round bar specimens supported this theory (Hancock & Mackenzie, 1976; G. R. Johnson & Cook, 1985). Micro-mechanical studies have been conducted to cover a wide range of stress triaxialities and Lode parameters (Brünig, Gerke, & Hagenbrock, 2013). The classical Mohr-Coulomb criterion was used to describe fracture of brittle materials (rock, concrete, soil, etc.). This model was transferred and extended to the mixed space of stress invariant and equivalent strain to describe ductile fracture (Bai & Wierzbicki, 2010), which is called the modified Mohr-Coulomb (MMC) model. This model includes not only both stress triaxiality and Lode angle dependence on fracture strain, but also gives their coupling effect. Many applications have proved the predicting capability of this model (Beese, Luo, Li, Bai, & Wierzbicki, 2010; Yaning Li, Luo, Gerlach, & Wierzbicki, 2010; Yaning Li, Wierzbicki, Sutton, Yan, & Deng, 2011; Luo, Dunand, & Mohr, 2012; Luo & Wierzbicki, 2010).

1.5 Outline of the Thesis

The thesis will consist of eight chapters. Chapter 1 is an introduction to the previously conducted research in the area of composite material modeling, including single fiber composites, polymer matrix composites and metal matrix composites.

Chapter 2 explains the experimental methods applied to different composites with various size and composition. For single fiber composites, cold-drawing or uniaxial tension loading condition is applied and an interesting phenomenon is observed. For unidirectional carbon fiber composites, biaxial loading conditions are applied to reveal the material behavior in tensile, compressive and shear conditions. For metal matrix composites, three loading conditions are applied.

Chapter 3 introduces the proposed theoretical framework for the material modeling of composite material. The framework involves elasticity, plasticity, damage initiation and post-failure softening stages.

Chapter 4 explains the application of the framework in the single fiber composites. Several individual material models are applied to reproduce the phenomenon observed in experiment.

Chapter 5 is the application of the framework into polymer matrix composites. Cohesive surface method is applied to reproduce the delamination behavior of the material.

Chapter 6 is a summary of applying the framework into metal matrix composites. A stress based MMC model (sMMC) is applied to model the fracture of metal matrix composites.

Chapter 7 is a validation of the proposed material modeling framework. The framework is applied to composite laminates. The experimental data is obtained from literature and good correlation between experiment and simulation is achieved.

Chapter 8 summaries the contributions of the present thesis and describes the recommended research in the future.

1.6 List of Related Papers Published, Submitted or in Preparation

- Yangyang Qiao, Chiara Bisagni, Yuanli Bai, "Experimental investigation and numerical simulation of unidirectional carbon fiber composite under multi-axial loading". Composite Part B: Engineering **124** (2017): 190-206.

- Soroush Shabahang, Guangming Tao, Joshua J. Kaufman, Yangyang Qiao, Lei Wei, Thomas Bouchenot, Ali P. Gordon, Yoel Fink, Yuanli Bai, Robert S. Hoy, and Ayman F. Abouraddy, "Controlled fragmentation of multimaterial fibers and films via polymer cold-drawing", Nature, June 2016.

- Yangyang Qiao, Jinling Liu, Yueqian Jia, Chengying Xu, Linan An and Yuanli Bai, "Study on coexistence of brittle and ductile fractures in nano reinforcement composites under different loading conditions." International Journal of Fracture (2017): **204** (2): 205-224.

- Yangyang Qiao, Yuanli Bai, "A Review on Fiber Reinforced Composites Failure Modelling Method", Journal of Automotive Safety and Energy, accepted for publication, March 2018.

CHAPTER 2 EXPERIMENT METHODS AND RESULTS

2.1 Single Fiber Composite and Thin-film Composite

A set of SFC and TFC tests have been done by Dr. Abouraddy's group. The SFC consist of a 20-μm-diameter glass core (e.g., the inorganic chalcogenide glass As_2Se_3) embedded in a 1-mm-diameter polymer cladding (the thermoplastic polymer polyethersulfone, PES). A series of core materials have been tested with the PES cladding by Dr. Gordon's group. The stress-strain curves of the materials are shown in Figure 4.

At room temperature, the core is brittle while the polymer is ductile. At a few percent of uniaxial extension, necks form locally and propagate until the fiber is fully drawn. The core is initially intact along the fiber axis and with the necking propagation, the glassy core fragments into an orderly sequence into a periodic train of cylindrical rods. As the necking propagation, the core continues to fragment until they consume the whole length of the fiber, or the applied stress is removed. The process is shown in Figure 5.

TFC tests have also been done with similar phenomenon. The width of the flat fiber is around 1 mm. The thickness of the continuous As_2Se_3 film and polymer matrix are 300 nm and 350 µm. In the flat-fiber geometry, the thin brittle film is embedded in a flat fiber. The propagation of the rectangular shoulder upon necking leads to the fragmentation of the film into parallel strips. The process is shown in Figure 6.

In addition to the simple geometries above, some complicated geometries were also utilized in the cold-drawing process. The procedure extends to scenarios where a large number of cores are embedded in a single polymer fiber. All of the cores simultaneously undergo fragmentation into

uniformly sized rods. In addition, hollow cylinders were also utilized in this process and could tune the $\bar{L}/D$ ratio of As_2Se_3 from 6 for a solid core to 4.5 and 3.2 when the hollow cylinder shell outer-to-inner-diameter ratio is 4 and 1.5, respectively. What's more, complex cross sections are used like triangle and combination of two materials. The geometries of the core materials are shown in Figure 7.
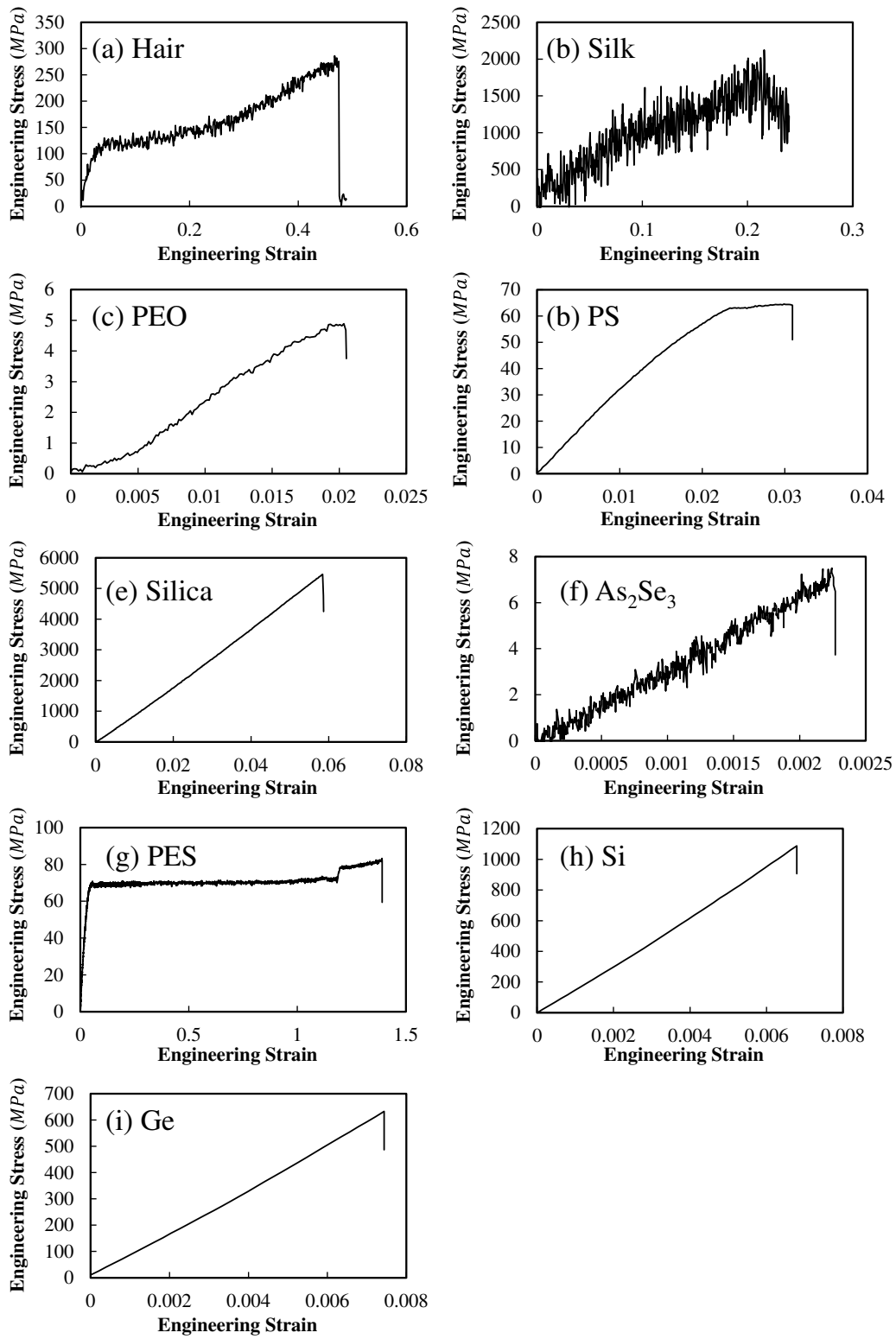
Figure 4: Engineering stress-Engineering strain curves of the tested core and cladding materials
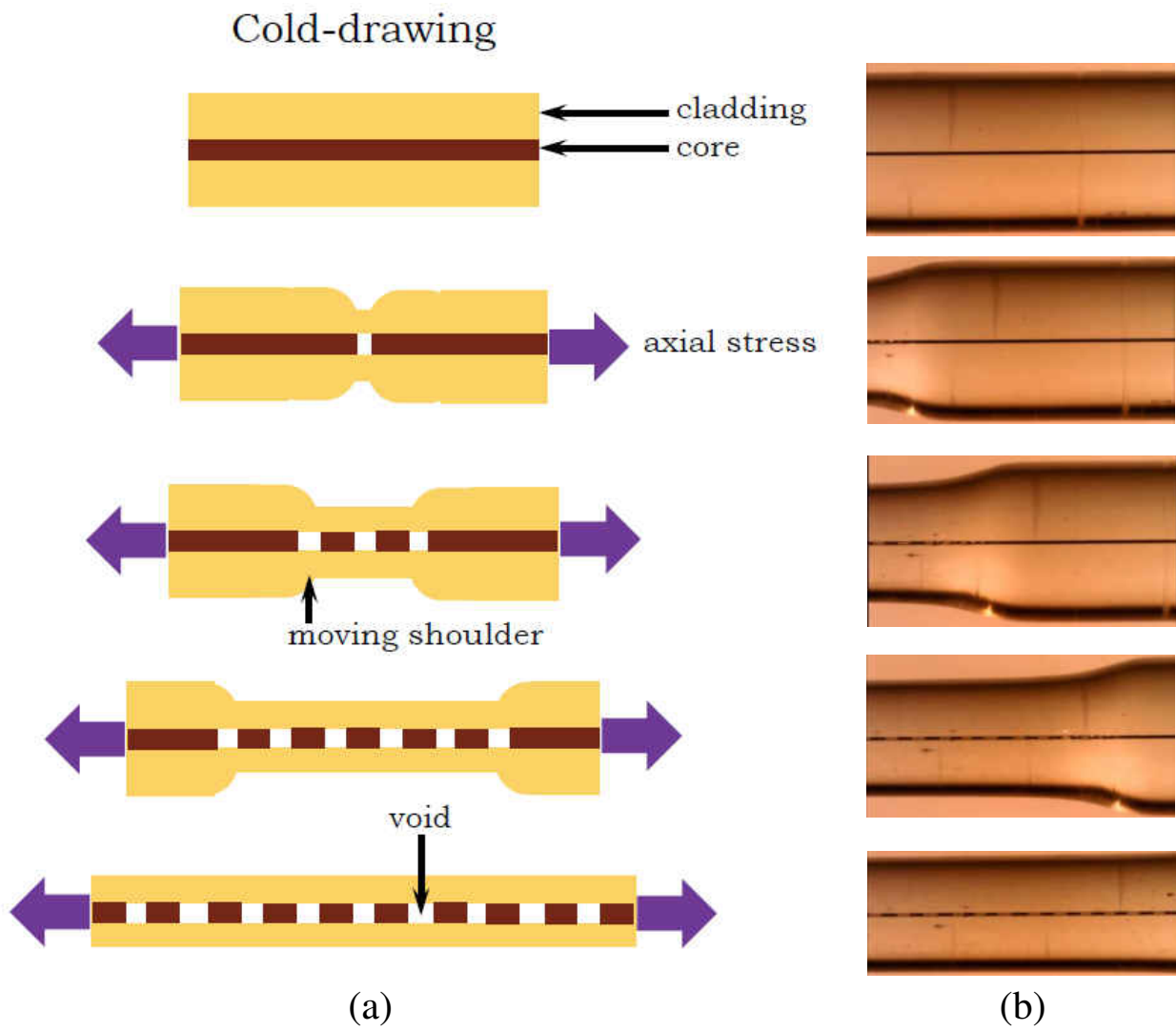
Figure 5: (a) Schematic of necking propagation and fragmentation of core material (b) Captured pictures of the experiments
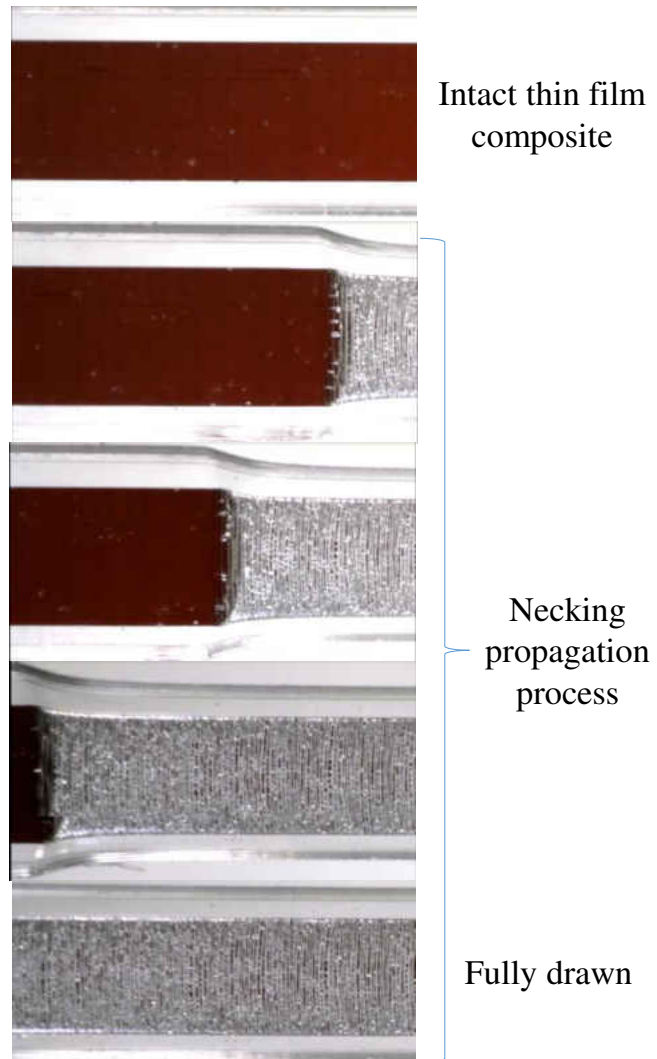
Figure 6: Captured pictures of the real necking propagation of TFC
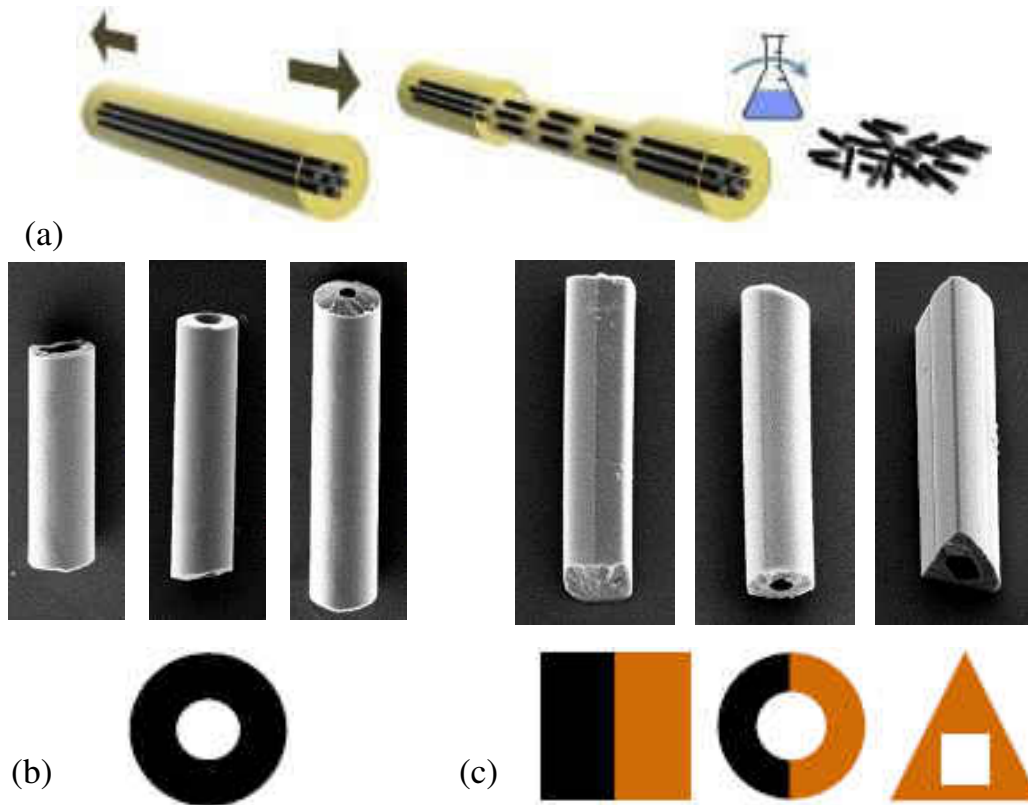
Figure 7: Complex cross section geometries utilized in cold-drawing process (a) multiple fibers (b) hollow cylinder core (c) complex particle structure

2.2 Unidirectional Carbon Fiber Polymer Matrix Composites

2.2.1 Experimental setup

Unidirectional carbon fiber composites are investigated in the study. The specimens are rectangular plates, which are 94.50 mm long, 20 mm wide and 4mm thick. A notch of radius 12 mm is introduced on each side and the minimum thickness of the plate is 1.5 mm in the center. See Figure 8. Specimens are made of unidirectional IM7 graphite fiber with 8552 epoxy. In order to reduce stress concentration and investigate the failure of the notched part, four aluminum tabs were attached to both sides of the specimens where clamps will be on. The fiber direction is along the axial direction. See Figure 9(a).

24
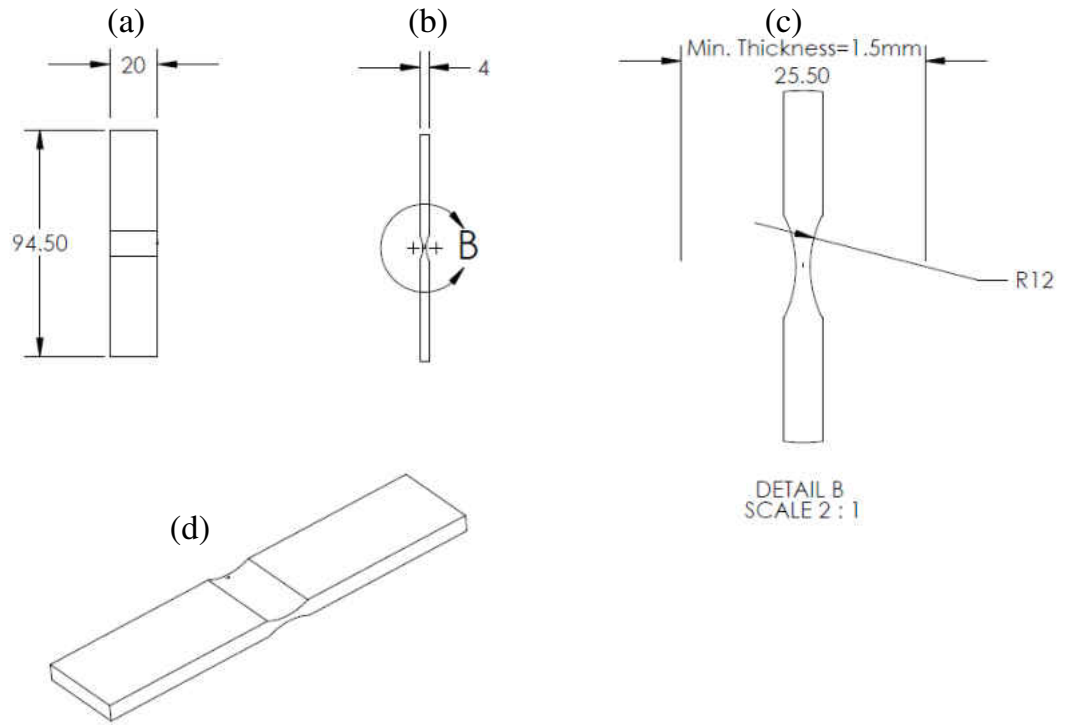
Figure 8: Dimension of carbon fiber composite. (a) front view (b) left view (c) detailed view of notch part (d) overall view of specimen

The tests were conducted at the Impact and Crashworthiness Laboratory in the Department of Mechanical Engineering at Massachusetts Institute of Technology, with an Instron load frame with both vertical and horizontal actuators for biaxial testing. See Figure 10. Combined loadings of tension/compression and shear are applied to the specimens. Along the fiber direction, tensile or compressive loadings is applied. Meanwhile, shear loading is applied on the transvers direction. Combination of the two axis loadings generated a series of loading conditions and a schematic plot is provided to illustrate the loading path in Figure 9(b). β represents the angle between the resultant total force F and the horizontal force F_H. It can be calculated through $\beta = \frac{180°}{\pi} \text{atan}(F_V/F_H)$. Totally, seven loading conditions were designed to test this material as listed in Table 1.

Table 1: Summary of loading conditions

Loading conditions	β	Repeat tests
Uniaxial compression	$-90°$	3
Compression + Shear	$-70°$	3
Compression + Shear	$-45°$	3
Shear	$0°$	3
Tension + Shear	$70°$	2
Tension + Shear	$80°$	3
Uniaxial tension	$90°$	3
	Total:	20
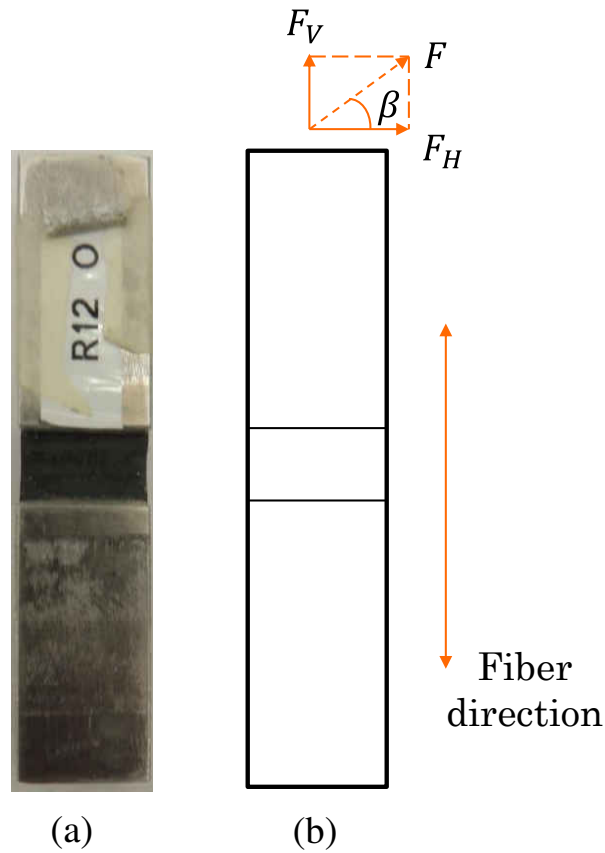
Figure 9: (a) A picture of a real specimen (b) Illustration of loading condition angle β

Since angle β needs to be maintained during a process, force control testing are applied to the specimen. In order to capture the deformation and failure modes, an optical measurement system recording images during tests was used to accurately measure displacement and strain fields. Images were captured by two cameras: one in the front view and the other one in the side view. Digital image correlation (DIC) technique was used to post-process the image data. Semi-gloss black and white paint were sprayed in small dots randomly on the specimen surfaces. Note that many specimen pictures in this paper show sprayed patterns.
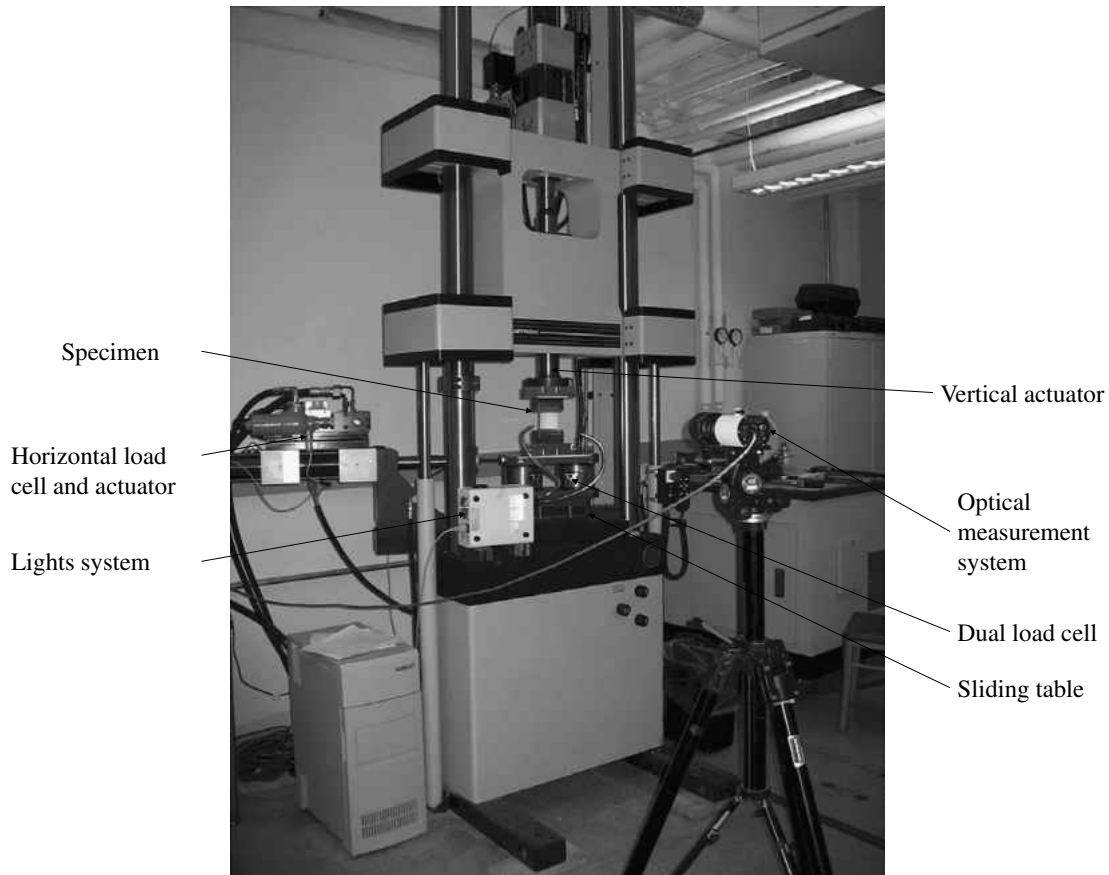
Figure 10: Instron dual-actuator loading frame (Bisagni & Walters, 2008)

2.2.2 Experimental results

2.2.2.1 Uniaxial compression

Three specimens were tested under uniaxial compression loading condition. Two of them were tested with displacement control and one was tested with force control. Tests curves show linear elasticity before failure with no obvious plasticity. The tests show good repeatability in regard to failure modes and material strength. All tests demonstrated brittle failure modes with local buckling during tests. The measured forces at total failure are in a range of 23.76 to 29.40 kN. The recorded force-displacement curve is shown in Figure 11.
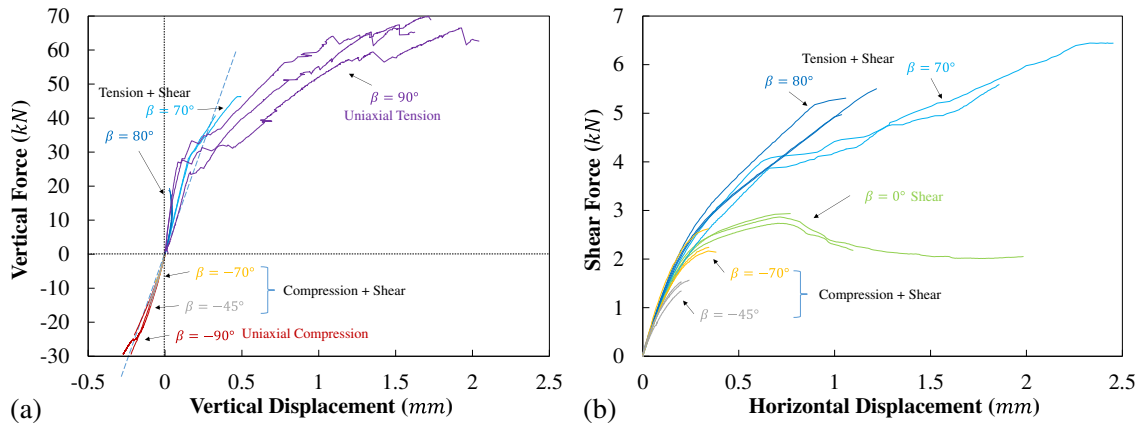
Figure 11: A collection of force-displacement curves of all seven loading conditions in (a) vertical and (b) horizontal directions

2.2.2.2 Compression + Shear with β = −70°

Three specimens were tested under combined compression and shear with $\beta = -70°$ loading condition. Experiments show good repeatability with force-displacement curves following similar trend and similar failure modes. In vertical direction, material presents linear elasticity of fibers and a small range of nonlinearity before failure. In horizontal direction, materials show a typical elastic-plastic behavior of polymer matrix. All tests show brittle failure modes during tests. The force-displacement curves of vertical and horizontal directions are also shown in Figure 11.

2.2.2.3 Compression + Shear with β = −45°

Three specimens were tested under combined compression and shear with $\beta = -45°$ loading condition. Similar behaviors as the ones with $\beta = -70°$ were observed. Experiments show good repeatability in terms of force-displacement curves and failure modes. In vertical direction, materials show linear elasticity till failure. In horizontal direction, materials show a typical

elastic-plastic behavior of polymer matrix. All tests show brittle failure modes during tests with a skew failure surface.

2.2.2.4 Shear

Three specimens were tested under shear loading condition. Two of them were tested with displacement control and the third one was tested with force control. For the two displacement control tests, material presents typical elastic-plastic behavior (due to matrix deformation) before failure initiation. After failure initiation, a long range of material softening occurs. For the one test with force control, material behaves the same before failure initiation. After failure initiation, material cannot sustain more loads in the horizontal shear direction and therefore total failure was observed. This phenomenon revealed that the matrix gradually degraded under displacement control and catastrophically failed under force control. A comparison of specimens between displacement control and force control shear tests is shown in Figure 12.

Figure 12: Comparison of last test step in shear tests between displacement control (left) and force control (right) shear tests

2.2.2.5 Tension + Shear with $\beta = 70°$

Two specimens were tested under combined tension and shear with $\beta = 70°$ loading condition. For both vertical and horizontal directions, material shows an elastic-linear plastic behavior. One

thing to mention here is that these two tests didn't run until total failure, because they were stopped when some delaminations were observed from the side view. See Figure 13. Due to high fiber tensile strength, delamination is the main degradation. It should be noted that the material can still sustain more loads under the same loading path if tests continued.
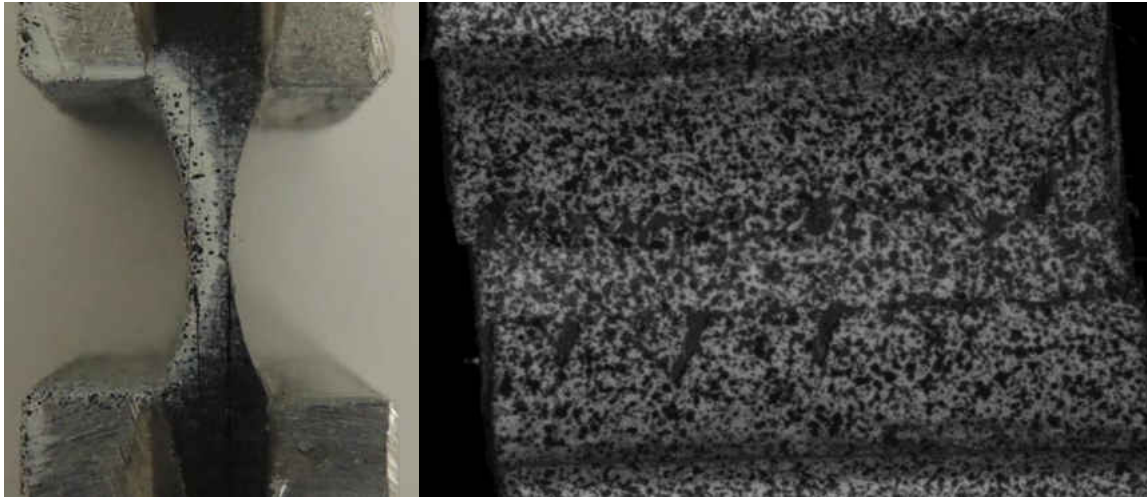
Figure 13: Delamination failure features observed under tests of combined tension and shear with β=70°. (left) Side view after tests (right) Front view during tests

2.2.2.6 Tension + Shear with $\beta = 80°$

Three specimens were tested under combined tension and shear with $\beta = 80°$ loading condition. Experiments showed good repeatability. For the vertical direction, the material presents a linear elastic range and then the displacement decreased with a load increasing. For the horizontal direction, the material showed an elastic-linear plastic behavior like the one under combined tension and shear with $\beta = 70°$ loading condition. It is interesting to find that the vertical displacement decreased as the load was increasing. This resulted from the strong anisotropy of the unidirectional PMCs material. As the material went through increasing tensile and shear loads, matrix degraded faster than fiber. The specimen had to be rotated more so that the force

decomposed from fiber tension force can contribute more to the horizontal direction. In this way, fibers got stretched with the increasing horizontal displacement and therefore the vertical force increased with a decreasing vertical displacement. For this loading conditions, material did not totally fail during the tests. Delamination is the main degradation. The specimen can still sustain more loads under the same loading path.

Three specimens were tested under uniaxial tension along fiber direction. Good repeatability was obtained. Material showed a small range of linear elasticity followed by large range of nonlinearity. The nonlinearity is brought in by delamination and sequential fiber pullout. These severe delamination failure features are shown in Figure 14, which is similar to "ductile failure" in some sense.
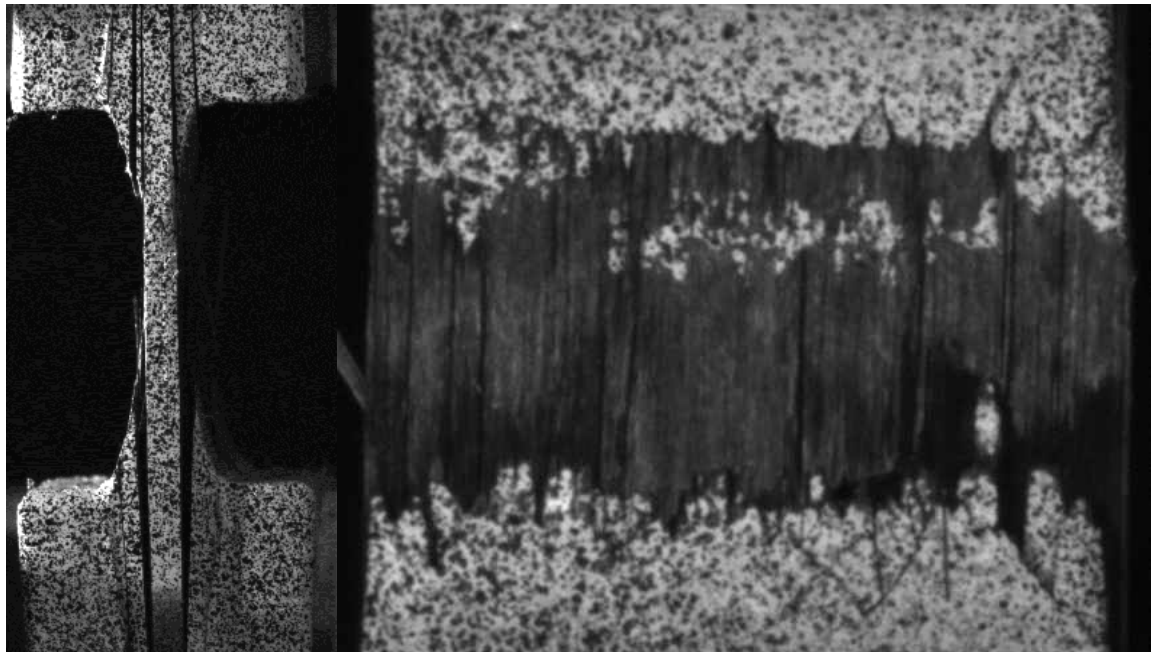
Figure 14: Severe delamination observed during uniaxial tension tests (left) side view (right) front view

2.2.3 Summary of experimental results

The PMCs materials exhibit strong asymmetric behaviors between tension and compression. Brittle failure features like local buckling were shown in compressive dominated loading conditions while "ductile failure" features like delamination and fiber pullout were observed in tensile and shearing dominated loading conditions. Material strengths in tension and compression showed notable difference. Specimens can sustain up to 70 kN in tension while only about 30 kN in compression. In addition, an interesting phenomenon in elastic moduli of tension and compression along fiber direction was exhibited. A collection of force-displacement curves of all conducted tests are shown in Figure 11. One can clearly see that composites are stiffer in elastic range under tension loading conditions than that of compression loading conditions.

Tests under shear loading conditions exhibit a unique material behavior, which include linear elastic, material strain hardening and post-failure softening behaviors. Matrix takes the main loads under this loading condition at the beginning and then fibers gradually takes the main loads when the matrix goes to failure and fibers rotate. Tests of loading conditions combined with shear show plasticity in both vertical and horizontal directions for most of the cases. The material nonlinearity mainly comes from the matrix and progressive delamination of composites.

2.3 Metallic Matrix Nano Composites

A series of nano-composite samples of magnesium/SiC were manufactured by using a ball milling process followed by subsolidus consolidation(Shen et al., 2013). The size of SiC particle was d=50nm. Two volume fractions (10% and 15%) of SiC particle were applied in the composites. All the experiments were conducted using an MTS universal testing machine. A quasi-static strain rate of about 10^{-3}/s was adopted for all tests reported. Optical measurements

with a digital image correlation (DIC) system were utilized to precisely measure strain fields. The system consists of a Tokina AT-X Pro macro 100mm-f/2.8-d lens with a resolution of 2448×2048 and the VIC-2D 2009 software by Correlated Solutions, Inc.. Since it is needed to get the local displacement between two selected gauge points, one DIC camera perpendicular to the specimen plane was used for all tests. The capture frequency was 1Hz. Semi-gloss black and white paint were sprayed in small dots randomly on the capturing surface of all specimens one day before testing, per to the requirement of DIC technique.

2.3.1 Uniaxial Tension

It is generally very hard to test MMNCs under tensile loading conditions due to their relatively brittle characteristic, which makes testing samples crack at the clamping boundary. One attempt was made for this part of work. A reduced-size dogbone specimen was applied for uniaxial tension tests due to the limitation of original sample size. A set of customized grips was designed for gripping and loading the specimens. The geometry of reduced-size dogbone specimen and the assembly is shown in Figure 15. The grips were connected to the loading frame by pins. The slant shoulder of the dogbone specimen could mitigate some stress concentration around the notch area. A pair of grooves, whose geometry matched the specimen shoulder, was cut from both of the grips to transfer the load to the specimen. The depth of each groove was equally $0.75mm$, which was half of the thickness of specimen (1.5mm). Two bolts were fastened for each grip to lock the entire specimen shoulder in the grooves. In this way the tensile load could be applied uniaxially to the specimen through the inner sides of the top shoulder. The gauge displacement was measured between two points at the top and bottom edges of the exposure part of the specimen by DIC.
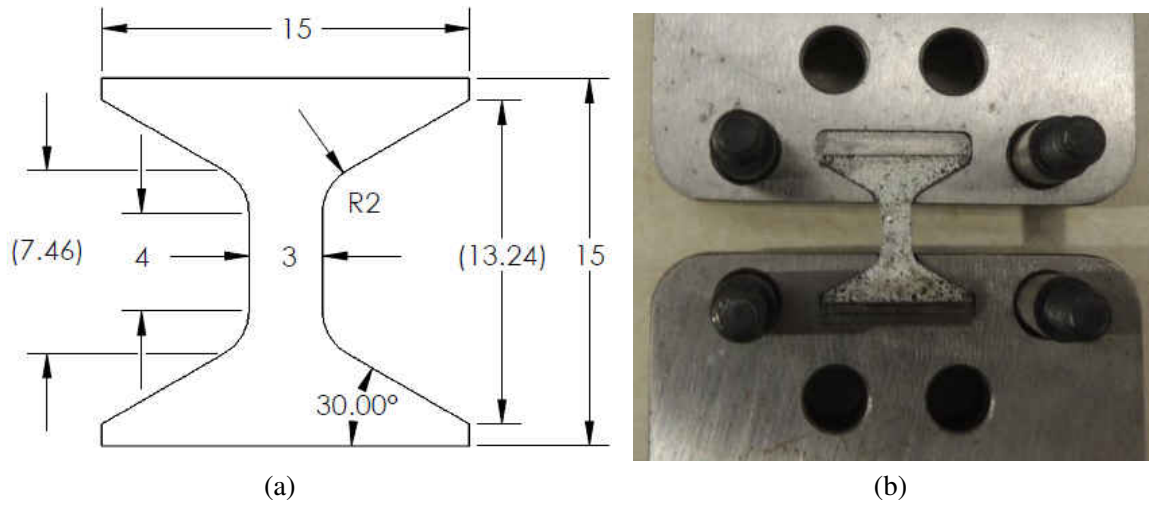
Figure 15: (a) Geometry of a reduced-size dogbone specimen (unit: mm) (b) half-assembled fixture showing grooves

The experimental results for uniaxial tension for these two Mg/SiC composites and the tested specimens are exhibited in Figure 16. One can see that a) the fracture behaviors for both material types were essentially brittle under tension, b) no clue for the plasticity was observed from tension tests. The fracture was initiated close to the notch area (due to stress concentration or surface imperfection), thus the fracture stress/strain for uniaxial tension was underestimated.
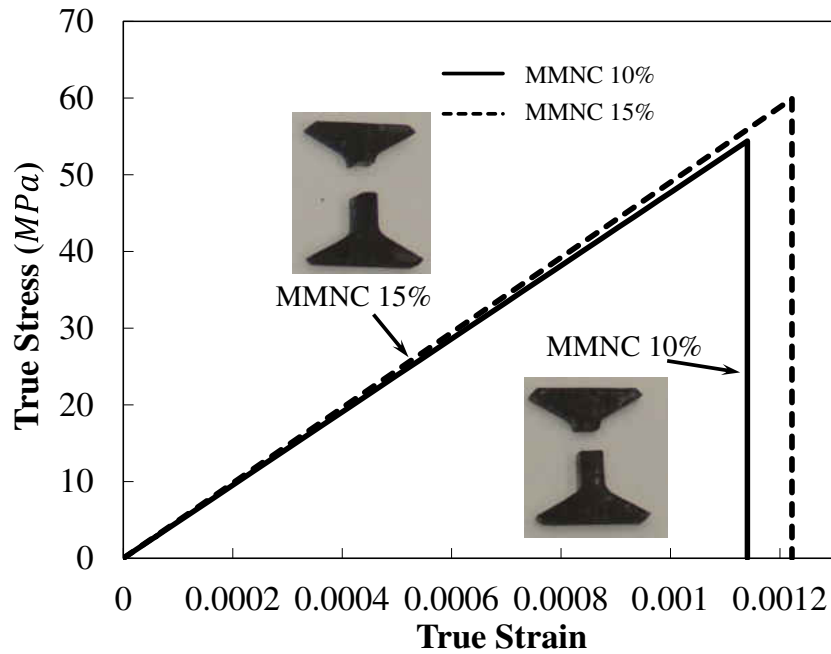
Figure 16: Stress-strain curves for MMNC 10% and MMNC 15% materials under uniaxial tension condition

2.3.2 Uniaxial Compression

A small cylinder specimen was designed for uniaxial compression tests. Both the length and the diameter were 5mm. The specimen was placed in the center on a round compression platen, which was fixed at the bottom of the load frame. The other piece of platen was driven by the load frame to apply a compression load downward. The surfaces between specimen and platens were lubricated by Vaseline before test to reduce the friction effect. One rectangular piece of white paper, with black dots sprayed, was adhered to the compression platens in order to obtain the compressive displacement using DIC. Three tests were conducted for each case.

The true stress-strain curves under uniaxial compression for these two Mg/SiC composites are illustrated in Figure 17. Different from uniaxial tension, the plasticity for all tested materials can be observed and the fracture strains were more than 10%. It can also be seen that a) a softening

behavior appeared right after going into the plastic region, and b) both materials show ductile fracture mode. The failed uniaxial compression specimens are also shown in Figure 17. One can see that the specimen of MMNC with 10% SiC particles has a slant fracture surface but with some small broken pieces, indicating shear dominated ductile fracture. The one of MMNC with 15% SiC particles, with failure strain up to around 15%, and it indicates ductile fracture, too. For composites, increasing of reinforcement particles usually results in higher strength but less ductility (Chawla, 2006; Milan & Bowen, 2004; Suresh, 2013). It is surprising to find that MMNC 15% had a higher compressive fracture strain than the one of MMNC 10%.
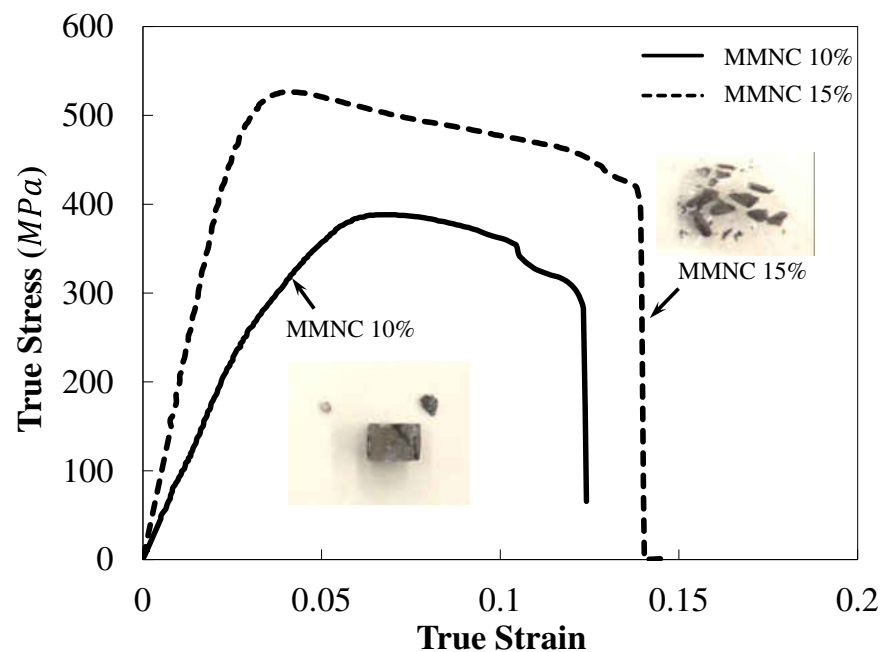
Figure 17: Stress-strain curves for MMNC 10% and MMNC 15% materials under uniaxial compression condition

2.3.3 Three-point Bending

A small rectangular plate was used for three-point bending tests. The length, width and thickness was 15mm, 6mm and 2mm, respectively. A customized three-point bending fixture was

manufactured for the specified dimension (shown in Figure 18). It was connected to the loading

frame by pins, and fastened by bearing nuts. Both the loading and supporting pins of three-point

bending had a geometry of half-cylinder, whose radii were 1.75mm. The distance between two

supporting pins in the bottom part was 10mm. Their side surfaces (onto the camera) were

sprayed by black and white dots as well to measure the vertical displacement between the tip of

loading and support pins by DIC. The plate was placed in the center of the bottom pins, along

both length and width directions. Three tests were done for each case.
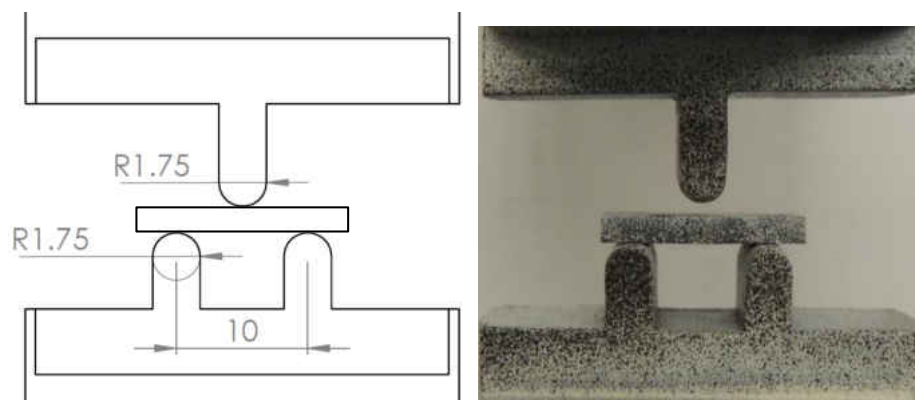
Figure 18: Three-point fixture assembly (unit: mm)

The representative force-displacement curves for both materials and tested specimens are given

in Figure 19. The fracture for all tests was initiated at the tensile side. This is because the fracture

stress under tension is much smaller than that of compression. With less stress concentration, the

fracture behavior obtained from three-point bending could be more reliable than that under

uniaxial tension.
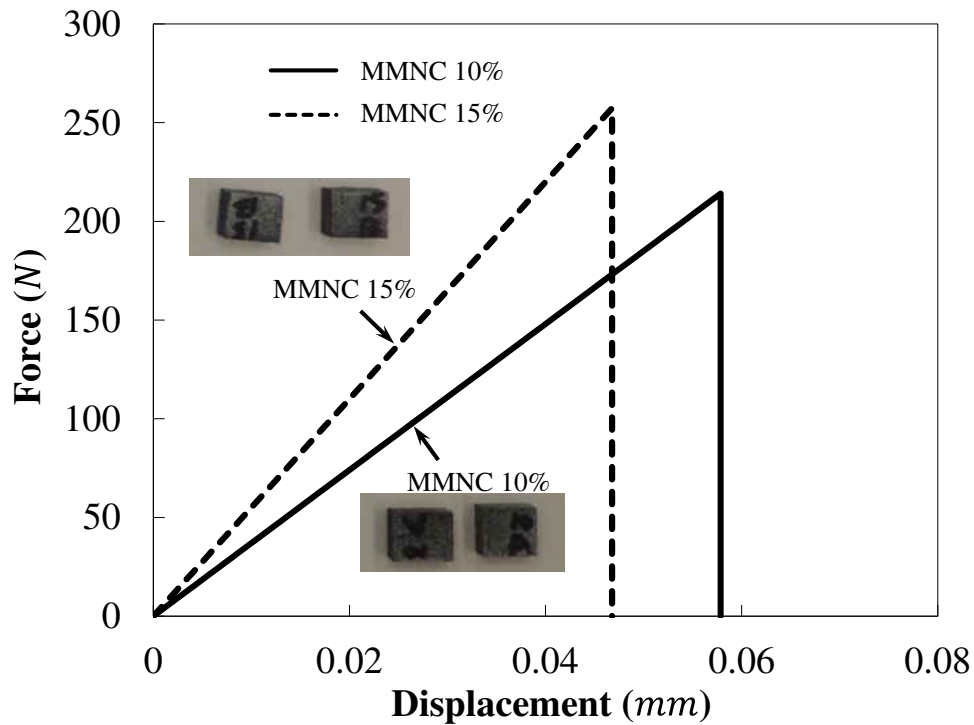
Figure 19: Force-displacement curves for MMNC 10% and MMNC 15% materials under three-point bending condition

2.3.4 Summary

All tested materials exhibit strong asymmetric behaviors between tension and compression. The key features are summarized as follows. (1) Both the fracture strain and stress were much higher under compression than tension. (2) Apparent plastic behavior was observed with softening (after crack initiation) under compression while no plasticity occurred under tension and three-point bending tests. (3) All tensile failures were brittle while compressive failures show a shear dominated ductile failure mode. For the MMNC materials, the SiC particle reinforcement was significant. The compressive strength of pure magnesium is about 240MPa(Habibi, Hamouda, & Gupta, 2012), but the MMNC 15% gives a yield strength over 500MPa.

CHAPTER 3 FRAMEWORK OF COMPOSITE MATERIAL MODELING

For single fiber composite and thin-film composite, details of the composition can be modelled. For the PMCs and MMCs which have plenty of reinforcements like fibers and particles, the details of the composition cannot be modelled due to the limitation of computing power. This framework of composite material modeling comprises elasticity, plasticity, failure initiation and post failure softening.

3.1 Elasticity

A composite material is a material made from two or more constituent materials with significantly different physical properties. The composition can have different elasticity. For example, the core material in the SFC is a linear elastic material while the polymer is a hyperelastic-plastic material. While it comes to the complex composite materials, the material usually behave linear elasticity like MMNCs and PMCs. For unidirectional carbon fiber composites, it shows orthotropic elasticity.

An interesting phenomenon has been found in MMNCs and PMCs from our experiments. The Young's moduli in tension and compression are different. Young's modulus has been reported to be dependent on stress state for materials like porous or clastic rocks, golden films and soils (Brown, Bray, & Santarelli, 1989; Cazacu, 1999; Jarausch, Kiely, Houston, & Russell, 2000; Pozdnyakova, Bruno, Efremov, Clausen, & Hughes, 2009; Yu & Dakoulas, 1993). Jones (1977) and Hamilton, Efstathiou, Sehitoglu, and Chumlyakov (2006) reported different Young's modulus in compression and tension direction for materials like fiber-reinforced, granular composite and single crystals NiFeGa. This phenomenon on PMCs was also noticed and studied

by W. van Dreumel (1982), W. H. Van Dreumel and Kamp (1977), Furuyama et al. (1993), Melanitis, Tetlow, Galiotis, and Smith (1994), Đorđević, Sekulić, and Stevanović (2007) and Djordjević, Sekulić, Mitrić, and Stevanović (2010). This phenomenon can be described as an S shape curve which distinguishes tensile and compressive loadings. In order to avoid numerical issues, transition loadings will be applied to the curve (Figure 20).
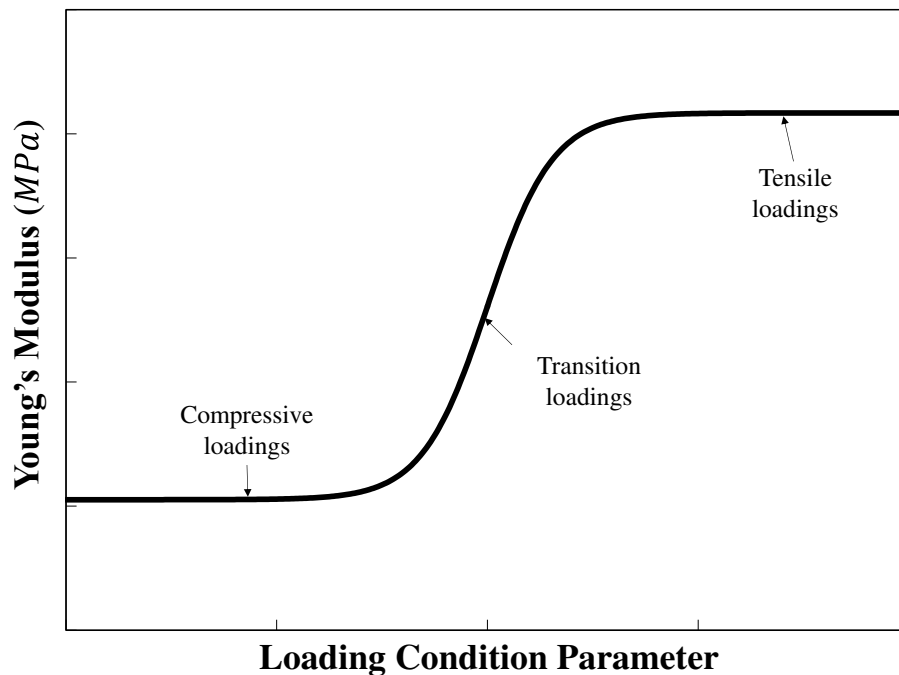
Figure 20: An illustration of the Young's modulus dependence on loading condition parameter

<u>3.2</u> Plasticity

Yield surface and plastic flow are complicated for the composites materials since plasticity is not shown on all the composites composition. For brittle materials like the core material As_2Se_3 in SFC and the carbon fibers in PMCs, materials show linear elasticity and brittle failure following. However, the matrix materials usually possess plasticity like the PES matrix in SFC, metal matrix in MMNCs and polymer matrix in PMCs. Then the composites plasticity is a complex

combination of the linear elasticity of the brittle material and the plasticity of the ductile material. Both isotropic and anisotropic yield criterion could be use on the composite materials since the material can have symmetric or asymmetric yield strength in tension and compression.

3.3 Damage initiation

Damage initiation defines the point of the initiation of degradation of stiffness. Usually composites have highly unsymmetrical damage initiation between different loading conditions. Various damage initiation criteria have been used in composites modeling as explained in the introduction section. Here for the MMNCs, a stress-based modified Mohr-Coulomb criterion (sMMC) will be used. MMNCs are metal matrix composites and the sMMC criterion has been proven to be effective in modeling metals and alloys. For the PMCs, Tsai-Wu failure criterion is used as the failure initiation since this model has shown effectiveness in the WWFE (M. Hinton, Kaddour, & Soden, 2002). Damage indicator is defined as the following.

$$D = \frac{\bar{\sigma}}{\hat{\sigma}_f(\psi)}, \qquad if\ D \leq 1. \tag{5}$$

Here $\bar{\sigma}$ is the equivalent stress and $\hat{\sigma}_f(\psi)$ is damage initiation limit of the current loading condition ψ. The following is a table of the stress-based damage initiation criteria.

Table 2: A summary of stress-based failure criteria

Tsai-Wu	$\hat{\sigma}_f = F_1\sigma_1 + F_2\sigma_2 + F_3\sigma_3 + F_4\sigma_4 + F_5\sigma_5 + F_6\sigma_6 + F_{11}\sigma_1^2 + F_{22}\sigma_2^2$ $+ F_{33}\sigma_3^2 + F_{44}\sigma_4^2 + F_{55}\sigma_5^2 + F_{66}\sigma_5^2 + 2F_{12}\sigma_1\sigma_2 + 2F_{13}\sigma_1\sigma_3$ $+ 2F_{23}\sigma_2\sigma_3$
sMMC	$\hat{\sigma}_f(\eta,\bar{\theta}) = C_2 \left\{ \left[\tilde{C}_\theta^s + \dfrac{\sqrt{3}}{2-\sqrt{3}}(\tilde{C}_\theta^{ax} - \tilde{C}_\theta^s)\left(\sec\left(\dfrac{\bar{\theta}\pi}{6}\right)-1\right) \right] \left[\sqrt{\dfrac{1+C_1^2}{3}}\cos\left(\dfrac{\bar{\theta}\pi}{6}\right) \right. \right.$ $\left. \left. + C_1\left(\eta + \dfrac{1}{3}\sin\left(\dfrac{\bar{\theta}\pi}{6}\right)\right) \right] \right\}^{-1}$
Tresca	$\hat{\sigma}_f = \max(\lvert\sigma_1 - \sigma_2\rvert \quad \lvert\sigma_2 - \sigma_3\rvert \quad \lvert\sigma_3 - \sigma_1\rvert)$
Von-Mises	$\hat{\sigma}_f = \sqrt{\dfrac{1}{2}[(\sigma_{11}-\sigma_{22})^2 + (\sigma_{22}-\sigma_{33})^2 + (\sigma_{33}-\sigma_{11})^2 + 6(\sigma_{12}^2 + \sigma_{23}^2 + \sigma_{31}^2)]}$
Hill	$\hat{\sigma}_f$ $= \sqrt{F(\sigma_{11}-\sigma_{22})^2 + G(\sigma_{22}-\sigma_{33})^2 + H(\sigma_{33}-\sigma_{11})^2 + 2L\sigma_{12}^2 + 2M\sigma_{23}^2 + 2N\sigma_{31}^2}$

3.4 Post Failure Softening

It is assumed that material softening starts after failure initiation. This is an important aspect which affects the prediction for failure stress, failure strain and failure modes (Donadon et al., 2009; Matzenmiller et al., 1995). Fracture toughness and softening rate can affect the post failure softening.

After failure initiation, the damage accumulation is defined by an incremental form:

$$dD = \frac{Ld\tilde{\sigma}\bar{\varepsilon}^p}{G_c(\psi)}. \tag{6}$$

Here L is the characteristic length of a finite element in the simulation. $\tilde{\sigma}$ is equivalent stress that incorporates the effect of material post-failure softening. $d\bar{\varepsilon}^p$ is the incremental work conjugate plastic strain. $G_c(\psi)$ is the toughness or critical strain energy release rate at fracture which is also

a function of loading condition ψ. $d\tilde{\sigma}\bar{\varepsilon}^p$ is the plastic strain energy incremental per unit volume, and $L d\tilde{\sigma}\bar{\varepsilon}^p$ represents strain energy incremental per unit surface. While damage indicator reaches two, it indicates that the accumulated strain energy reaches critical value and the material is defined as total failure.

The loading conditions can also influence the process of the post failure softening. Here a post failure softening coefficient is proposed.

$$\tilde{\sigma} = \bar{\sigma}[1 - Se(\psi)(D-1)^{S_m}], \qquad (if\ 1 < D \le 2) \qquad (7)$$

where $\bar{\sigma}$ is the equivalent stress including strain hardening. $Se(\psi)$ is a parameter to control the ultimate failure stress which also depends on loading condition ψ, and S_m is a parameter to determine stress softening rate with respect to damage accumulation indicator D. The material post-failure softening coefficient $[1 - Se(\psi)(D-1)^{S_m}]$ is demonstrated in Figure 32.
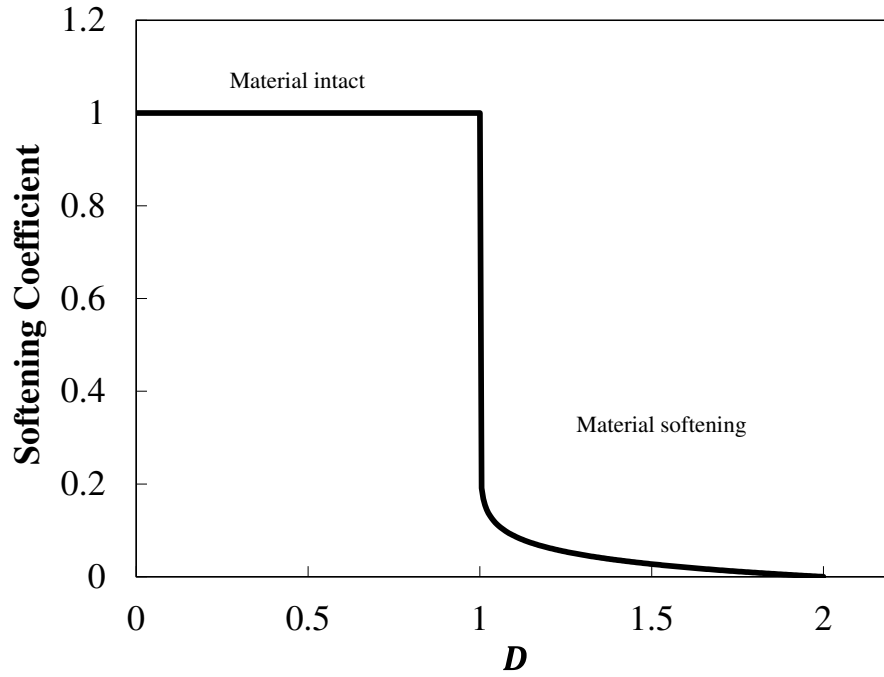
Figure 21: Material post-failure softening evolution curve (set $Se(\psi) = 1, S_m = 0.08$)

A composite usually have different failure modes under different loading conditions. The toughness need to represent this asymmetric feature. A loading condition dependent fracture toughness $G_c(\psi)$ is defined as follows.

$$G_c(\psi) = G_{Fc0} + \frac{G_{Fc1}}{1 + e^{G_{Fc2}(\psi + \psi_{G0})}} \tag{8}$$

Here G_{Fc0}, G_{Fc1}, G_{Fc2} and ψ_{G0} are model parameters for describing the brittle-ductile fracture transition. A typical toughness relationship with loading condition is shown in Figure 22.
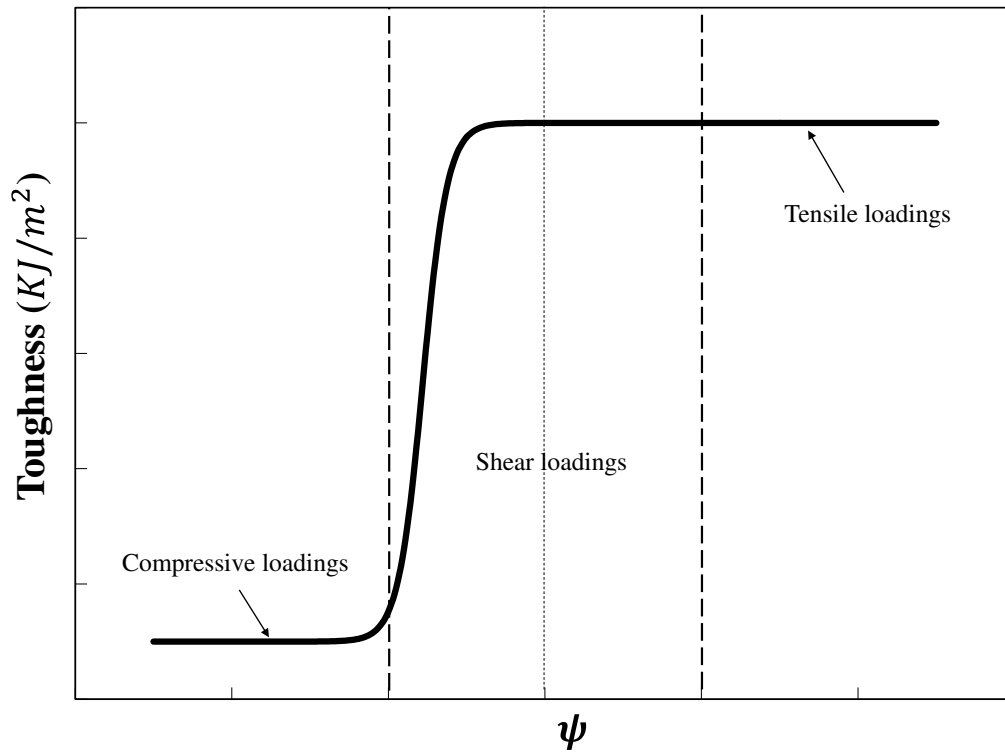
Figure 22: Material fracture toughness versus loading condition parameter ψ

CHAPTER 4 SINGLE FIBER COMPOSITE AND THIN-FILM COMPOSITE

4.1 Theoretical Modeling

4.1.1 Necking Propagation Model

The single fiber composite is one simple composite which contains a single fiber embedded in the polymer matrix. The stress-strain curves shown in Figure 4 does not indicate the real material property. For the PES material, when the stress goes into the stage of plateau, the material is undergoing necking propagation process. In this process the true stress shown in the Figure 4 is invalid. An elastic-viscoplastic continuum model proposed by Anand and Gurtin (2003) is used in simulating necking propagation process. This model introduces an internal-state variable that represents the local free-volume associated with certain metastable states and is able to capture the highly non-linear stress-strain behavior that precedes the yield-peak and gives rise to post-yield strain softening. This model explicitly accounts for the dependence of the Helmholtz free energy on the plastic deformation in a thermodynamically consistent manner. This dependence leads directly to a backstress in the underlying flow rule, and allows us to model the rapid strain-hardening response after the initial yield-drop in monotonic deformations.

Parameters of the model have been calibrated to test data in the finite-element computer program ABAQUS/Explicit with a user material subroutine. The stress-strain curve is obtained from a monotonic simple tension experiment of PES material. Nominal stress-strain curve has been plotted in Figure 23. For the test data, the curve shows an initial approximately linear region. Then it becomes a plateau with small increase along strain enlarging till failure. For the simulation, the curve also shows a linear region to a peak stress and then strain-softens to a

plateau. In the simulation, the linear part correspond to the initial elastic stretch and the peak is due to the local strain hardening and then the necking occurs and propagates which decreases the dimension of cross section. Total force decreases due to the decrease of cross section and reflects on nominal stress.
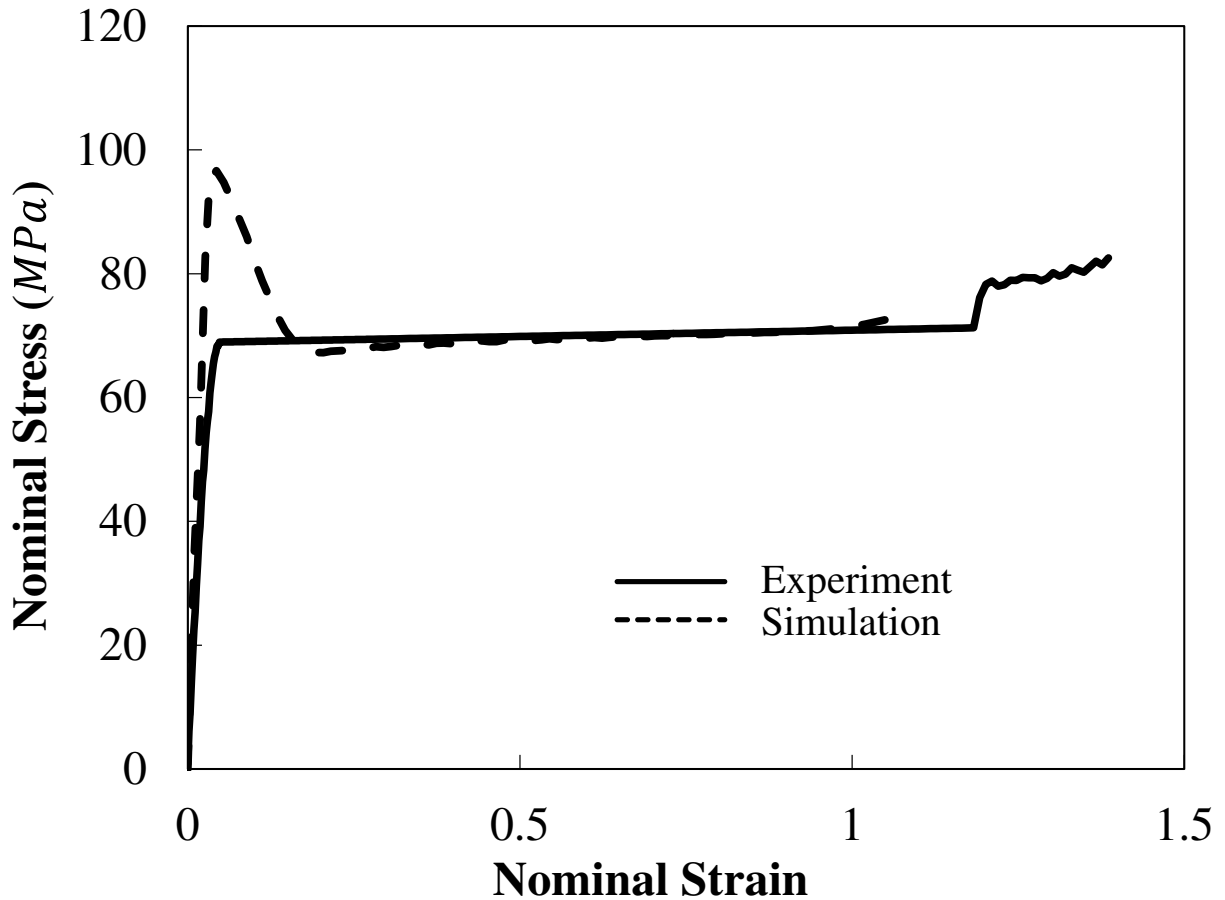
Figure 23: Nominal stress-strain response of PES in simple tension, together with simulation result of the same process

The list of parameters for calibration of the elastic-viscoplastic model are in

Table 3.

Table 3: Parameters used for calibration elastic-viscoplastic model

$E(MPa)$	μ	$\mu_R(MPa)$	λ_L	$\dot{\gamma}_0(1/s)$
2280	0.33	4.0	1.45	$2e15$
δ_F	$S_0(MPa)$	$S_{SS}(MPa)$	$H_0(MPa)$	α
$3.23e-19$	120.0	100.0	300.0	0.08

With the parameters above, a true stress-strain curve is shown in Figure 24.
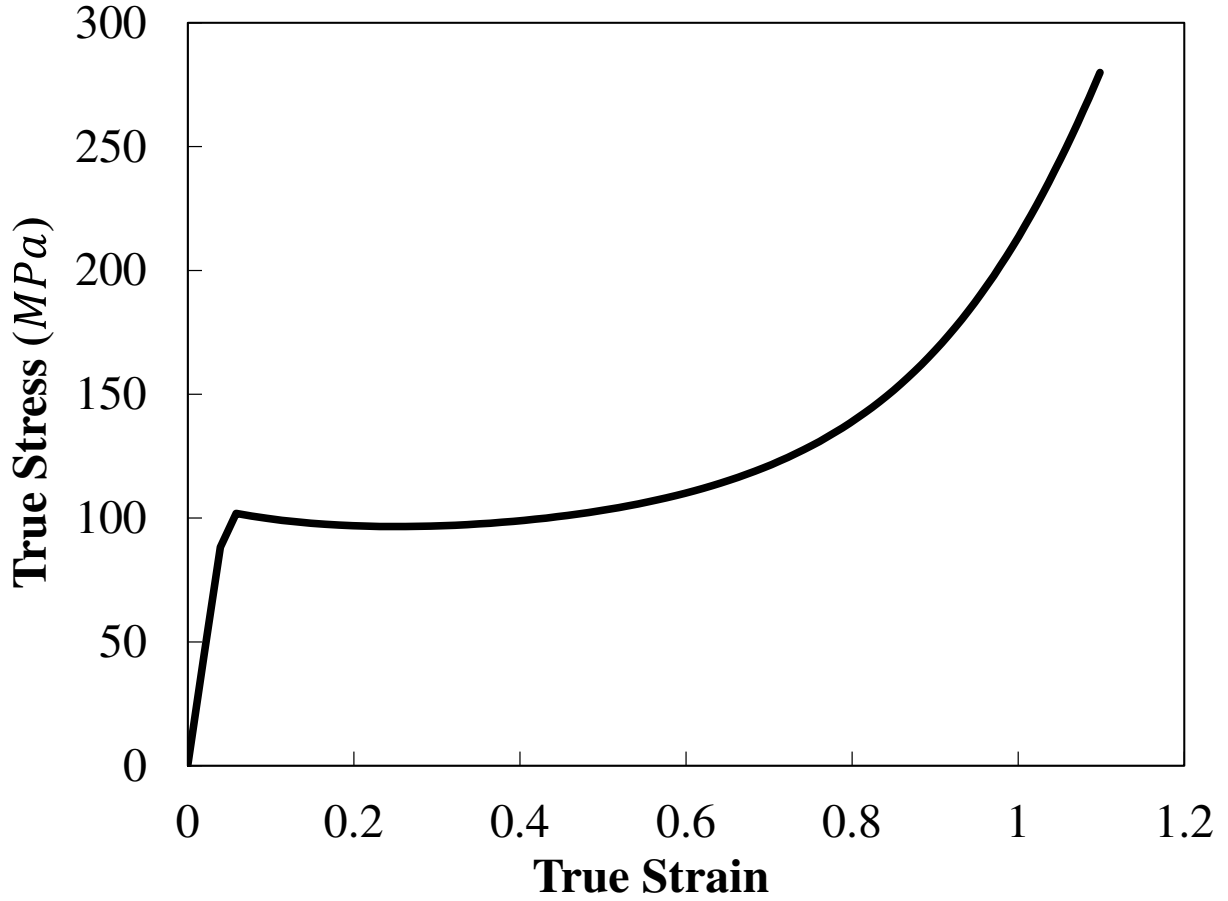
Figure 24: True stress-true strain curve of PES obtained using FE simulation

After an initial approxiamtely linear region, the stress-strain curve shows some non-linear prior to reaching a peak in the stress; the material then strain-softens to a quasi-plateau before beginning a broad region of rapid strain hardening. The necking happens when the material reaches the peak and begin to deform with large strain. Then the material strain-hardens to a much higher stress level and begins stretching adjacent material forming the necking propagation. A comparison of the diameter change between test and simulation has been made. For test, the range of the diameter decreases are 10% to 30%. The simulation shows a diameter decrease of 26.9% which fits well with the test data.

4.1.2 Cracking Model

For the As_2Se_3 material, the stress-strain curves form Figure 4 cannot reveal the real behavior either. A material post-failure softening has to be brought in to fully describe the behavior. The brittle cracking failure model used for core section is a built-in model in ABAQUS. The main ingredients of the model are a strain rate decomposition into elastic and cracking strain rates, elasticity, a set of cracking conditions, and a cracking relation (the evolution law for the cracking behavior).

The strain rate decomposition is as follows:

$$d\varepsilon = d\varepsilon^{el} + d\varepsilon^{ck}, \tag{9}$$

where $d\varepsilon$ is the total mechanical strain rate, $d\varepsilon^{el}$ is the elastic strain rate representing the uncracked concrete (the continuum between the cracks), and $d\varepsilon^{ck}$ is the cracking strain rate associated with any existing cracks.

The intact continuum between the cracks is modeled with isotropic, linear elasticity. And a simple maximum normal stress criterion is used to detect crack initiation. This states that a crack forms when the maximum principal tensile stress exceeds the tensile strength of the brittle material. After a crack initiates, a consistency condition for cracking is introduced which includes a tension softening model (mode I fracture) in the case of the direct components of stress and a shear softening/retention model (mode II fracture) in the case of the shear components of stress.

$$\boldsymbol{C} = \boldsymbol{C}(\boldsymbol{t}, \boldsymbol{\sigma}^{I,II}) = \boldsymbol{0} \tag{10}$$

where

$$\boldsymbol{C} = [C_{nn} \quad C_{tt} \quad C_{ss} \quad C_{nt} \quad C_{ns} \quad C_{ts}]^T$$

The cracking condition for a particular crack normal direction n is:

$$C_{nn} = C_{nn}(t_{nn}, \sigma_t^I) = t_{nn} - \sigma_t^I(e_{nn}^{ck}) = 0, \tag{11}$$

for an actively opening crack, where $\sigma_t^I(e_{nn}^{ck})$ is the tension softening evolution.

The crack opening dependent shear model (shear retention model) is written as

$$C_{nt} = C_{nt}(t_{nt}, \sigma_s^{II}) = t_{nt} - \sigma_s^{II}(g_{nt}^{ck}, e_{nn}^{ck}, e_{tt}^{ck}) = 0 \tag{12}$$

for shear loading or unloading of the crack, where $\sigma_s^{II}(g_{nt}^{ck}, e_{nn}^{ck}, e_{tt}^{ck})$ is the shear evolution that depends linearly on the shear strain and also depends on the crack opening strain.

For the normal and shear cracking conditions, $\sigma_t^I(e_{nn}^{ck})$ and $\sigma_s^{II}(g_{nt}^{ck}, e_{nn}^{ck}, e_{tt}^{ck})$ can be defined to fit the observed phenomenon.

Totally 8 core materials are tested and we have calibrated 2 representative ones of them: Si and As$_2$Se$_3$. Si has relatively large Young's modulus and As$_2$Se$_3$ has small Young's modulus. Figure 25(a) is the curve for tension softening evolution of the material As$_2$Se$_3$. The curve shows a linear region which corresponds to the intact elastic part. Then the crack initiates after peak stress and stress decreases along increasing cracking strain till failure. The fracture strength is the same as the test data and the fracture strain has been modified to fit the fracture mode since experiment can only capture the whole strain of sample but local strain (Hillerborg, Modéer, & Petersson, 1976). Figure 25(b) is the curve for shear retention factor dependence on crack opening. The shear retention factor decreases from 1 with no cracking strain to 0 when total failure. A similar material post-failure feature is applied to the material Si.

(a)   (b)
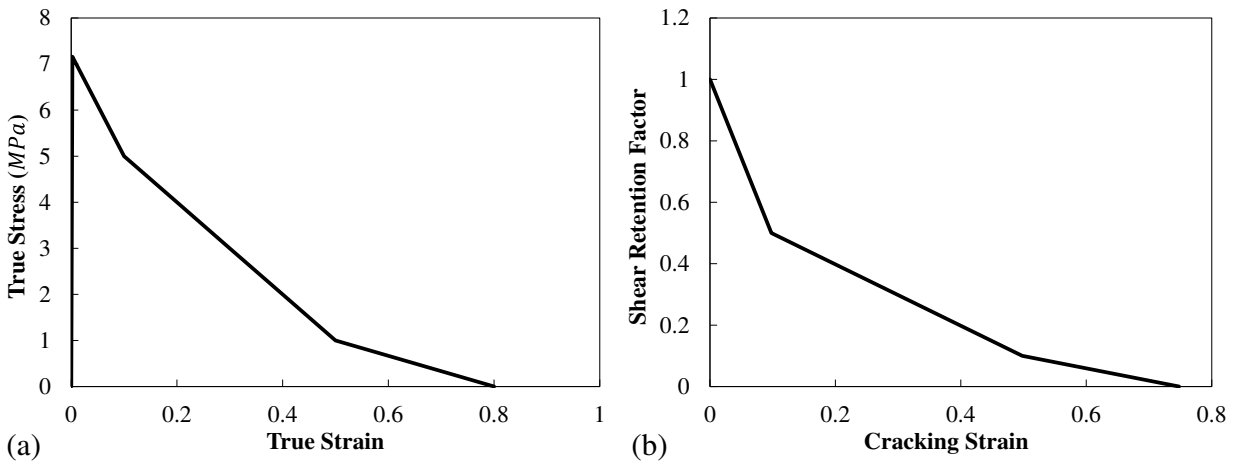
Figure 25: (a) Tension softening evolution of As$_2$Se$_3$ and (b) shear retention factor dependence on cracking strain

Since the failure strain are relatively larger than the test data, a simulation has been conducted to examine the cracking model. A dogbone model has been set up with material As$_2$Se$_3$ whose length is 42mm. A displacement of 0.12mm is applied to the top of the dogbone model. The

resultant failure strain is close to the test data. The comparison of test and simulation is in Figure 26. The comparison between experiment and simulation validated the cracking model.
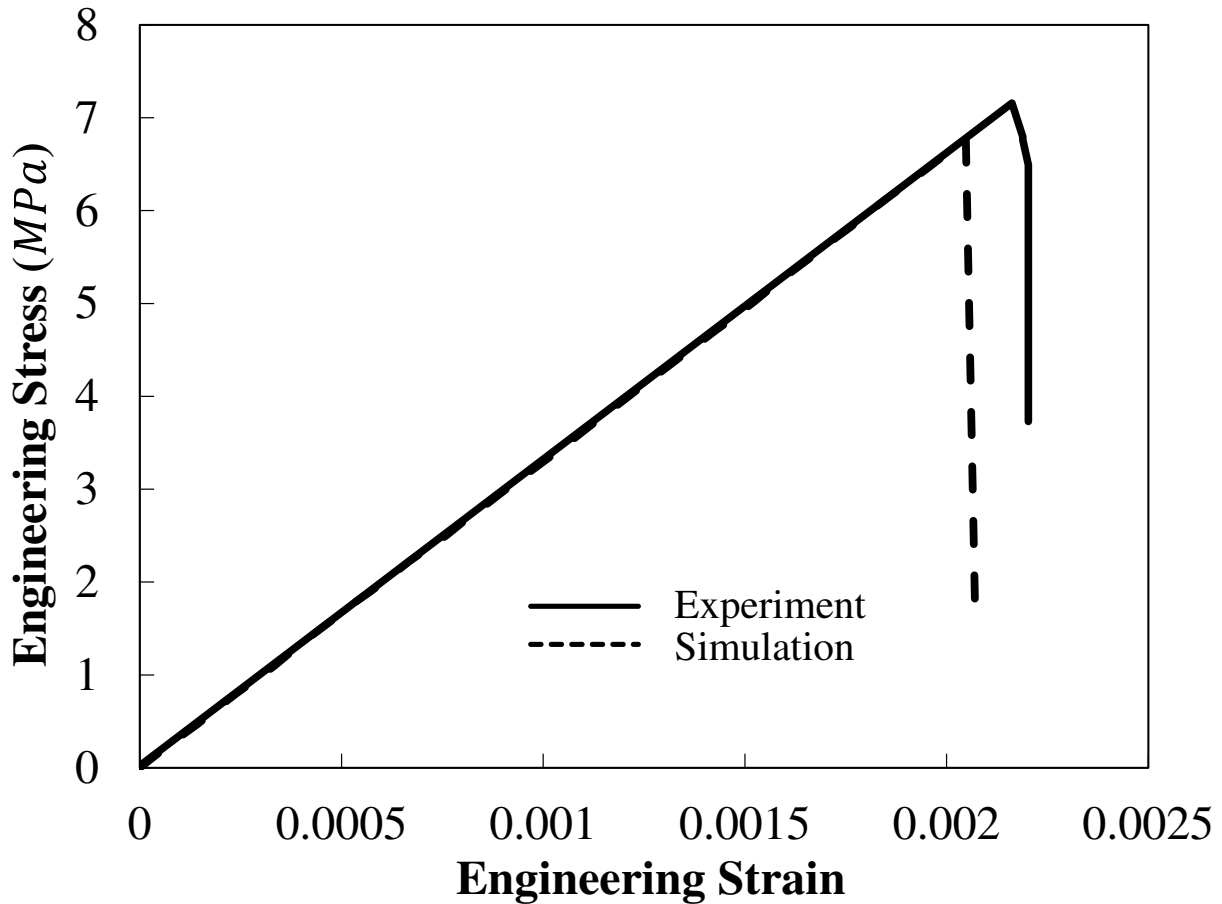
Figure 26: Comparison between experimental and simulation stress-strain curves of uniaxial tension of As_2Se_3

4.1.3 Interfacial Model

An interfacial model is brought into the modelling of the SFC and TFC. The feature of interface has been brought into simulation by the representative volume element (RVE) method and can provide good fits to the experiments (X. Chen & Liu, 2001; Y. Liu, Xu, & Luo, 2000). The interphase is between the core material and the cladding. It possesses similar properties to PES

but with much weaker strength; thus the stress-strain curve for this interfacial layer is taken to be the same as the PES, but multiplied by a scalar factor that depends on the core material. The interphase materials could be determined from the FE simulations to fit the failure features. The interphase material properties depending on the core materials are shown in Figure 27.

(a)

(b)
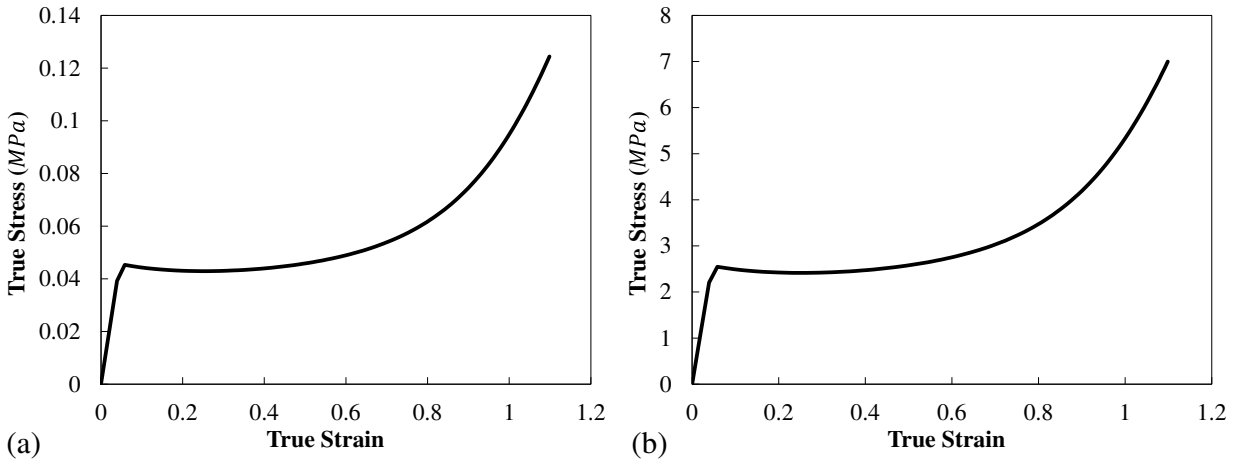
Figure 27: Interphase material (matrix side) properties for core materials (a) As$_2$Se$_3$ (b) Si

4.2 Model Setup

The explicit solver of the non-linear finite element code (ABAQUS, 2011) was used for the computational analyses of the cold-drawing process. Axisymmetric model is built and totally 3 sections are used for the simulation. See Figure 28. The inner section corresponds to the core material and the cladding section corresponds to the PES matrix. There is an interface section between the core and cladding section which possesses PES material property but much weaker than the cladding PES material. Two material models are used in the simulation: For core section, a brittle cracking failure model is used which includes linear elastic range and some softening behavior at crack propagation, of which linear elastic range and the fracture limit are input as material data from tests. For the cladding PES material, an elastic-viscoplastic continuum model

54

proposed by Anand and Gurtin (2003) is calibrated according to the test data and used in simulations.
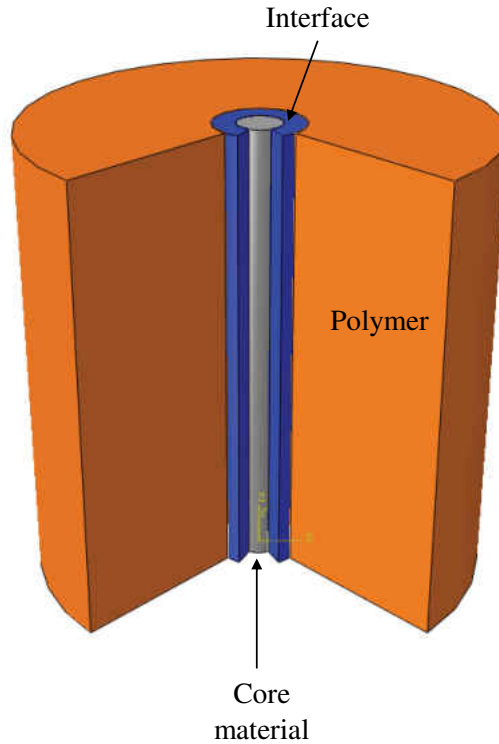
Figure 28: Schematic plot of the single fiber cold-drawing

The flat-fiber cold-drawing simulations are carried out using a similar procedure to that of the cylindrical-fiber simulations. A plane-strain model is built in the plane spanned by the fiber longitudinal axis and the fiber thickness (Figure 29). This is a good approximation for the thin film since the strain in transverse direction is much smaller compared to those of the other two directions during cold-drawing. A quarter of the cross-section is modeled with symmetric boundary conditions using CPE4R elements (75×1000 nm^2). There are three sections defined in the simulation: the film, an interfacial layer, and the outer PES cladding. The dimensions used in the simulation are the same as those in the experiment: the film and fiber thicknesses are 300 nm

and 350 μm, respectively, and initial fiber length is 1.44 mm. The material models used are the same as those used in the cylindrical cold-drawing simulations above. The moving grip applies a constant tensile velocity of 2 mm/s.
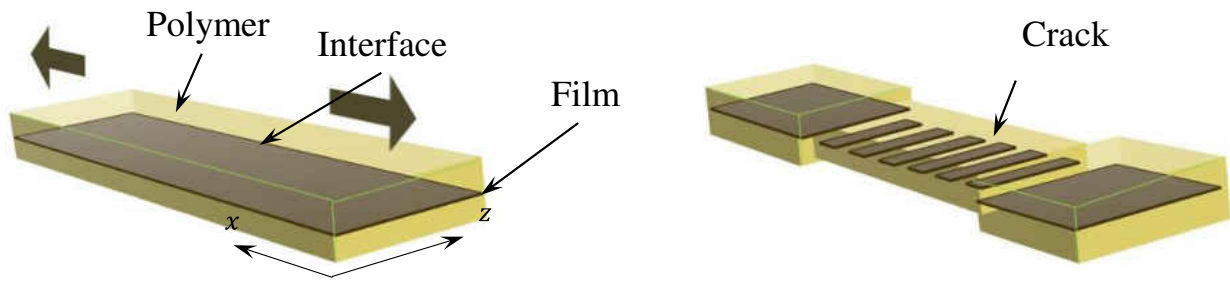
Figure 29: Schematic plot of the flat-fiber cold-drawing

4.3 Simulation Results

4.3.1 Single Fiber Composite

In the finite element simulations, the lower grip is fixed in the vertical direction and the upper grip is applied with a constant velocity $5mm/s$ upwards. At first, no displacement has been applied in step i. In step ii, a minor displacement is applied and therefore some random crack could be found in the core. As the upper grip goes further, necking is found in step iii and the core in the center breaks into segments uniformly. Necking continues in step iv and the distance between segments enlarges due to the stretch from the cladding. Necking propagates due to the low strain hardening of the cladding material and the fiber continues to break into segments as the necking propagates. The step v shows that necking fully propagates and the whole fiber uniformly breaks into segments. The process shown in the Figure 30 is the cold-drawing of As$_2$Se$_3$ with an initial diameter of 10 um. And another core material Si is also simulated and a summary of these two materials is listed in Table 4. It is found that the ratios of piece length

versus core diameter (L/D ratio) fit well with the test data. The standard deviation of the L/D ratio is also provided in the table for reference.
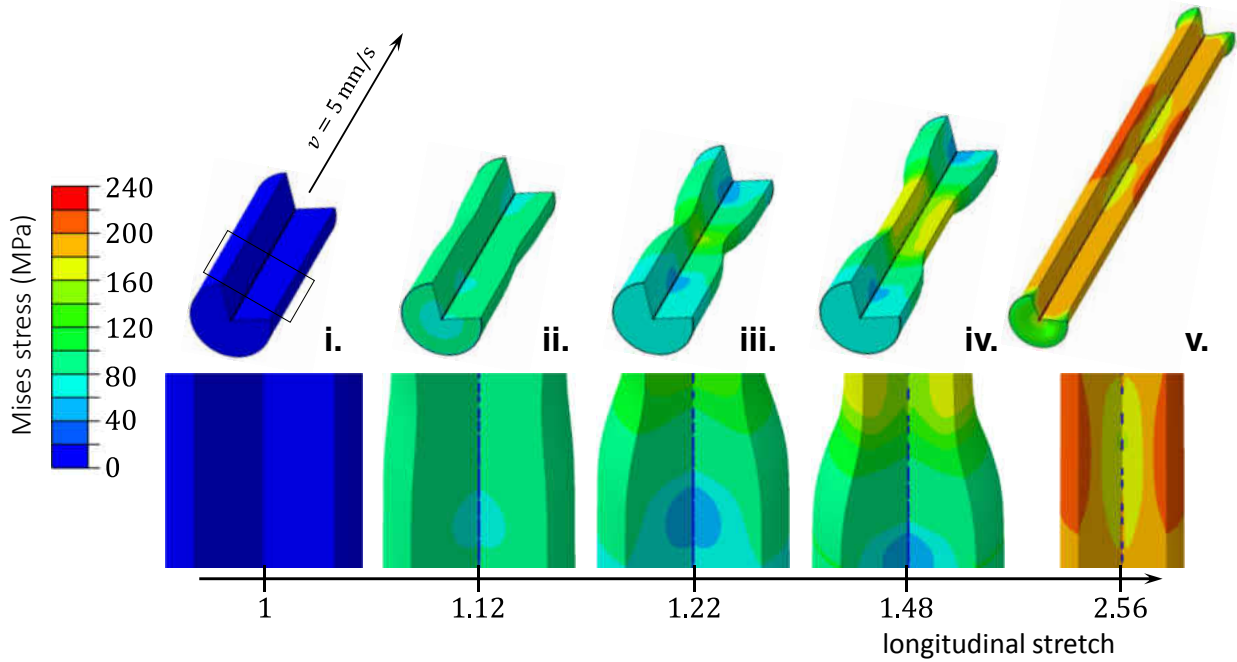
Figure 30: Finite element simulation of necking propagation of PES matrix and fracture into pieces of As_2Se_3 core under tensile loading with constant speed.

Table 4: Geometry comparison of fractured core pieces between numerical simulations and test measurement

Core Material	L/D ratio (simulation)	Standard deviation (simulation)	L/D ratio (test)
As_2Se_3	5.57	1.38	6
Si	36.6	5.89	32.5

4.3.2 Thin-film Composite

Extrusion and mirror methods are used to visualize the results in 3D. The width of the fragmented strips in the cold-drawing simulation is 7.55 µm, which is in good agreement with the measurements.
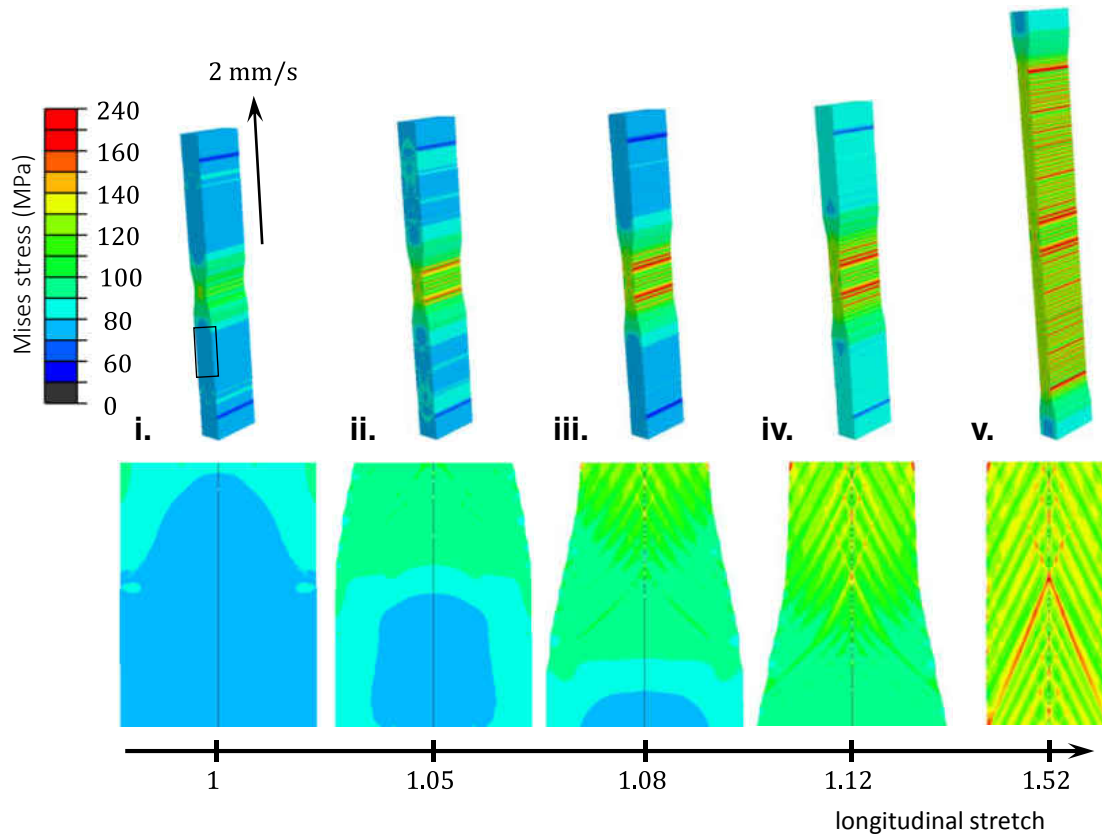
Figure 31: Finite element simulation of thin film composite

In the finite element simulations, the fragmentation along necking propagation are duplicated well. In step i, a minor displacement is applied and therefore some random crack could be found in the core. As the upper grip goes further, necking is found in step ii and the core in the center breaks into segments uniformly. Necking continues in step iii and iv and the distance between

segments enlarges due to the stretch from the cladding. The step v shows that necking fully propagates and the whole fiber uniformly breaks into segments.

CHAPTER 5 POLYMER MATRIX COMPOSITES

5.1 Theoretical Modeling

This section presents the constitutive model formulation which comprises of elasticity, plasticity, damage accumulation and fracture propagation. Extensive test results on PMCs are used to calibrate and validate the proposed model.

5.1.1 Elasticity

In elastic range, the stress is a linear function of strain. The orthotropic elastic material law that relates the stress to strain is written as

$$\boldsymbol{\sigma} = \boldsymbol{C}\boldsymbol{\varepsilon} \tag{13}$$

Where $\boldsymbol{\sigma}^T = [\sigma_{11} \quad \sigma_{22} \quad \sigma_{33} \quad \sigma_{12} \quad \sigma_{23} \quad \sigma_{31}]$, $\boldsymbol{\varepsilon}^T = [\varepsilon_{11} \quad \varepsilon_{22} \quad \varepsilon_{33} \quad \varepsilon_{12} \quad \varepsilon_{23} \quad \varepsilon_{31}]$ and

$$\boldsymbol{C} = \begin{bmatrix} c_{11} & c_{12} & c_{13} & & & \\ c_{12} & c_{22} & c_{23} & & & \\ c_{13} & c_{23} & c_{33} & & & \\ & & & c_{44} & & \\ & & & & c_{55} & \\ & & & & & c_{66} \end{bmatrix} \tag{14}$$

The engineering constants (Young's modulus E, Poisson's ratio v, and shear modulus μ) are related to the components of the stiffness tensor by

$$c_{11} = E_1(1 - v_{23}v_{32})\gamma, c_{22} = E_2(1 - v_{13}v_{31})\gamma, c_{33} = E_3(1 - v_{12}v_{21})\gamma \tag{15}$$

$$c_{12} = E_1(v_{21} + v_{31}v_{23})\gamma = E_2(v_{12} + v_{32}v_{13})\gamma$$

$$c_{13} = E_1(v_{31} + v_{21}v_{32})\gamma = E_3(v_{13} + v_{12}v_{23})\gamma$$

$$c_{23} = E_2(v_{32} + v_{12}v_{31})\gamma = E_3(v_{23} + v_{21}v_{13})\gamma$$

$$c_{44} = \mu_{12}, c_{55} = \mu_{23}, c_{66} = \mu_{31}$$

$$\gamma = \frac{1}{1 - \nu_{12}\nu_{21} - \nu_{23}\nu_{32} - \nu_{31}\nu_{13} - 2\nu_{21}\nu_{32}\nu_{13}}$$

To ensure the stiffness matrix to be symmetric, the generalized Poisson's ratios satisfy $\nu_{ij}/E_i = \nu_{ji}/E_j$.

In this paper, we define the direction 1 as the fiber direction. In addition, a new stress state parameter describing loading conditions for unidirectional fiber is defined as

$$\psi = \frac{\sigma_1}{\bar{\sigma}_{vm}}, \tag{16}$$

where σ_1 is the stress along fiber direction and $\bar{\sigma}_{vm}$ is von-Mises equivalent stress. In this way, ψ can be used to distinguish different loading conditions including tension dominated, compression dominated and shear dominated loading conditions, as shown in Figure 32.
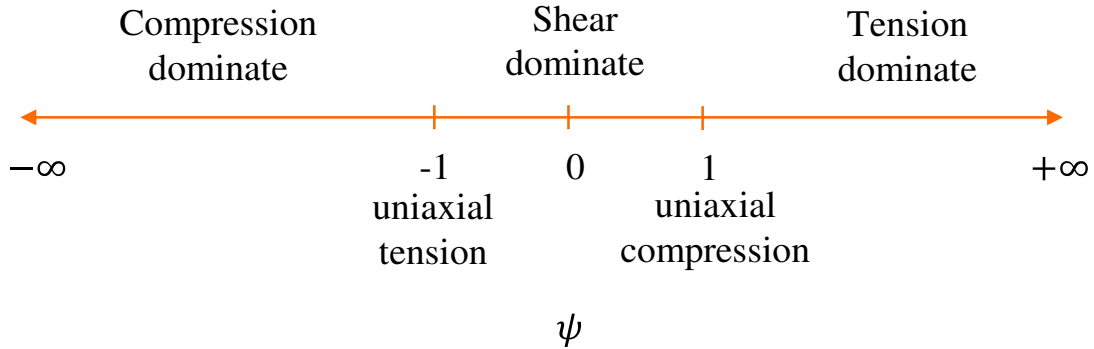
Figure 32: Parameter ψ describing different loading conditions of unidirectional fiber composite

As shown in the experimental section, tension and compression tests along the fiber direction have different Young's modulus. This unsymmetrical elasticity brings difficulty in modeling the behavior of PMCs. An elastic model considering the unsymmetrical elasticity is proposed as follows.

$$E_1(\psi) = e_\circ + \frac{e_d}{1 + e^{-e_c\psi}}, \tag{17}$$

where E_1 is the Young's modulus in fiber direction. e_0 and e_d are two parameters determining the upper and lower bounds of $E_1(\psi)$, and e_c is a parameter to fit the transition from tension to compression loading conditions. With parameters $e_0 = 70521 MPa$, $e_c = 21.42$ and $e_d = 31160 MPa$, an example of Young's modulus's dependency on ψ is shown in Figure 33. The proposed elastic model clearly distinguishes between the tension and compression tests with a smooth transition through the shear dominated loading conditions.
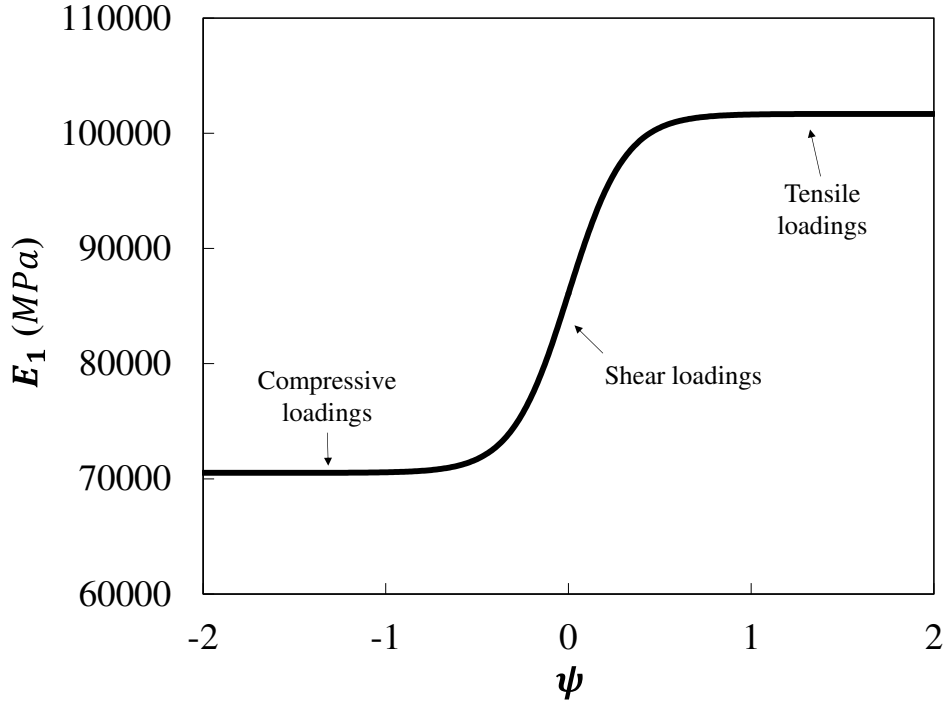
Figure 33: Relationship between Young's modulus along fiber direction (E_1) and the stress state parameter (ψ)

5.1.2 Yield locus and Failure initiation locus

One can see that non-linear or unrecoverable deformation (called yield in this paper) before total failure has been observed in almost all the experiments presented here except for uniaxial

compression along fiber direction. This non-linear or unrecoverable deformation phenomenon was also reported by Lonetti, Barbero, Zinno, and Greco (2004).An anisotropic yield function in the form of Tsai-Wu failure criterion (Tsai & Wu, 1971) is adopted in this paper.

$$f_y(\sigma_{ij}) = f_1\sigma_1 + f_2\sigma_2 + f_3\sigma_3 + f_4\sigma_4 + f_5\sigma_5 + f_6\sigma_6 + f_{11}\sigma_1^2 + f_{22}\sigma_2^2 \qquad (18)$$

$$+ f_{33}\sigma_3^2 + f_{44}\sigma_4^2 + f_{55}\sigma_5^2 + f_{66}\sigma_5^2 + 2f_{12}\sigma_1\sigma_2 + 2f_{13}\sigma_1\sigma_3 + 2f_{23}\sigma_2\sigma_3$$

where subscript 1 refers to the fiber direction while 2 and 3 refer to the transverse directions. f_i and f_{ij} are parameters to be determined from the yield or non-linear initiation stresses. The interaction parameter f_{12} takes the form of Mises-Hencky criterion (Tsai & Hahn, 1981). If the yield stress in tension (Y_T), compression (Y_C) and shear (Y_S) from directions 1, 2, and 3 are known, then the model coefficients can be determined as follows.

$$f_1 = \frac{1}{Y_{T1}} - \frac{1}{Y_{C1}}, f_2 = \frac{1}{Y_{T2}} - \frac{1}{Y_{C2}}, f_3 = \frac{1}{Y_{T3}} - \frac{1}{Y_{C3}}, f_4 = f_5 = f_6 = 0 \qquad (19)$$

$$f_{11} = \frac{1}{Y_{T1}Y_{C1}}, f_{22} = \frac{1}{Y_{T2}Y_{C2}}, f_{33} = \frac{1}{Y_{T3}Y_{C3}}, f_{44} = \frac{1}{Y_{S23}^2}, f_{55} = \frac{1}{Y_{S31}^2}, f_{66} = \frac{1}{Y_{S12}^2}$$

$$f_{12} = -\frac{1}{2\sqrt{Y_{T1}Y_{C1}Y_{T2}Y_{C2}}}$$

Meanwhile, the Tsai-Wu criterion was also used to describe the failure initiation locus for PMCs which takes the form of

$$F_f(\sigma_{ij}) = F_1\sigma_1 + F_2\sigma_2 + F_3\sigma_3 + F_4\sigma_4 + F_5\sigma_5 + F_6\sigma_6 + F_{11}\sigma_1^2 + F_{22}\sigma_2^2 \qquad (20)$$

$$+ F_{33}\sigma_3^2 + F_{44}\sigma_4^2 + F_{55}\sigma_5^2 + F_{66}\sigma_5^2 + 2F_{12}\sigma_1\sigma_2 + 2F_{13}\sigma_1\sigma_3 + 2F_{23}\sigma_2\sigma_3.$$

F_i and F_{ij} are free parameters to be determined from the fracture data points using Eq. (20). The failure initiation stresses in tension (F_T), compression (F_C) and shear (F_S) from directions 1, 2, and 3 are needed to calibrate the model.

$$F_1 = \frac{1}{F_{T1}} - \frac{1}{F_{C1}}, F_2 = \frac{1}{F_{T2}} - \frac{1}{F_{C2}}, F_3 = \frac{1}{F_{T3}} - \frac{1}{F_{C3}}, F_4 = F_5 = F_6 = 0 \qquad (21)$$

$$F_{11} = \frac{1}{F_{T1}F_{C1}}, F_{22} = \frac{1}{F_{T2}F_{C2}}, F_{33} = \frac{1}{F_{T3}F_{C3}}, F_{44} = \frac{1}{F_{S23}^2}; F_{55} = \frac{1}{F_{S31}^2}; F_{66}$$

$$= \frac{1}{F_{S12}^2}$$

$$F_{12} = -\frac{1}{2\sqrt{F_{T1}F_{C1}F_{T2}F_{C2}}}$$

Based on the current test results, the initial yield and total failure stresses compared with model prediction are shown in Figure 34. It is noticed that the failure initiation locus is within the range between initial yield locus and total failure data points since there are still a stage of fracture propagation. One may notice that in the σ_{xy}-σ_x stress space, the fracture data points in first quadrant are far outside the corresponding fracture locus. This can be explained as follows. For these shear combined with tension loading conditions, shear strength is enlarged due to the decomposed force component from fiber tension force. It is shown in Figure 35 that the shear strength is calculated from measured horizontal force which includes force component decomposed from total force along fiber direction. In this way, the yield and failure loci are somewhat conservative in the first quadrant of σ_{xy}-σ_x stress space in order to better describe the material behavior. The final yield and failure initiation loci will be determined through iterations of FE simulations.
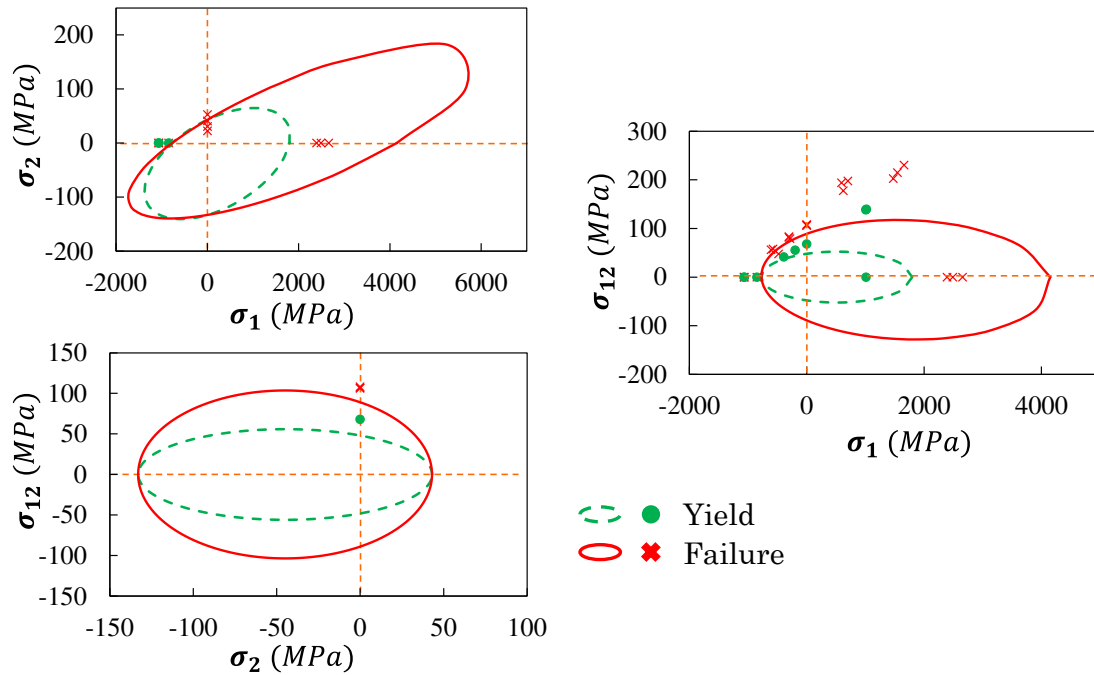
Figure 34: Comparison between initial yield and total failure data points from tests and model predicted initial yield locus and failure initiation loci
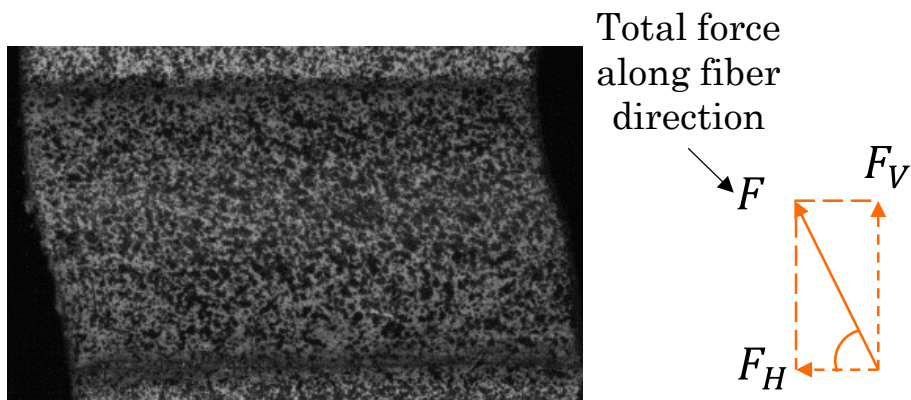
Figure 35: Force in fiber direction (F) can be decomposed into horizontal force component (F_H) and vertical force component (F_V)

5.1.3 Plastic flow rule

An associated flow rule (AFR) is assumed for the PMCs materials undergoing inelastic deformation observed in the tests. An anisotropic plastic potential takes the following form.

$$f(\sigma_{ij}) = f_y(\sigma_{ij}) - \hat{\sigma}(\bar{\varepsilon}_p) = \bar{\sigma}_{TW} - \hat{\sigma}_{TW}(\bar{\varepsilon}_p) = 0 \qquad (22)$$

$\bar{\sigma}_{TW} = f_y(\sigma_{ij})$ is the Tsai-Wu yield function shown in Eq. (18) or called Tsai-Wu equivalent

stress hereinafter. In this way, the initial yield point of the material will naturally start from

$\bar{\sigma}_{TW} = 1$ according to the f_{ij} coefficients in $f_y(\sigma_{ij})$. Material strain hardening is assumed to

follow isotropic Swift power hardening law, which reads $\hat{\sigma}_{TW} = A(\bar{\varepsilon}_{TW}^p + \varepsilon_0)^n$. Here $\bar{\sigma}_{TW}$ and

$\bar{\varepsilon}_{TW}^p$ are normalized Tsai-Wu yield stress and work conjugate Tsai-Wu equivalent plastic strain

defined by the yield criteria. A, ε_0 and n are determined by the stress-strain curve obtained from

corresponding tests.

According to AFR, the incremental plastic strains can be expressed as

$$d\boldsymbol{\varepsilon}_p = d\lambda \frac{\partial f}{\partial \boldsymbol{\sigma}}, \qquad (23)$$

where $d\lambda$ is the proportionality factor.

The increment of plastic work per unit volume can be obtained by

$$dW^p = \sigma_{ij}d\varepsilon_{ij}^p = \bar{\sigma}_{TW}d\bar{\varepsilon}_{TW}^p \qquad (24)$$

Therefore, the effective plastic strain increment can be expressed as follows:

$$d\bar{\varepsilon}_{TW}^p = \frac{\sigma_{ij}d\varepsilon_{ij}^p}{\bar{\sigma}_{TW}} \qquad (25)$$

As observed from the experiments, vertical direction force-displacement curves show little

plasticity but polymer matrix provides the major source of plasticity. So, the Swift power

hardening law will be calibrated from the pure shear test. See Figure 36. Work conjugate stress

and strain are used in the data processing. Therefore, the "equivalent stress" start from unity and

the "equivalent strain" are relatively larger than traditional ways. One can find that the curve

fitting does not exactly follow the experimental data. Here the experimental curve is nominal

since it is calculated from a notched plate where stress is not very uniform on the notched area.

The curve is provided as a benchmark for the initial hardening curve fitting. The illustrated curve

is an optimized result through iterative FE simulations to achieve the best correlation in force-

displacement responses.
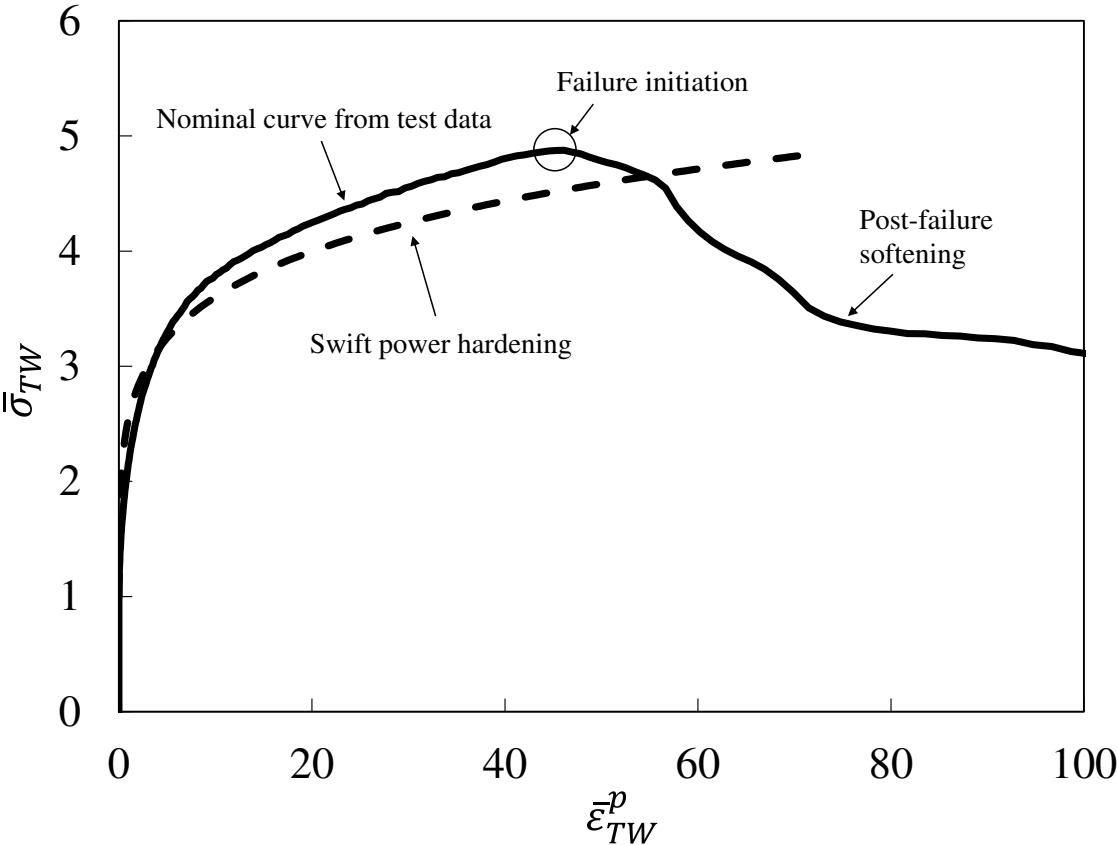
Figure 36: Curve fitting of power hardening law for the pure shear loading condition

5.1.4 Damage accumulation and material post-failure softening

When Tsai-Wu failure criterion is not reached, damage indicator (D) is set to be equal to the normalized Tsai-Wu failure stress (Eq. (20)). Therefore, the material damage evolution is defined as

$$D = F(\sigma_{ij}), \qquad if \; D \leq 1. \tag{26}$$

When damage indicator $D < 1$, the material is intact with no damage. When $D = 1$, it indicates that failure initiates as "equivalent stress" reaches the critical value 1. Typically the material exhibits both elastic and plastic behaviors before failure initiates $(D \leq 1)$. However, sometimes failure initiation could occur before material yielding and therefore material plastic strain hardening could vanish, under some loading conditions like uniaxial compression for this material.

After failure initiation, the damage accumulation is defined by an incremental form:

$$dD = \frac{L d\tilde{\sigma}_{TW} \bar{\varepsilon}^{p}_{TW}}{G_c(\psi)}. \tag{27}$$

Here L is the characteristic length of a finite element in the simulation. $\tilde{\sigma}_{TW}$ is Tsai-Wu equivalent stress that incorporates the effect of material post-failure softening, which is different from $\bar{\sigma}_{TW}$, the equivalent stress from the hardening model. $d\bar{\varepsilon}^{p}_{TW}$ is the incremental work conjugate plastic strain. $G_c(\psi)$ is the toughness or critical strain energy release rate at fracture which is also a function of loading condition ψ. $d\tilde{\sigma}_{TW} \bar{\varepsilon}^{p}_{TW}$ is the plastic strain energy incremental per unit volume, and $L d\tilde{\sigma}_{TW} \bar{\varepsilon}^{p}_{TW}$ represents strain energy incremental per unit surface.

As stated earlier, carbon fiber composite material shows brittle failure in compressive loading conditions and ductile failure in tensile and shear dominated loading conditions. This feature is characterized by applying a loading condition dependent fracture toughness $G_c(\psi)$, which is defined by

$$G_c(\psi) = G_{Fc0} + \frac{G_{Fc1}}{1 + e^{G_{Fc2}(\psi + \psi_{G0})}} \tag{28}$$

where G_{Fc0}, G_{Fc1}, G_{Fc2} and ψ_{G0} are model parameters for describing the brittle-ductile fracture transition. Parameters were obtained by calibrating each tested loading condition and the results are shown in Figure 37. The negative range of $\psi < -1$ corresponds to the brittle failure modes in the compression dominated loading conditions. The positive range of $\psi > 1$ corresponds to the ductile failure modes in the tension dominated loading conditions. The values in the range of $-1 \leq \psi \leq 1$ correspond to the shear dominated loading conditions which is also ductile. The exact transition area needs to be determined from iterations of simulations or more test data.
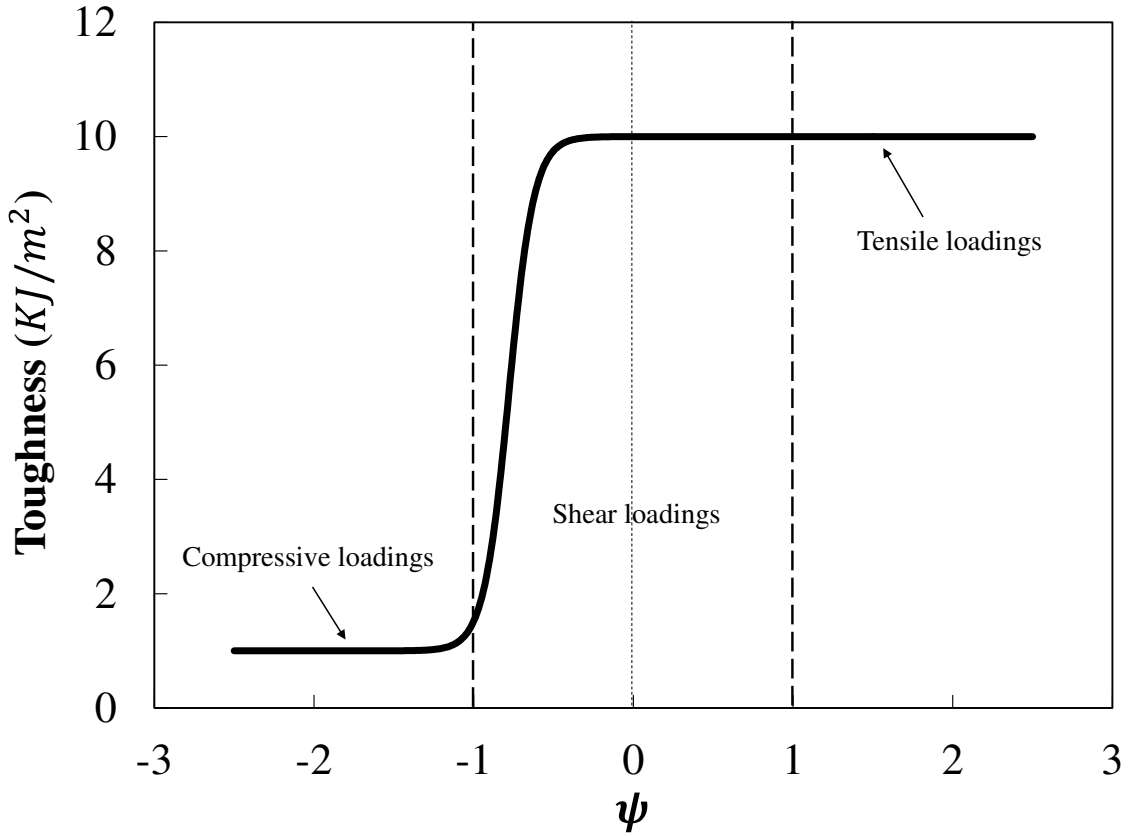
Figure 37: Material fracture toughness versus loading condition parameter ψ

It is assumed that material softening starts after failure initiation ($D > 1$). This is an important aspect which affects the prediction for failure stress, failure strain and failure modes (Donadon et al., 2009; Matzenmiller et al., 1995). A material post-failure softening model is postulated in the following expression:

$$\tilde{\sigma}_{TW} = \bar{\sigma}_{TW}[1 - Se(\psi)(D-1)^{S_m}], \qquad (if\ 1 < D \leq 2) \qquad (29)$$

where $\bar{\sigma}_{TW}$ is the Tsai-Wu equivalent stress including strain hardening. Therefore post-failure equivalent stress takes the product of both hardening $\bar{\sigma}_{TW}$ and softening coefficient [$1 - Se(\psi)(D-1)^{S_m}$]. $Se(\psi)$ is a parameter to control the ultimate failure stress which also depends on loading condition ψ, and S_m is a parameter to determine stress softening rate with respect to

damage accumulation indicator D. The material post-failure softening coefficient $[1 - Se(\psi)(D-1)^{Sm}]$ is demonstrated in Figure 38. In order to distinguish the softening between different loading conditions, the parameter $Se(\psi)$ takes the following form.

$$Se(\psi) = s_{\circ} - \frac{s_d}{1 + e^{-s_c(|\psi|+\psi_{S0})}} \tag{30}$$

The relationship between $Se(\psi)$ and loading condition parameter ψ is illustrated in Figure 39. At shear dominated loading conditions (around $\psi = 0$), $Se(\psi) = 1$ which gives a sharp drop in the softened equivalent stress. This was found in the pure shear tests. For other loading conditions, the drop is not that sharp and therefore $Se(\psi)$ takes a smaller number around 0.65. Note that these softening parameters will be calibrated through several iterations of FE simulations.
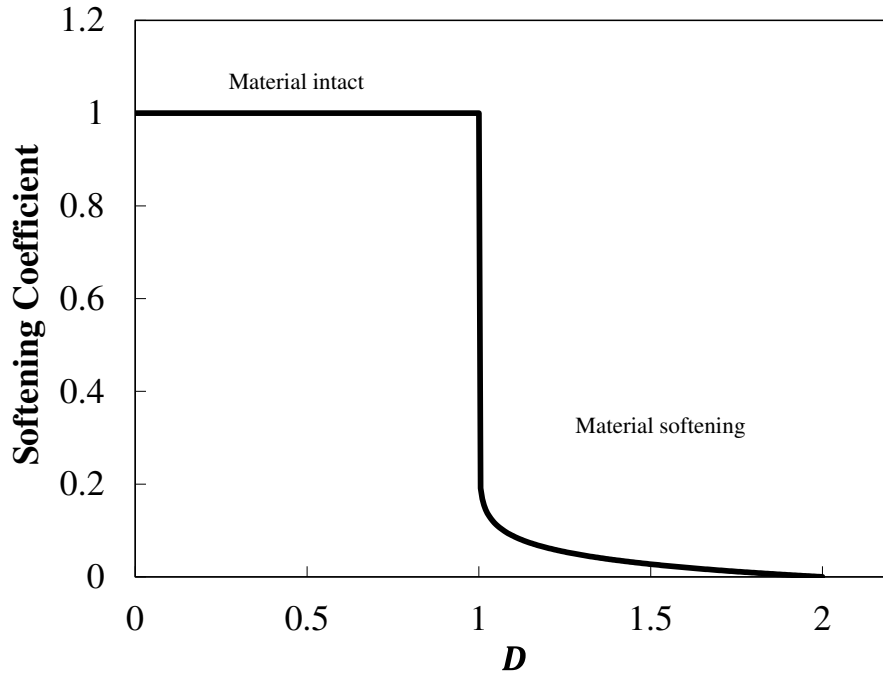
Figure 38: Material post-failure softening evolution curve (set $Se(\psi) = 1, S_m = 0.08$)
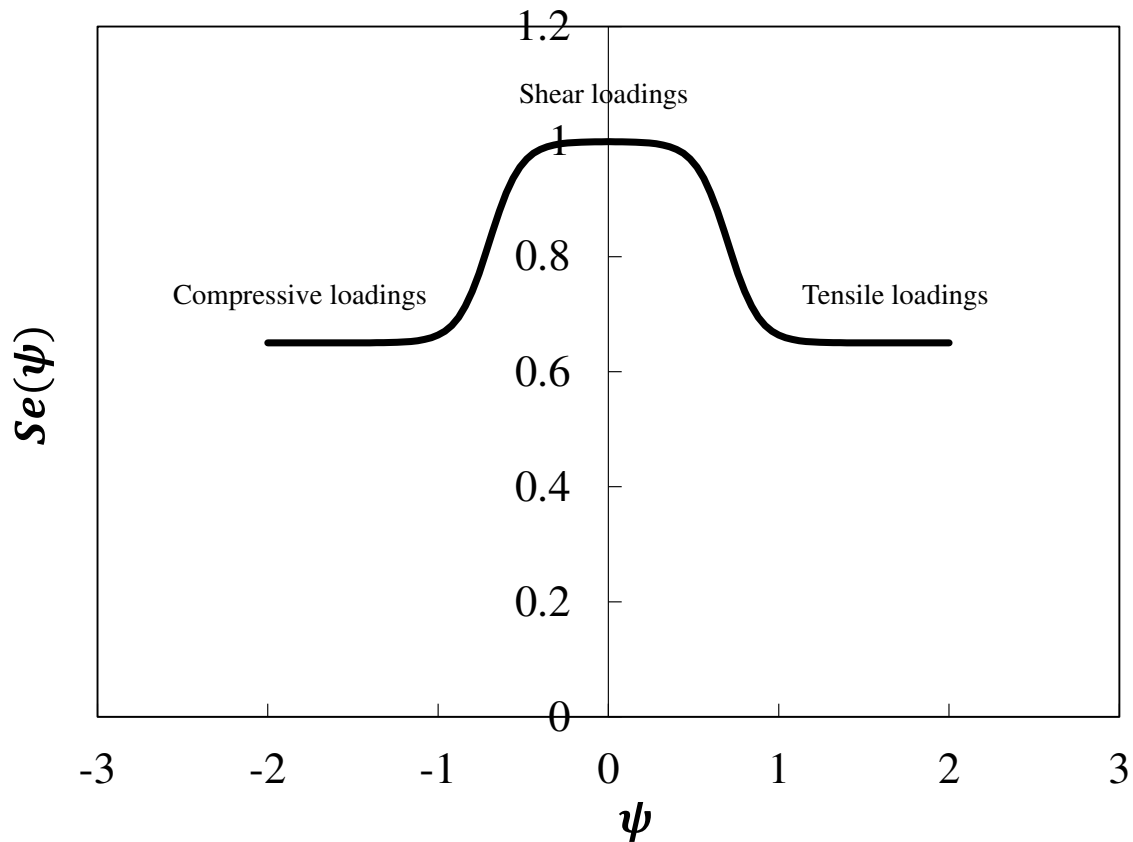
Figure 39: Relationship between $Se(\psi)$ and loading condition parameter ψ

5.1.5 Cohesive surface

Delamination was observed in some of the loading conditions like simple tension and tension combined with shear tests. This special damage feature was due to the notch design in the specimens and it will be modeled as cohesive surface failure in finite element simulations using ABAQUS/Explicit (ABAQUS, 2011).

The surface-based cohesive behavior consists of a linear elastic traction-separation behavior, damage initiation, and damage evolution which are explained in details as follows.

The elastic behavior is written in terms of an elastic constitutive matrix that relates the normal and shear stresses to the normal and shear separations across the interface. The nominal traction

stress vector $\boldsymbol{t}$, consists of three components t_n, t_s and t_t, which represent the normal and the two shear tractions, respectively. The corresponding separations are denoted by δ_n, δ_s and δ_t. The elastic behavior can then be written as

$$\boldsymbol{t} = \begin{Bmatrix} t_n \\ t_s \\ t_t \end{Bmatrix} = \begin{bmatrix} K_{nn} & & \\ & K_{ss} & \\ & & K_{tt} \end{bmatrix} \begin{Bmatrix} \delta_n \\ \delta_s \\ \delta_t \end{Bmatrix} = \boldsymbol{K\delta} \tag{31}$$

Here, an uncoupled traction-separation feature is assigned to the linear elastic behavior. In this way, the normal and tangential stiffness components will not be coupled: pure normal separation by itself does not give rise to cohesive forces in the shear directions and *vice versa.*

A maximum stress criterion is utilized to model damage initiation. Damage is assumed to initiate when the maximum contact stress ratio reaches a value of one which has the following form.

$$\max\left\{ \frac{t_n}{t_n^o}, \frac{t_s}{t_s^o}, \frac{t_t}{t_t^o} \right\} = 1 \tag{32}$$

After damage initiation, a linear damage evolution takes place on the cohesive surface. A damage indicator of the cohesive surface D_s is postulated in the following form,

$$D_s = \frac{\delta_m^f(\delta_m^{max} - \delta_m^o)}{\delta_m^{max}(\delta_m^f - \delta_m^o)}. \tag{33}$$

δ_m^{max} refers to the maximum value of the effective separation attained during the loading history. δ_m^o refers to the initial value of the effective separation at the damage initiation point. δ_m^f is the value of the effective separation at current time step. Here the effective separation is defined as

$$\delta_m = \sqrt{\langle\delta_n\rangle^2 + \delta_s^2 + \delta_t^2}, \tag{34}$$

where $\langle\delta_n\rangle$ is the Macaulay bracket which renders only positive value of δ_n.

With the linear elastic traction-separation behavior, damage initiation and linear damage evolution, a typical traction-separation response with a failure mechanism is shown in Figure 40.
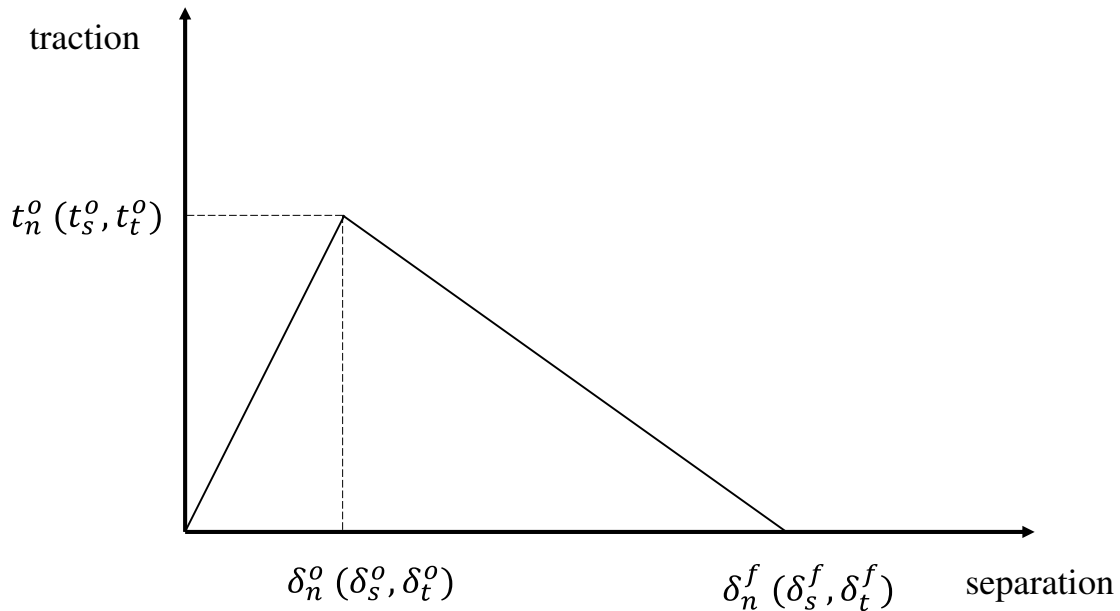
Figure 40: A typical traction-separation response of cohesive surface

<u>5.2</u> Model calibration procedure

Finite element simulations for all loading conditions were performed using ABAQUS/Explicit. The proposed material model was implemented as a user material subroutine (VUMAT). The phenomena of crack initiation and propagation were simulated using an element deletion technique for the continuum model and an ABAQUS built-in cohesive surface technique for delamination. Two types of finite element models with or without cohesive surfaces are shown in Figure 41. Specimens were modeled using C3D8R solid elements. The attached aluminum plates on both shoulder sides of carbon fiber composite specimen are modelled as a linear elastic material.

For the single part model, the PMCs specimen is treated as a homogenized material with four aluminum plates attached to both sides of top and bottom. Boundary conditions are applied to the outer surfaces of aluminum plates. In the case of carbon fiber composite with cohesive surfaces model, the specimen is treated as five parts with four aluminum plates attached to both sides. The five parts of PMCs are attached together using the cohesive surface feature. Boundary conditions are applied to the outer surfaces of aluminum plates, too.

Single part   Cohesive surfaces   Multiple parts
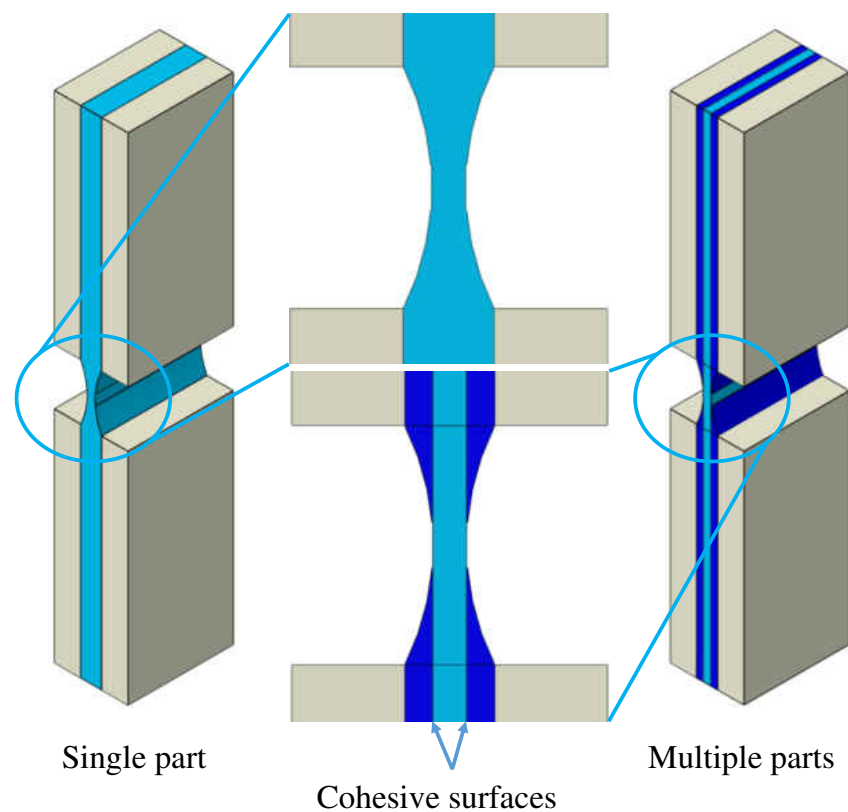
Figure 41: Finite element models for unidirectional carbon fiber composite specimen (a) Single part model (b) Multiple parts with cohesive surfaces

The model calibration procedures are summarized as follows.

1. The first step was to calibraste the elasticity model ($E_1(\psi)$) and other constants in stiffness tensor C). Tested Young's moduli under both uniaxial tension and uniaxial compression were

correlated with the model ones by adjusting the parameter e_0 and e_d. The main consideration is to make sure the Young's moduli under tension ($\psi > 1$) and compression ($\psi < 1$) dominated conditions to fit with the correspoinding values. Iterations would be required to fit the other loading conditions like tension or compression combined with shear by modifying the transition parameter e_c.

2. Secondly, the yield and failure initiation loci ($f_y(\sigma_{ij})$ and $F_f(\sigma_{ij})$) were fitted through correlating force-displacement curves and images captured during tests. For the yield locus, it will be fitted to the material nonlinearity initiation point. For the ones without material nonliearity, the material nonliear initiation point will be the failure initiation point like the uniaxial compressive loading. For the failure initiation point, it is simple for compression and combined compression-shear conditions. These failure inititaion points are also the total failure points since they show linear elasticity with brittle failure modes. As for the shear loading condition, the maximum load point is set as the failure initiation point. For the loading conditions incorporating tensile loads, shear-induced failure or delamination will take place and hence failure points will be taken as reference for failure locus.

3. Thirdly, the strain hardening model based on Tsai-Wu equivalent stress ($\hat{\sigma}_{TW}(\bar{\varepsilon}^p_{TW})$) was fitted using tested stress-strain data under shear. The selection of data was based on the occurrence of plastic behavior under this loading condition. Usually, carbon fiber does not show plasticity and polymer matrix will show plasticity. Shear loading condition helped to reveal the matrix plasticity and therefore the curve fitting of material hardening was based on it. Modifications on the hardening model would be required to fit the other loading conditions.

4. Fouthly, the toughness function $(G_c(\psi))$ was calibrated based on areas under the tested stress-strain (or force-displacement) curves under different loading conditions. This was to assure the correlation of the ultimate fracture displacement. The other purpose was to simulate the brittle failure in compression dominated loading condisions and ductile failure in tension dominated loading conditions.

5. The softening function $(\tilde{\sigma}_{TW})$ was calibrated by using the tested shear loading stress-strain curve to achieve the correct post-failure softening mode. As shown in the experimental results, shear tests have a long range of softening without total failure which brought difficulty in the softening calibration. A sharp softening was assigned to the softening model by setting $Se(\psi)$ to be around 1 in the shear dominated loading conditions $(-1 < \psi < 1)$. The softening function needs to be calibrated with toughness $(G_c(\psi)$, step 4) since they work together in the material failure behavior.

6. In addition, for the multiple parts model with cohesive surfaces, additional steps are needed to calibrate the stiffness matrix K, critical stress vector t and maximum effective separation δ_m^{max}. A simple uncoupled traction-separation feature is assigned to the cohesive surface. Since shear-induced failure/delamination is shown in the experiments, a critical shear stress component is the key parameter.

A set of fully calibrated model parameters for the PMCs materials is listed in Table 5. A flow chart of the above calibration process is illustrated in Figure 42.

Table 5: Calibrated material model parameters for numerical simulations (unit in MPa or unitless)

Elastic property	$E_1(e_0)$	E_2	E_3	ν_{12}	ν_{23}	ν_{13}	G_{12}	G_{23}
	70521	8217	8217	0.28	0.28	0.28	3720	3720
	G_{13}	e_c	e_d					
	3720	21.42	31160					
Yield criterion & Material hardening	Y_{T1}	Y_{C1}	Y_{T2}	Y_{C2}	Y_{S12}	A	ε_0	n
	1800	770	43	133	48	2.55	0.002	0.15
Failure criterion & Cohesive surface	F_{T1}	F_{C1}	F_{T2}	F_{C1}	F_{S12}	K_{ss}	t_s	δ_s^t
	4150	771	43	133	89	25000	99	0.015
Toughness & Material softening	G_{Fc0}	G_{Fc1}	G_{Fc2}	ψ_{G0}	S_m	S_c	S_d	ψ_{S0}
	10	-8.0	12.7	0.78	0.04	10.7	0.3	-0.6
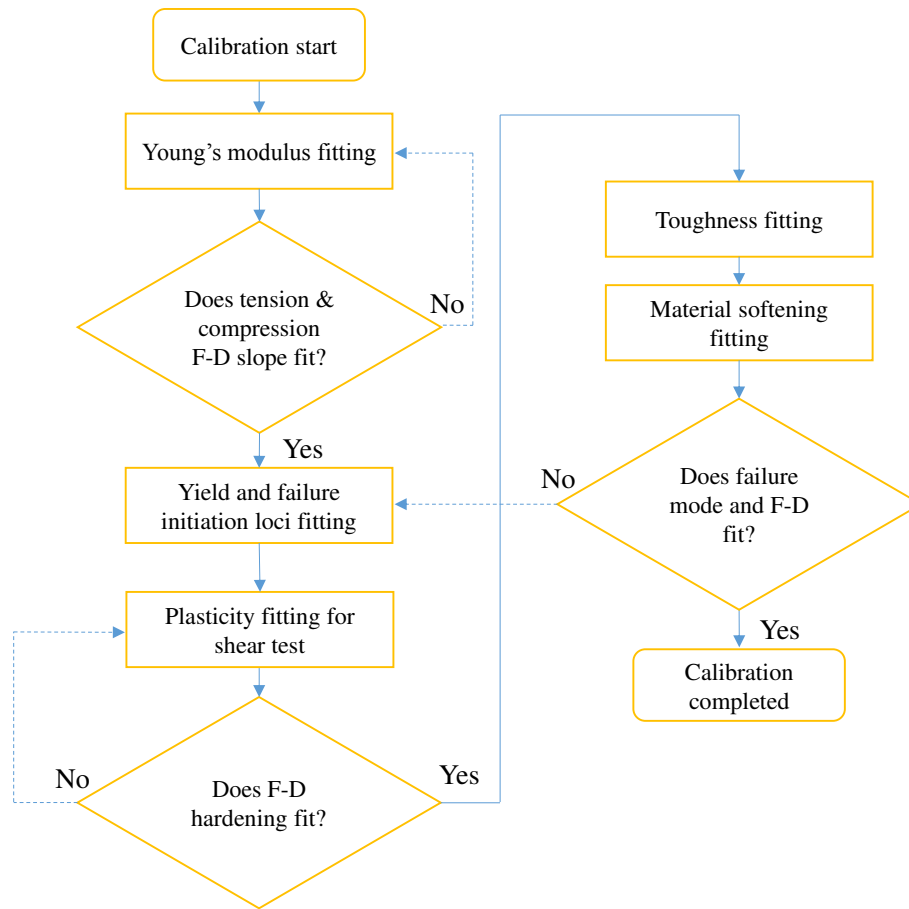
Figure 42: A flow chart of model calibration procedure. F-D stands for force-displacement curve.

5.3 Simulation results

The FE simulation results will be presented in two subsections. Tests without delamination failure were simulated using single part model. Other tests with delamination failure were simulated using multiple parts model with cohesive surface.

5.3.1 Simulations using single part model

5.3.1.1 Uniaxial compression

Figure 43 shows a photo of the uniaxial compression test of PMCs specimen compared to the FE simulation results. A brittle fracture due to local buckling failure was observed in both

experiment and simulation. A straight failure surface is well predicted by the simulation. In both experiments and simulation, the failure happens in a short time and the whole cross section breaks immediately. The elements shown in red are the most critical and close to fracture. The predicted force-displacement curve from simulation well duplicated the experimental ones in terms of both elasticity slope and ultimate fracture limit.
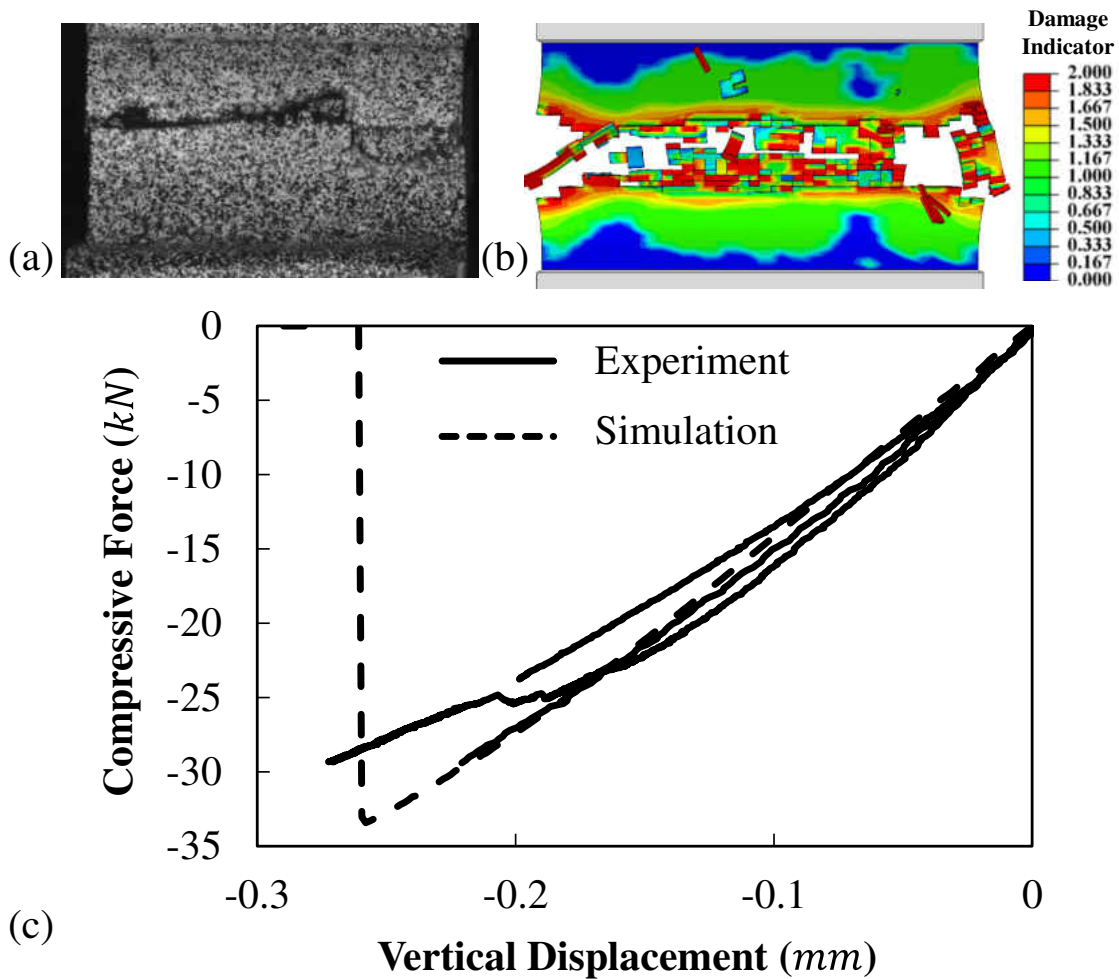
Figure 43: Comparison between FE simulations and test results of uniaxial compression test. Failure modes in (a) experiment (b) FE simulation; (c) Force–displacement curves of experiments and simulation

5.3.1.2 Compression + Shear with $\beta = -70°$

For the combined compression and shear loading with $\beta = -70°$, FE simulation well reproduced the experiment in regards to force-displacement evolution, fracture limit and failure modes. See Figure 44. Both the vertical and horizontal force-displacement curves from simulation follow the experimental ones. In fiber direction the material mostly exhibits elasticity while in transverse direction it shows nonlinearity due to the polymer matrix plasticity. The predicted ultimate fracture forces in both directions fit the experiments with a reasonable accuracy. The brittle failure mode and skew failure surfaces due to combined loading are also duplicated in simulation.
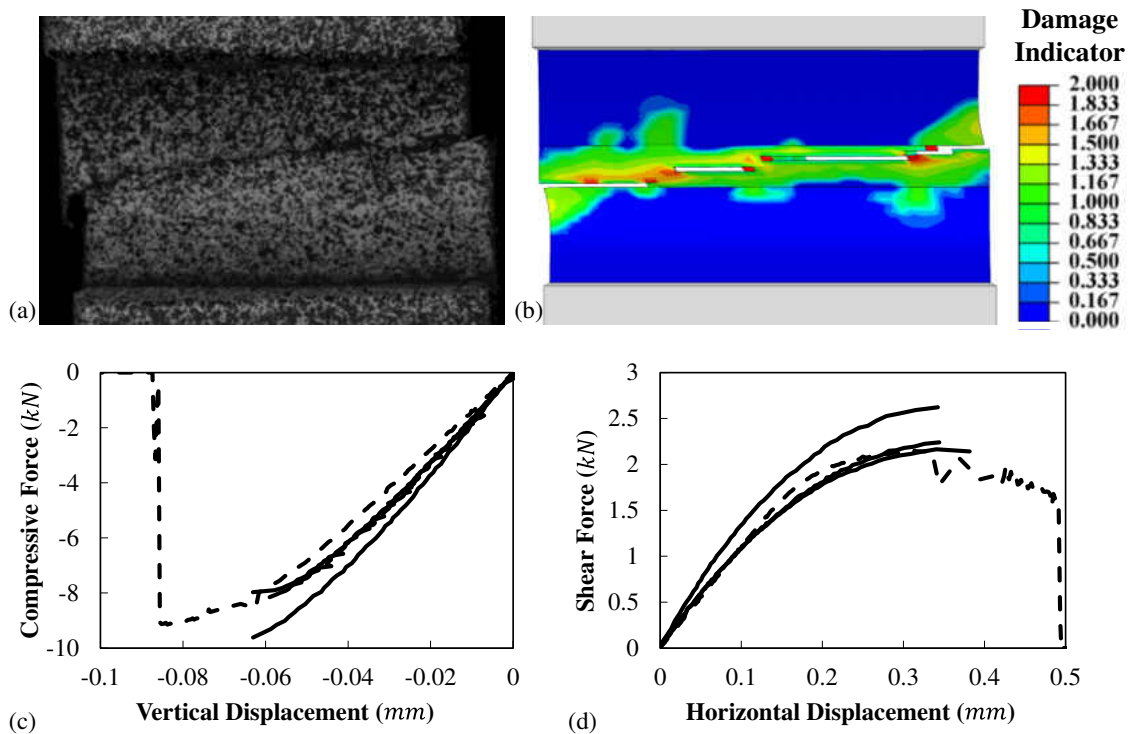
Figure 44: Comparison between numerical simulation and test results of combined compression and shear with $\beta = -70°$. Total failure in (a) experiment (b) simulation. Force-displacement curves of (c) vertical direction (d) horizontal direction. (Solid curve: experiment; Dashed curve: simulation)

5.3.1.3 Compression + Shear with $\beta = -45°$

For the combined compression-shear loading with $\beta = -45°$, it is similar to the test of $\beta = -70°$. The FE simulation duplicates the experiments well. Both force-displacement curves from simulation correlate well with the experimental ones. See Figure 45. Similarly, in fiber direction the material exhibits elasticity while in transverse direction shows nonlinearity. The fracture limits in both directions well fit the experiments. The brittle failure mode and skew failure surface are reproduced by simulation. For the above three types of tests with compressive loading investigated, brittle failure modes play a major role.
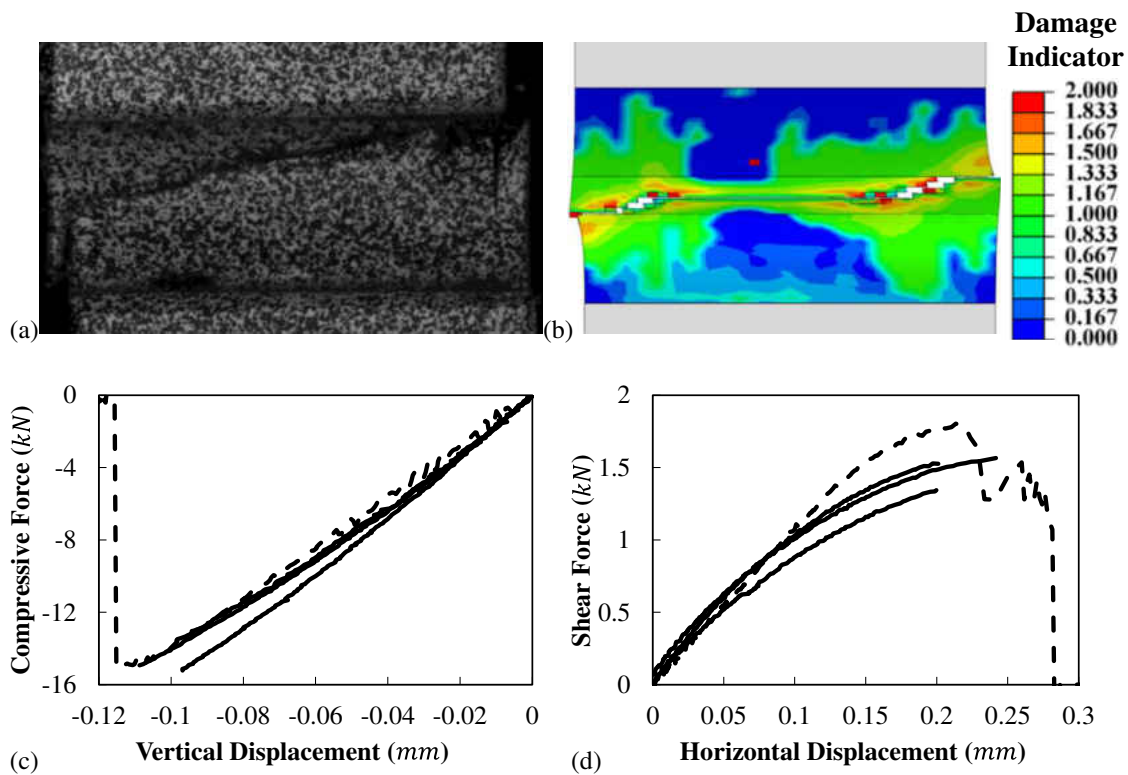
Figure 45: Comparison between numerical simulation and test results of combined compression and shear with $\beta = -45°$. Total failure in (a) experiment (b) simulation. Force-displacement curves of (c) vertical direction (d) horizontal direction. (Solid curve: experiment; Dashed curve: simulation)

<u>5.3.1.4 Shear</u>

For the shear loading condition, a significant amount of matrix plasticity is revealed. A comparison of the test and simulation results is shown in Figure 46. The matrix plasticity is well captured by the model, and the simulation results well duplicate this feature. The simulation used the same displacement control as the experimental one. The force-displacement curve fits well in the elastic and plastic hardening part. After the damage initiation point, the model exhibits a long range of material softening. Final failure is not shown in both experiment and simulation in the tests with displacement control. The material can still sustain some deformation and absorb more fracture energy. A deformation pattern comparison between experiment and simulation demonstrates the good predicting capability of the model in capturing the material plastic flow.
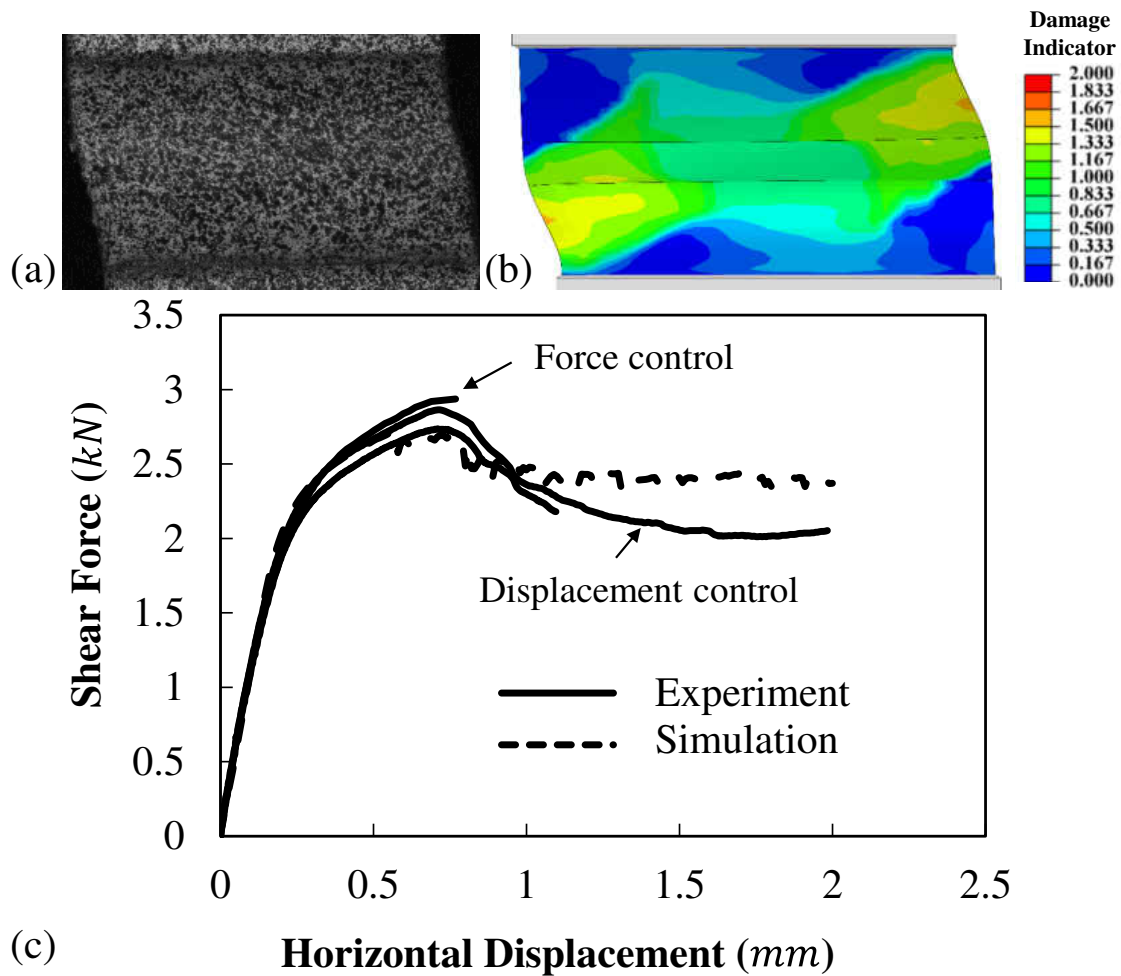
Figure 46: Comparison between numerical simulation and test results of the shear test. Final specimen configuration of (a) experiment (b) simulation; (c) Force-displacement curves of experiments and simulation

5.3.2 Simulations using multiple parts model with cohesive surfaces

As delamination feature is not shown in the loading conditions incorporating compression loads in the fiber direction, simulations with cohesive surface model are done for the loading conditions incorporating tensile loads. Good delamination features have been shown in the simulations.

5.3.2.1 Tension + Shear with $\beta = 70°$

For the combined tension and shear loading with $\beta = 70°$, FE simulation with the cohesive surface model well duplicates force-displacement curves. The key consideration lies in the failure features where delamination is clearly shown in the simulation as the loads gets larger and the matrix between fibers cannot sustain the shear stress. As the delamination propagates, the loads decreases in the simulation. Using the cohesive surface model, the simulation can well capture the elastic and material strain hardening behavior before delamination propagation. In addition, the delamination failure feature can be reproduced.
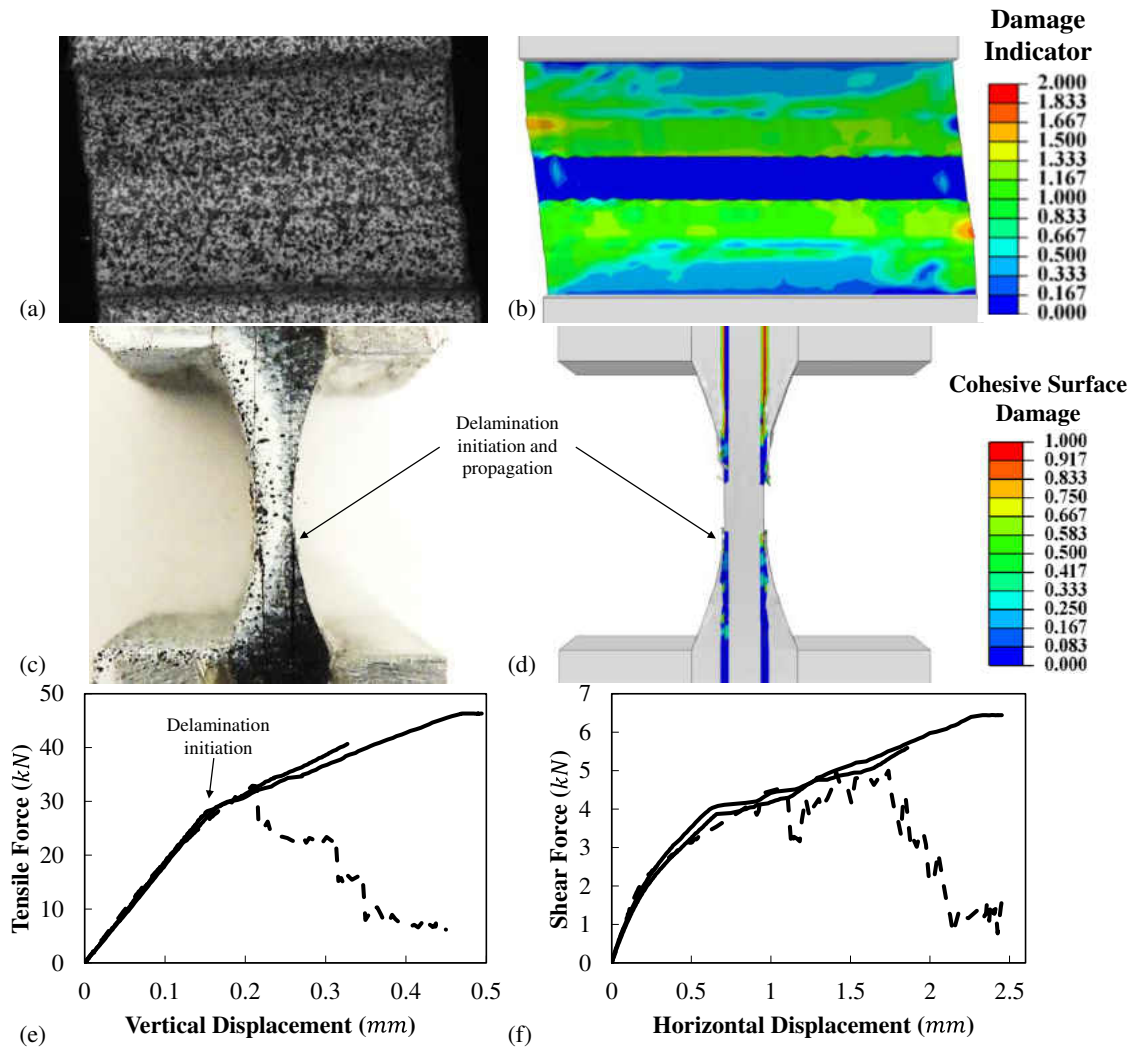
Figure 47: Comparison between numerical simulation and test results of combined tension and shear with $\beta = 70°$. Specimen configuration before severe delamination propagation of (a) experiment (b) simulation (contour showing damage indicator D, similarly hereinafter); Delamination failure feature (c) remaining after experiment (d) during simulation. Force-displacement curves of (e) vertical direction (f) horizontal direction. (Solid curve: experiment; Dashed curve: simulation)

5.3.2.2 Tension + Shear with $\beta = 80°$

For the combined tension and shear loading with $\beta = 80°$, FE simulations correlate well with the experiments in the force-displacement curve from both directions. In the vertical direction, the simulation reproduces the reverse curve from the experiment. In the horizontal direction, the

force-displacement curve shows an elastic-plastic trend similar to the experiments. Experiments shows delamination as the force in the horizontal direction gets large. This failure feature can also be reproduced by the model with cohesive surface.
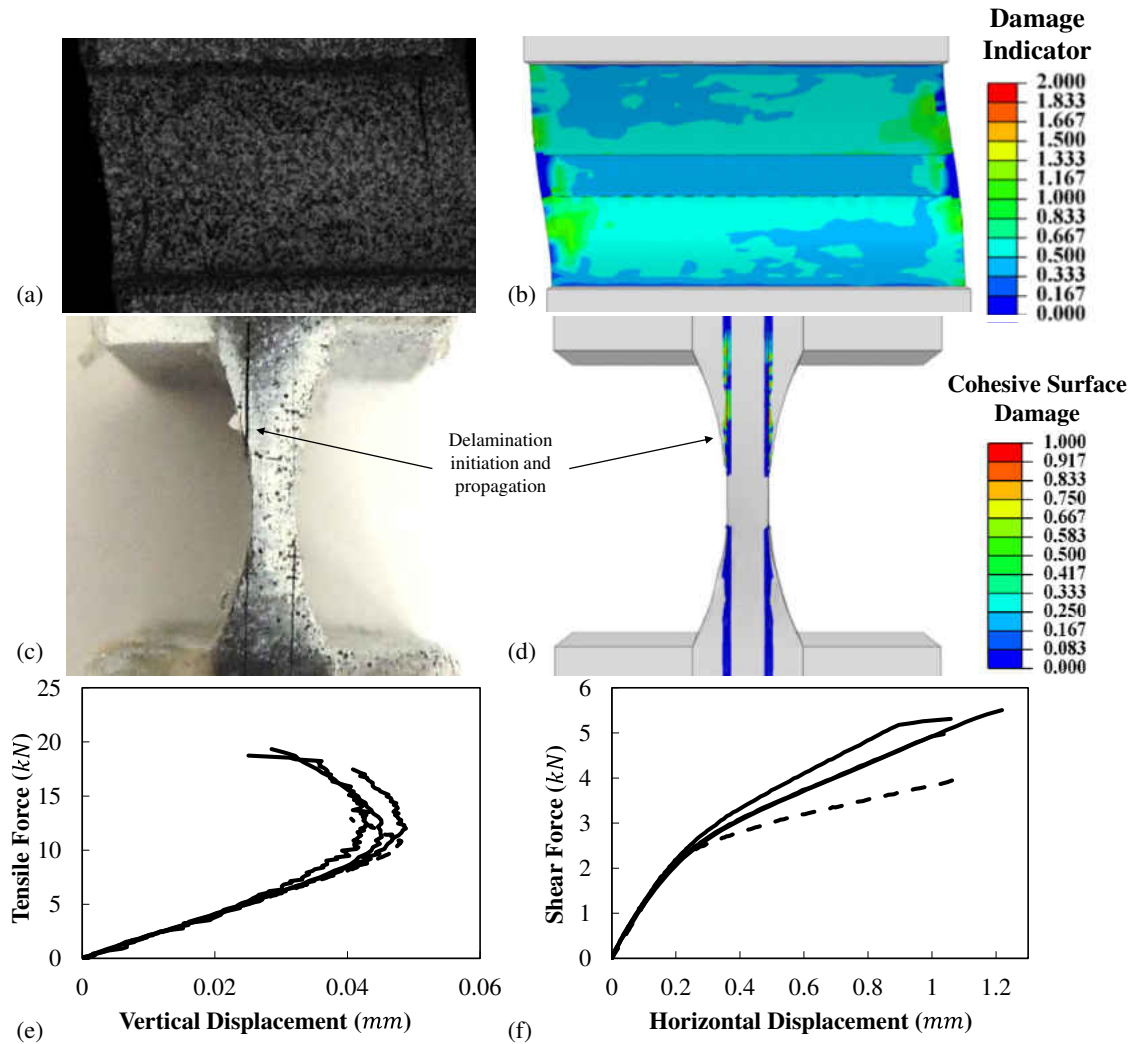
Figure 48: Comparison between numerical simulation and test results of combined tension and shear with $\beta = 80°$. Specimen configuration before severe delamination propagation of (a) experiment (b) simulation. Delamination failure feature (c) remaining after experiment (d) during simulation. Force-displacement curves of (e) vertical direction (f) horizontal direction. (Solid curve: experiment; Dashed curve: simulation)

5.3.2.3 Uniaxial tension

For the uniaxial tension loading condition, force-displacement curve from simulation correlates well with experiments before severe delamination occurs. A linear elastic range and small range of delamination propagation range are well duplicated. The delamination and subsequent propagation are shown in the simulation as the experiments. The slope of the simulation curve is larger than the compression side as observed in the experiments.
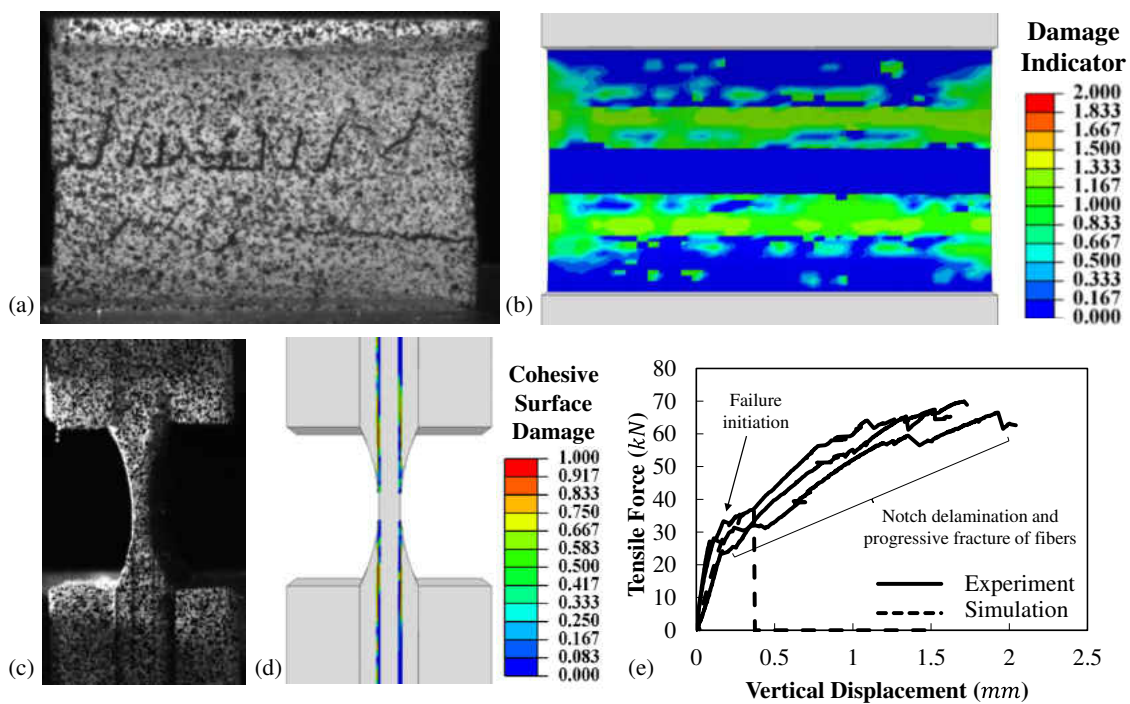
Figure 49: Comparison between numerical simulation and test results of uniaxial tension test. Specimen configuration before severe delamination propagation of (a) experiment (b) simulation. Delamination initiation during (c) experiment (d) simulation. (e) Force-displacement curves of experiments and simulation

To sum up, the multiple parts model with cohesive surfaces behave similar to the single part model before delamination takes place. Delamination and propagation failure feature are well reproduced by cohesive surface method.

CHAPTER 6 METAL MATRIX NANO COMPOSITES

6.1 Theoretical Modeling

6.1.1 Elasticity and plastic hardening

As shown in Section 2, MMNCs have demonstrated asymmetry of elasticity in addition to fracture between tension and compression loading conditions. Similar phenomenon of asymmetric elasticity was reported and studied (Brown et al., 1989; Jarausch et al., 2000; Jones, 1977; Pozdnyakova et al., 2009). Young's modulus has been reported to be dependent on stress state for materials like porous or clastic rocks, golden films and soils (Brown et al., 1989; Cazacu, 1999; Jarausch et al., 2000; Pozdnyakova et al., 2009; Yu & Dakoulas, 1993). Jones (1977) and Hamilton et al. (2006) reported different Young's modulus in compression and tension direction for materials like fiber-reinforced, granular composite and single crystals NiFeGa. Flow stress asymmetry in compression and tension is also reported(J.-Y. Kim, Jang, & Greer, 2012). A model to describe Young's modulus depending on stress states is given by

$$E(\eta) = e_0 + \frac{e_d}{1 + e^{-e_c(\eta+\eta_0)}} . \tag{35}$$

Here, η is the stress triaxiality used to distinguish tensile and compressive loading conditions. e_0 and e_d are parameters determining the upper and lower bound of Young's modulus $E(\eta)$. e_c and η_0 are the parameters used to control the transition from lower to upper bound. Young's modulus's dependency on stress triaxiality are shown in Figure 50, with parameters: $e_0 = 7680 MPa$, $e_c = 54.95$, $e_d = 40000 MPa$ and $\eta_0 = 0.256$ for MMNC 10%; and $e_0 = 19220 MPa$, $e_c = 26.88$, $e_d = 29790 MPa$ and $\eta_0 = 0.256$ for MMNC 15%. A nominal Poisson's ratio $v = 0.3$ is adopted for both materials.

Mg/SiC composites have been reported to have little plasticity when subjected to tensile loading conditions, and as the volume ratio of SiC gets larger, the plastic behavior becomes less apparent(Ferkel & Mordike, 2001; Saravanan & Surappa, 2000). However, for the materials with high volume of SiC reinforcement particles (10% and 15%) in nano size as investigated, apparent plastic behavior was observed under compression tests while no plasticity was exhibited under tensile tests. Due to material composition, particle-reinforced composites have an essence of isotropic in their properties (Manoharan, Lim, & Gupta, 2002). Therefore an isotropic yield function is employed in this study. In addition to the yield condition, associated flow rule (AFR) and isotropic Swift power law hardening function are also used in modeling the plasticity of the MMNCs. The Swift power hardening law reads $\bar{\sigma} = A(\bar{\varepsilon}_{pl} + \varepsilon_0)^n$, where $\bar{\sigma}$ and $\bar{\varepsilon}_{pl}$ are equivalent stress and equivalent plastic strain defined by the von-Mises yield criterion. ε_0 is the correction factor. A and n are determined by the true stress-strain curve obtained from the compression test. Curve fitting results are illustrated in Figure 51 with parameters $A = 2999MPa, n = 0.658$ and $\varepsilon_0 = 0.03$ for MMNC 10%; and $A = 1846.2MPa, n = 0.372$ and $\varepsilon_0 = 0.0267$ for MMNC 15%.
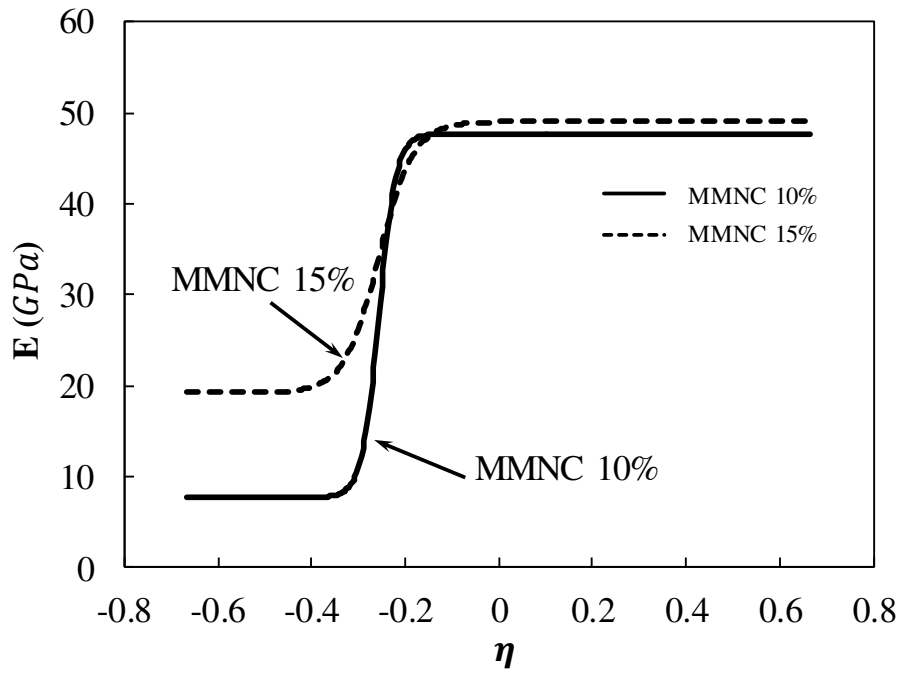
Figure 50: Comparison of Young's modulus (E) versus stress triaxiality (η) between MMNC 10% and MMNC 15% materials

(a) MMNC 10%

(b) MMNC 15%
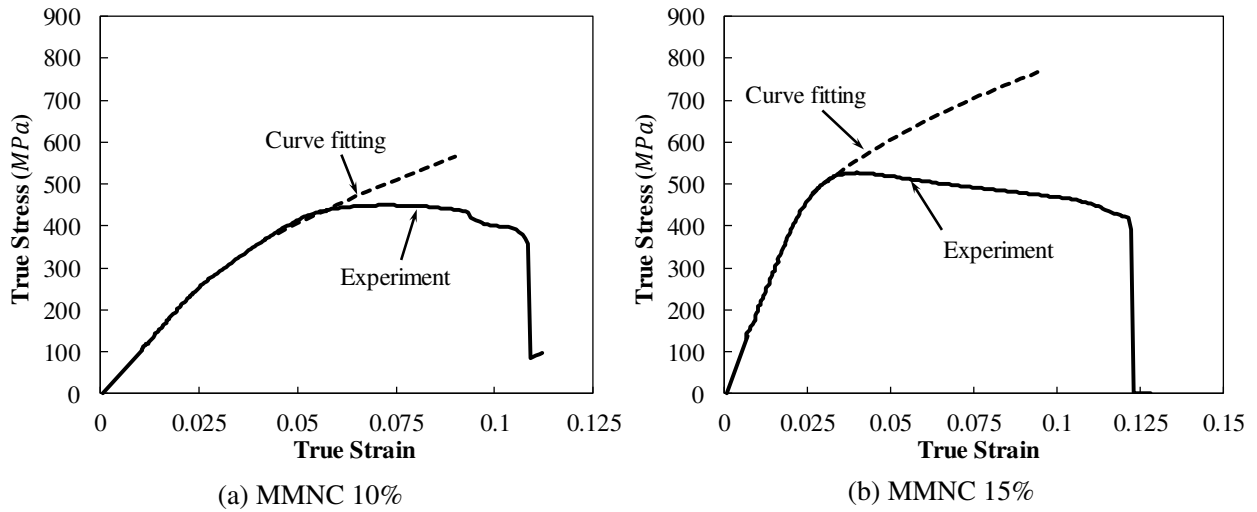
Figure 51: Swift power hardening law fitting for two MMNC materials before softening

6.1.2 Stress based MMC fracture model (sMMC)

Modified Mohr Coulomb (MMC) fracture model was proposed to describe ductile fracture of high strength steels and aluminum alloys (Bai & Wierzbicki, 2008, 2010). The original MMC is based on a mixed space of strain and stress invariant, the fracture locus of which reads

$$\bar{\varepsilon}_f(\eta, \bar{\theta}) = \left\{ \frac{A}{C_2} \left[\tilde{C}_\theta^s + \frac{\sqrt{3}}{2-\sqrt{3}} \left(\tilde{C}_\theta^{ax} - \tilde{C}_\theta^s \right) \left(\sec\left(\frac{\bar{\theta}\pi}{6}\right) - 1 \right) \right] \left[\sqrt{\frac{1+C_1^2}{3}} \cos\left(\frac{\bar{\theta}\pi}{6}\right) + \right. \right. \tag{36}$$

$$\left. \left. C_1 \left(\eta + \frac{1}{3}\sin\left(\frac{\bar{\theta}\pi}{6}\right) \right) \right] \right\}^{-\frac{1}{n}}.$$

Here, A and n are two power hardening coefficients (assuming $\bar{\sigma} = A\bar{\varepsilon}^n$, which was used in the derivation of MMC model. It should be noted that fracture model is uncoupled from plasticity model in the equation of fracture locus). C_1, C_2, $\tilde{C}_\theta^s$ and $\tilde{C}_\theta^{ax}$ are four fracture parameters. η is the stress triaxiality and $\bar{\theta}$ is the Lode angle parameter. The parameter $\tilde{C}_\theta^{ax}$ is defined as

$$\tilde{C}_\theta^{ax} = \begin{cases} 1 & \bar{\theta} \geq 0 \\ \tilde{C}_\theta^c & \bar{\theta} < 0 \end{cases}. \tag{37}$$

Many experimental results and numerical simulations have validated the fracture predicting capability of MMC model for metallic materials (Yaning Li et al., 2010; Y. Li et al., 2011; Luo & Wierzbicki, 2010). However, this model cannot be applied to brittle fracture if there is no plastic deformation before crack. It has to be transferred back to the stress space of Mohr-Coulomb model. By applying $\bar{\varepsilon}_f(\eta, \bar{\theta})$ into $\bar{\sigma} = A\bar{\varepsilon}^n$, the derived stress based MMC model (referred as sMMC hereafter) is shown as follows.

$$\hat{\sigma}_f(\eta, \bar{\theta}) = C_2 \left\{ \left[\tilde{C}_\theta^s + \frac{\sqrt{3}}{2 - \sqrt{3}} (\tilde{C}_\theta^{ax} - \tilde{C}_\theta^s) \left(\sec\left(\frac{\bar{\theta}\pi}{6}\right) - 1 \right) \right] \left[\sqrt{\frac{1 + C_1^2}{3}} \cos\left(\frac{\bar{\theta}\pi}{6}\right) \right. \right.$$

$$\left. \left. + C_1 \left(\eta + \frac{1}{3} \sin\left(\frac{\bar{\theta}\pi}{6}\right) \right) \right] \right\}^{-1} \tag{38}$$

The calibrated 3D fracture loci of material MMNC 10% and MMNC 15% are plotted in Figure 52. In addition, two more features are added to sMMC model while applying in FE simulation. One is the lower limit of fracture stress σ_{cutoff} just in case of it comes up with a nonrealsitic small number at the high stress triaxiality range. The other feature is the cutoff value of stress triaxiality at low stress triaxiality region (taking $\eta < -0.35$). Since all three tests were failed under plane stress loading condition, the fracture locus can be presented in a 2D space of stress triaxiality (η) and equivalent stress to fracture ($\hat{\sigma}_f$). A relationship between η and $\bar{\theta}$ under plane stress condition is known as follows (Bai & Wierzbicki, 2008).

$$\cos\left[\frac{\pi}{2}(1 - \bar{\theta})\right] = -\frac{2}{27}\eta\left(\eta^2 - \frac{1}{3}\right) \tag{39}$$

By substituting Eq. (39) into Eq. (38), the 2D plane stress sMMC fracture locus is obtained in the following form:

$$\hat{\sigma}_f(\eta, \bar{\theta}) = C_2 \left\{ f_3 \left[\sqrt{\frac{1 + C_1^2}{3}} f_1 + C_1 \left(\eta + \frac{f_2}{3} \right) \right] \right\}^{-1}, \tag{40}$$

where

$$f_1 = \cos\left\{\frac{1}{3}\arcsin\left(-\frac{27}{2}\eta\left(\eta^2 - \frac{1}{3}\right)\right)\right\} \tag{41}$$

$$f_2 = \sin\left\{\frac{1}{3}\arcsin\left(-\frac{27}{2}\eta\left(\eta^2 - \frac{1}{3}\right)\right)\right\} \tag{42}$$

$$f_3 = \tilde{C}_\theta^s + \frac{\sqrt{3}}{2-\sqrt{3}}\left(\tilde{C}_\theta^{ax} - \tilde{C}_\theta^s\right)\left(\frac{1}{f_1} - 1\right). \tag{43}$$

Hence, the $\hat{\sigma}_f(\eta, \bar{\theta})$ depends only on η under plane stress condition, becoming $\hat{\sigma}_f(\eta)$. It is indicated as magenta solid curves in Figure 52. $\hat{\sigma}_f(\eta)$ is also demonstrated for 2D plane stress condition in Figure 53 for a better comparison.
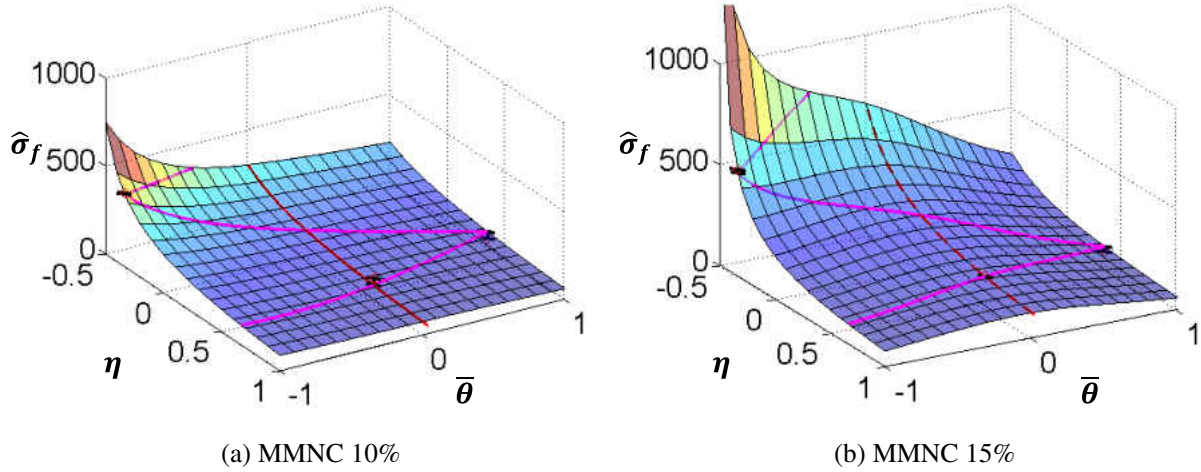
(a) MMNC 10%   (b) MMNC 15%

Figure 52: 3D fracture loci of two materials (a) MMNC 10% and (b) MMNC 15% in the space of equivalent stress to fracture($\hat{\sigma}_f$), stress triaxiality (η) and Lode angle parameter ($\bar{\theta}$). Experimental points are marked.
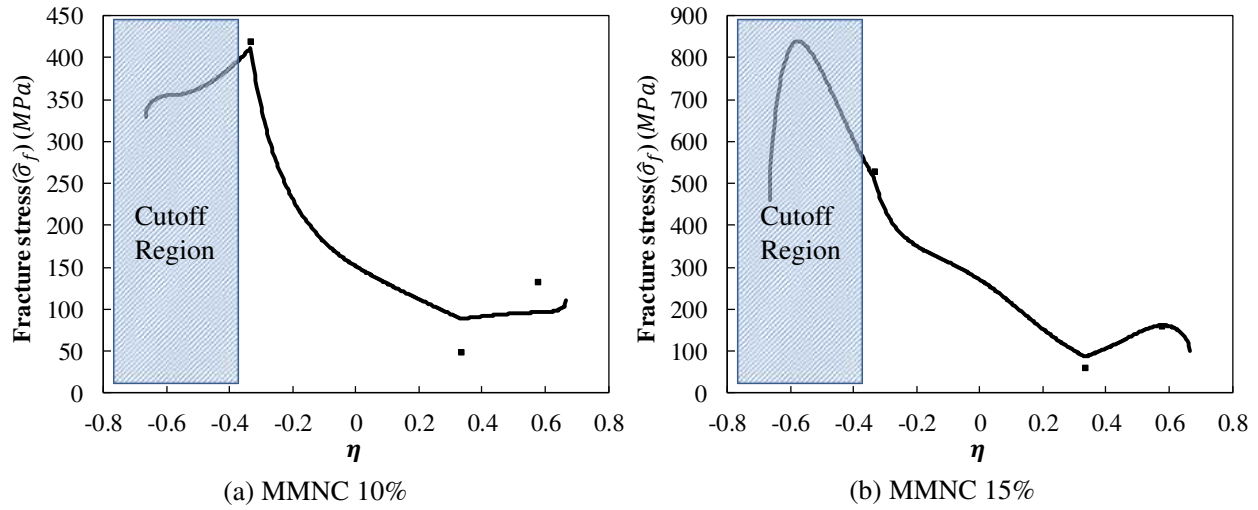
Figure 53: Calibration of sMMC fracture model for (a) Mg/SiC nano composites with 10% volume fraction of SiC ($C_1 = 0.703, C_2 = 85.12, \tilde{C}_\theta^s = 0.7984 \ and \ \tilde{C}_\theta^c = 0.796$), (b)Mg/SiC nano composites with 15% volume fraction of SiC ($C_1 = 0.92179, C_2 = 98.44, \tilde{C}_\theta^s = 0.4636 \ and \ \tilde{C}_\theta^c = 0.8816$)

Three equivalent stresses to fracture from three different tests were used to calibrate this model. The calibrated fracture loci are shown in Figure 52 and Figure 53. Good correlations are obtained for both materials. It is found that the experimental result for uniaxial tension ($\eta = \frac{1}{3}$) is lower than model prediction because there were surface defects on the sample which are not included in calibration and simulations. As for the three-point bending condition ($\eta = \frac{1}{\sqrt{3}} = 0.577$), the experimental results were calculated from flexural stress equation (assuming the same Young's modulus between tension and compression for simplicity). The final modeled curves were obtained from iteration of comparison between simulations and experiments. The modeling procedure will be explained in details in Section 4.

6.1.3 Damage accumulation and material post-failure softening

When equivalent stress is less than corresponding fracture stress, a linear relationship is assumed between damage indicator (D) and the equivalent stress $\bar{\sigma}$. Therefore the material damage evolution is defined as follows.

$$D = \frac{\bar{\sigma}}{\hat{\sigma}_f(\eta,\bar{\theta})}, \tag{44}$$

where $\bar{\sigma}$ is von-Mises equivalent stress and $\hat{\sigma}_f(\eta,\bar{\theta})$ is the sMMC fracture locus. When damage indicator $D < 1$, the material is either elastic or elastic-plastic without failure. When $D = 1$, it indicates that failure initiates as equivalent stress reaches a critical value from the sMMC model. Typically, the material exhibits elastic-plastic behaviors from beginning to failure initiates ($0 \leq D \leq 1$). However, sometimes failure initiation could occur before material yielding and therefore material plastic hardening could vanish under some loading conditions like uniaxial tension for this material.

After failure initiation, the damage indicator is defined by an incremental form:

$$dD = \frac{L\tilde{\sigma}d\bar{\varepsilon}_{pl}}{G_c}, \tag{45}$$

where L is the characteristic length of a finite element in FE simulation, $\tilde{\sigma}$ is equivalent stress that incorporates the effect of material post-failure softening, which is different from the equivalent stress $(\bar{\sigma})$ from the hardening model. $d\bar{\varepsilon}_{pl}$ is the incremental plastic strain. G_c is the toughness or critical strain energy release rate at fracture. $\tilde{\sigma}d\bar{\varepsilon}_{pl}$ is the strain energy incremental per unit volume, and $L\tilde{\sigma}d\bar{\varepsilon}_{pl}$ represents strain energy incremental per unit surface.

Material softening starts after the failure initiation ($D \geq 1$). This is an important aspect which affects the prediction of failure stress, failure strain and failure modes. A material post-failure softening model is postulated in the following expression,

$$\tilde{\sigma} = \hat{\sigma}_f(\eta, \bar{\theta})[1 - S_s(D - 1)^{S_m}], \tag{46}$$

where $\hat{\sigma}_f(\eta, \bar{\theta})$ is the failure stress dependent on loading conditions, given by the sMMC model. It is also the upper limit of stress after failure initiation. S_s is a parameter to determine the ultimate failure stress, and S_m is a parameter to determine stress decreasing rate with respect to damage indicator D. The material post-failure softening coefficient $[1 - S_s(D - 1)^{S_m}]$ at the range of $1 \leq D \leq 2$ is demonstrated in Figure 54.

When the strain energy accumulation reaches $L \int \tilde{\sigma} d\bar{\varepsilon} = G_c$, the damage indicator reaches $D = 2$. Then, a material point is defined as ultimate failure and the corresponding finite element will be deleted.

As stated earlier, Mg/SiC material shows brittle failure in tensile loading conditions and ductile failure in compressive loading conditions. This feature is characterized by applying a stress triaxiality dependent toughness $G_c(\eta)$, which is defined by

$$G_c(\eta) = g_{\circ} e^{-(\eta - g_1)g_2}, \tag{47}$$

where g_0, g_1 and g_2 are parameters for describing the brittle-ductile fracture transition. Parameters were obtained to calibrate this failure feature individually for each material and the results are shown in Figure 55. For a larger value of G_c, a material needs to accumulate more strain energy before ultimate failure. Since there is no test data available at the region of $\eta < -0.4$, G_c is assumed as constant under those loading conditions. In this way, materials need more

energy to break when it undergoes compressive loading conditions ($\eta < 0$) than tensile loading conditions ($\eta > 0$), which corresponds to the features of ductile compression failure and brittle tension failure.
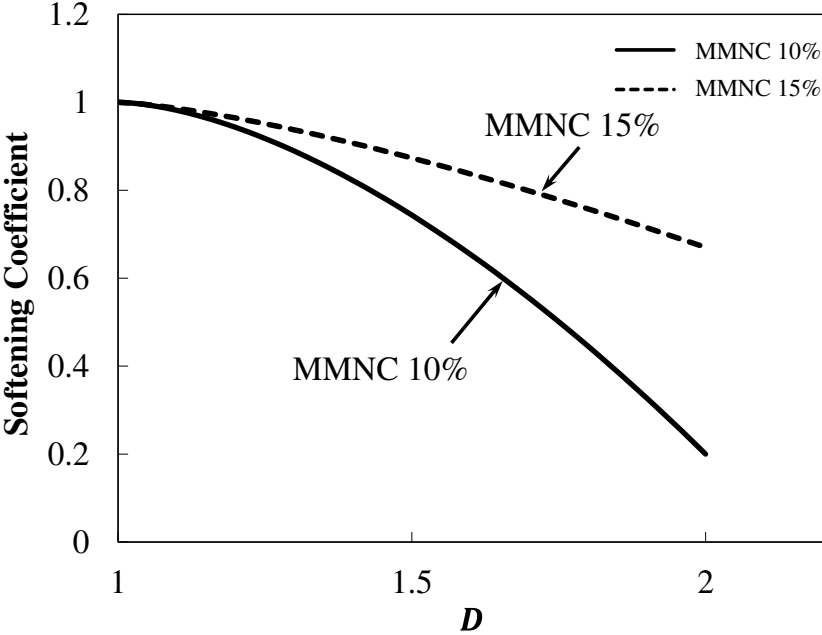
Figure 54: Comparison of material softening evolution curves between MMNC 10% and MMNC 15% materials
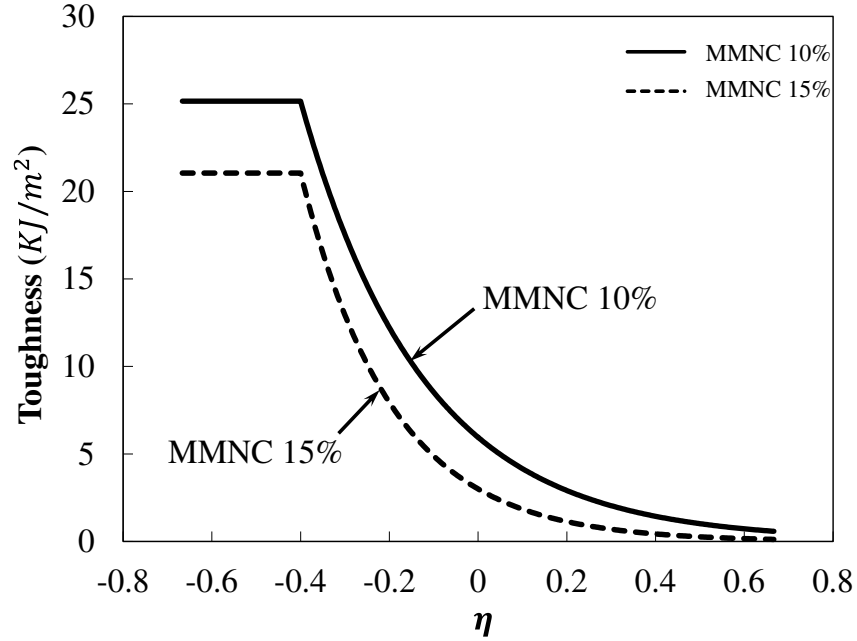
Figure 55: Comparison of toughness versus stress triaxiality (η) curves between MMNC 10% and MMNC 15% materials

To sum up, the damage indicator follows the following equation,

$$D = \begin{cases} \dfrac{\bar{\sigma}}{\hat{\sigma}_f(\eta,\bar{\theta})} & ,0 \leq D \leq 1 \\[4mm] 1 + \dfrac{L \int \tilde{\sigma} d\bar{\varepsilon}}{G_c(\eta)} & ,1 < D \leq 2 \end{cases} . \tag{48}$$

With all the modeling methods mentioned above, a sketch is provided in Figure 56 to show the overall stress-strain curves of two typical loading conditions: uniaxial compression and uniaxial tension. At the beginning the material presents elasticity under both loading conditions. Under compressive loading conditions plastic hardening follows afterwards till the stress reaches sMMC fracture stress $\hat{\sigma}_f(\eta,\bar{\theta})$ where failure initiates. Then, material post-failure softening takes place and equivalent stress $\bar{\sigma}$ becomes $\tilde{\sigma}$. The ultimate failure of material occurs when $D = 2$, which means the strain energy stored in the material reaches a critical value G_c. Shadowed area

99

indicates the strain energy accumulation along deformation. On the other hand, material presents only elasticity under tensile loadings, before reaching sMMC fracture stress $\hat{\sigma}_f(\eta, \bar{\theta})$. At this point the equivalent stress $(\bar{\sigma})$ becomes $\tilde{\sigma}$ as well, and the ultimate failure occurs much earlier than compression since G_c is much smaller in this case. Here the shadowed area shows a schematic for the plastic strain energy from fracture initiation to total crack. Due to deformation localization, a testing machine usually cannot detect this small area of deformation and a sharp force drop is observed.
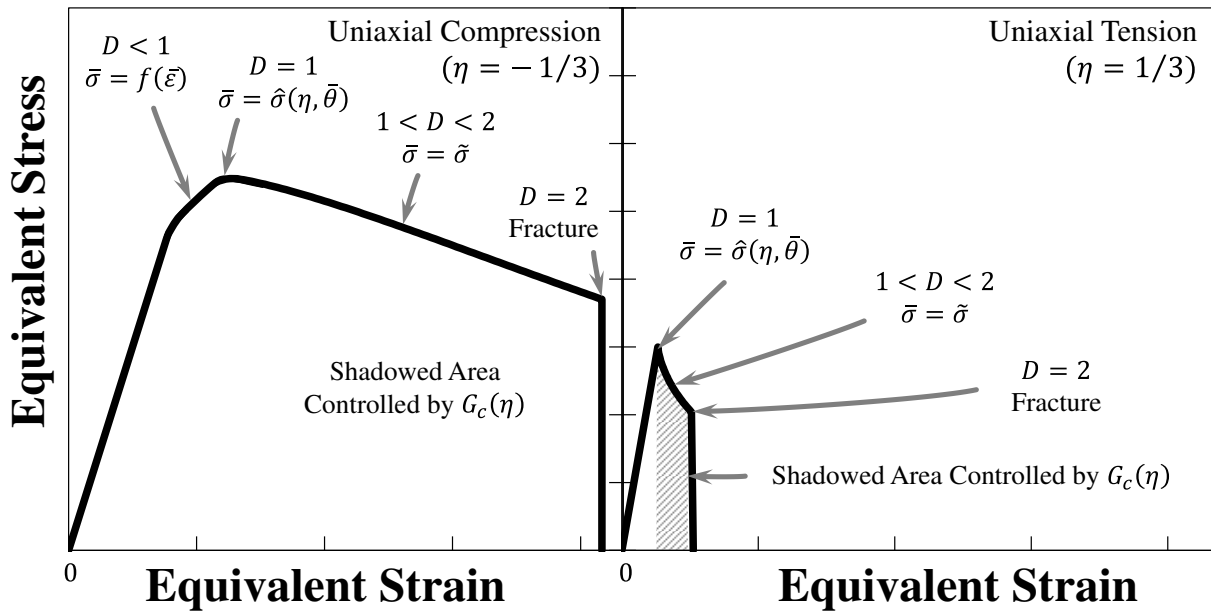
Figure 56: A sketch of equivalent stress-strain curves for uniaxial compression and uniaxial tension conditions

6.2 Model calibration procedure

Finite element simulations for three loading conditions were performed using ABAQUS/Explicit. The proposed material model was implemented as a material subroutine (VUMAT). The phenomena of crack initiation and propagation were simulated using an element deletion

technique. The finite element meshes are shown in Figure 57. Specimens were modeled using C3D8R solid elements with a typical element size of $0.25mm \times 0.25mm \times 0.25mm$. The experimental apparatus, including grips of tensile testing, the support and crosshead pins of three-point bending, and compression platens, were modeled as rigid bodies.

| (a) Three point bending | (b) Uniaxial Compression |
| (c) Uniaxial Tension | (d) Dogbone specimen |
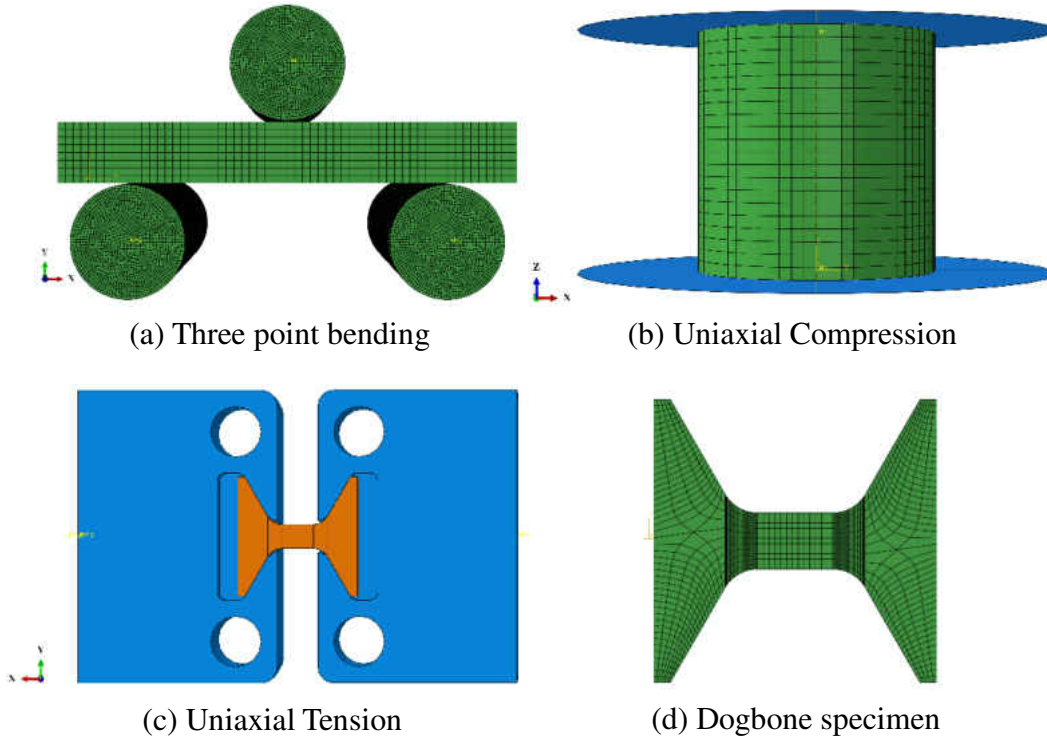
Figure 57: Finite element meshes for Mg/SiC specimens. (a) Three-point bending, (b) Uniaxial compression, (c) Half assembled uniaxial tension model, (d) Dogbone specimen for uniaxial tension.

The model calibration procedures were similar for both MMNC 10% and MMNC 15% materials, which are summarized as follows.

1. The first step was to calibrate the elasticity model. Tested Young's moduli under both uniaxial tension and compression were correlated with the model ones by adjusting the parameter e_0 and e_d. Iterations would be required to fit the measured slope in the elastic range of the force-displacement curve under three-point bending condition, in order to calibrate the transition area between tension and compression loading conditions (represented by parameter e_c and η_0).

2. Secondly, the hardening model was fitted using tested stress-strain data under uniaxial compression. The selection of data was based on the occurrence of plastic behavior under this loading condition. The curve fitting was performed up to the maximum true stress.
3. Thirdly, the sMMC fracture model was calibrated using the maximum strength under three different stress states. It is worth mentioning that data point of bending ($\eta = 0.577$) is a nominal number because of the elasticity asymmetry between tension and compression, which may shift the neutral axis of a beam. In this case, the locus of sMMC model at that point should be determined iteratively with simulations.
4. Finally, the toughness function was calibrated based on the tested stress-strain (or force-displacement) areas under three different loading conditions. This was to assure the correlation of the ultimate fracture strains. The softening function was calibrated by using the tested stress-strain under uniaxial compression to achieve the correct failure mode.

Material post-failure softening is essential to simulate slant shear failure modes, especially for the material of MMNC 10%. Slant fracture is attributed to the shear band localization after post-failure softening. This can be achieved by applying a faster material softening characterization with setting a larger difference in toughness between uniaxial compression ($\eta = -1/3$) and pure shear condition ($\eta = 0$). With slant fracture feature shown in compression loading condition, the same material post-failure softening was used in other two conditions. Several iterations of step 3 and 4 were attempted with performing finite element simulations, in order to well correlate all tested force-displacement curves. Two sets of fully calibrated model parameters for these two materials are presented in

Table 6. A flow chart of the above calibration process is shown in Figure 58 .
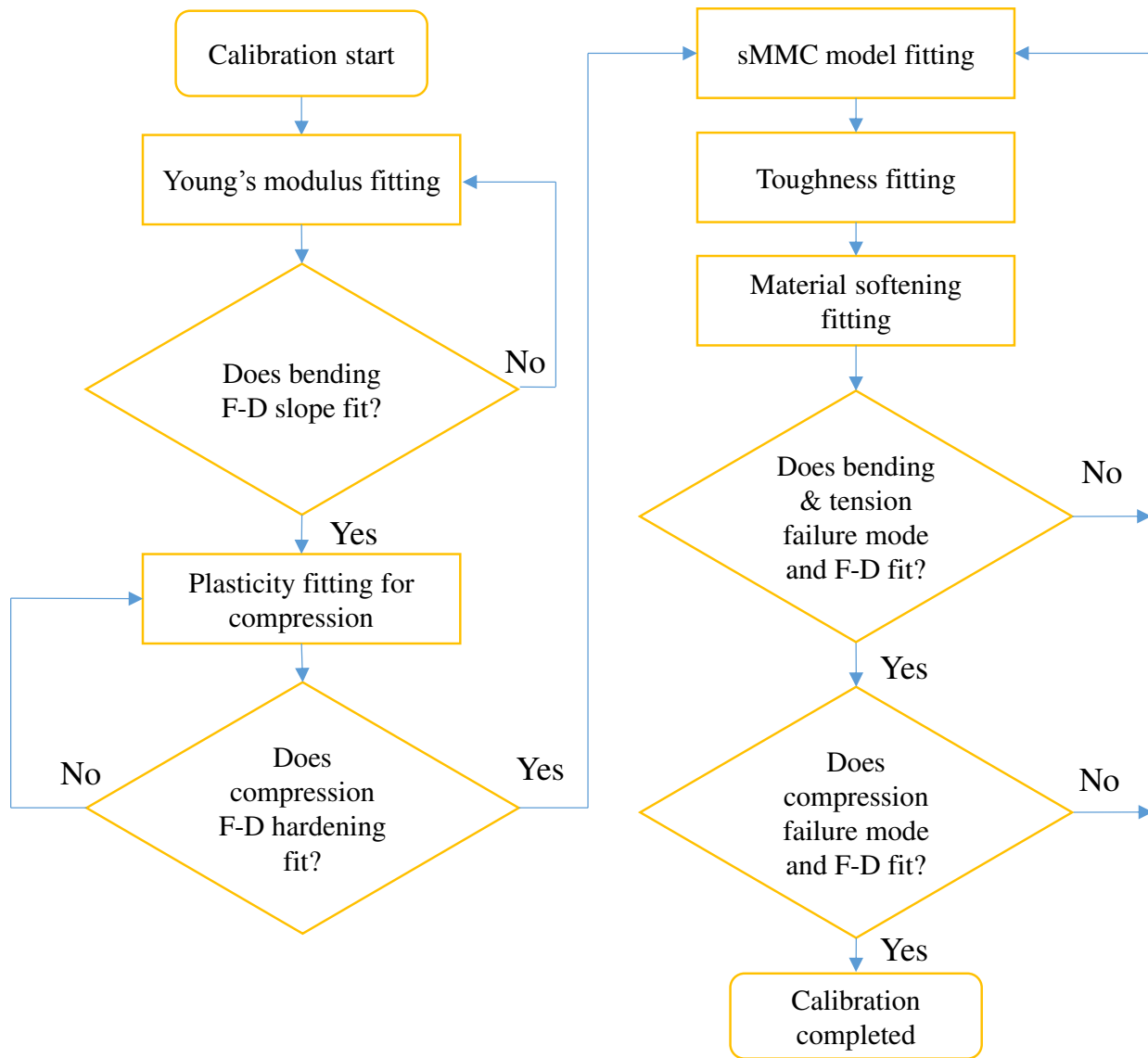
Figure 58: Flow chart of model calibration procedure. F-D stands for force-displacement curve.

Table 6: Input parameters for numerical simulations

	$e_0(MPa)$	e_c	$e_d(MPa)$	η_0	ν	$A(MPa)$	n
MMNC 10%	7680	54.95	40000	0.256	0.3	2999	0.658
MMNC 15%	19220	26.88	29790	0.256	0.3	1846.2	0.372
	ε_0	C_1	C_2	$\tilde{C}_\theta^s$	$\tilde{C}_\theta^c$	S_s	S_m
MMNC 10%	0.03	0.703	85.12	0.7984	0.796	0.8	1.69
MMNC 15%	0.0267	0.92179	98.44	0.4636	0.8816	0.33	1.38
	g_0	g_1	g_2	η_{cutoff}	σ_{cutoff}		
MMNC 10%	5.9	0.05	3.62	-0.35	45		
MMNC 15%	3	0	4.87	-0.35	75		

6.3 Simulation results

The FE simulation results of these two MMNCs are presented and analyzed in the following subsections. All three types of loading conditions are included.

6.3.1 MMNC 15% simulation results

6.3.1.1 Three-point Bending

Figure 59 shows the photo of the bending test of material MMNC 15% as well as the FE simulation results. A brittle fracture is observed in both experiment and simulation. Crack initiation location and propagation were well captured by the FE simulation. In the simulation, cracks (deleted elements) initiated from the bottom and propagated to the top surface. The predicted force-displacement curve in simulation well duplicated the experimental one in terms of both slope and ultimate fracture limit.

Figure 59: Comparison between numerical simulation and test results of the three-point bending test for Mg/SiC nano composites with 15% volume fraction of SiC

6.3.1.2 Compression

Figure 60 shows the photo of an upsetting test of material MMNC 15% as well as the simulation results. The specimen broke into random pieces after ultimate fracture. The fracture pattern was well captured in the FE simulation. Force-displacement curve of simulation accurately duplicated the experimental one in terms of slope, ultimate fracture limit, strain hardening, post-failure softening and corresponding displacement to fracture.

Figure 60: Comparison between numerical simulation and test results of an upsetting test for Mg/SiC nano composites with 15% volume fraction of SiC

6.3.1.3 Uniaxial Tension

Figure 61 shows the comparison between experiment and simulation for uniaxial tension using a dogbone speciemn. One can see that similar fracture features were well captured by the FE simulation. The crack location of experiment was at the shoulder of the specimen, rather than in the middle. This was probably due to the friction from the grip and possible defects on the specimen surface. Since there was no surface defect assumed in the simulation model, the simulation strength was higher than experiment. This is consistent with calibration of fracture locus (Figure 53). Further details will be provided in the discussion section. The Young's modulus of simulation fitted well with experiment in the tensile condition.

Figure 61: Comparison between numerical simulation and test results of uniaxial tensile tests for Mg/SiC nano composites with 15% volume fraction of SiC

6.3.2 MMNC 10% simulation results

6.3.2.1 Three-point Bending

Figure 62 shows the FE simulation result of material MMNC 10%. Fracture modes are the same as the material MMNC 15%. Brittle fracture initiated from the bottom and propagated to the top surface. Fracture limit was well simulated and the Young's modulus was close to the value from experiment.
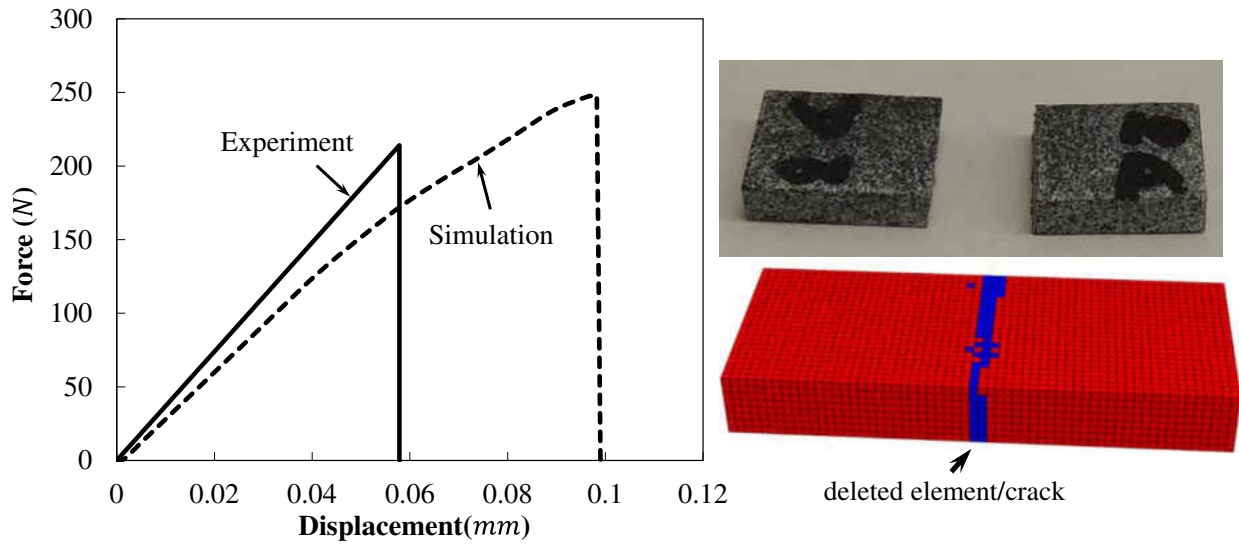
Figure 62: Comparison between numerical simulation and test results of three-point bending tests for Mg/SiC nano composites with 10% volume fraction of SiC

6.3.2.2 Compression

Shear dominated ductile fracture was observed in this upsetting test. This phenomenon was also well captured by the FE simulation (see Figure 63). Slant failure surface emerged after large deformation has been applied to the specimen. Since there was friction effect on both the top and bottom surfaces (or called the barreling effect in upsetting tests), a complex combination of tensile and compressive force components will exist on the contact boundaries. This brought additional difficulty since the material shows brittle fracture and low strength in tensile conditions. Through iterations in FE simulations, appropriate parameters for tensile condition strength and toughness were found to fit all three loading conditions. In addition, the slant fracture surface indicated a shear failure mode after shear band localization, which required a low fracture stress around shear loading condition ($\eta = 0$). Finally, a good fit of stress-strain curve was obtained.

108
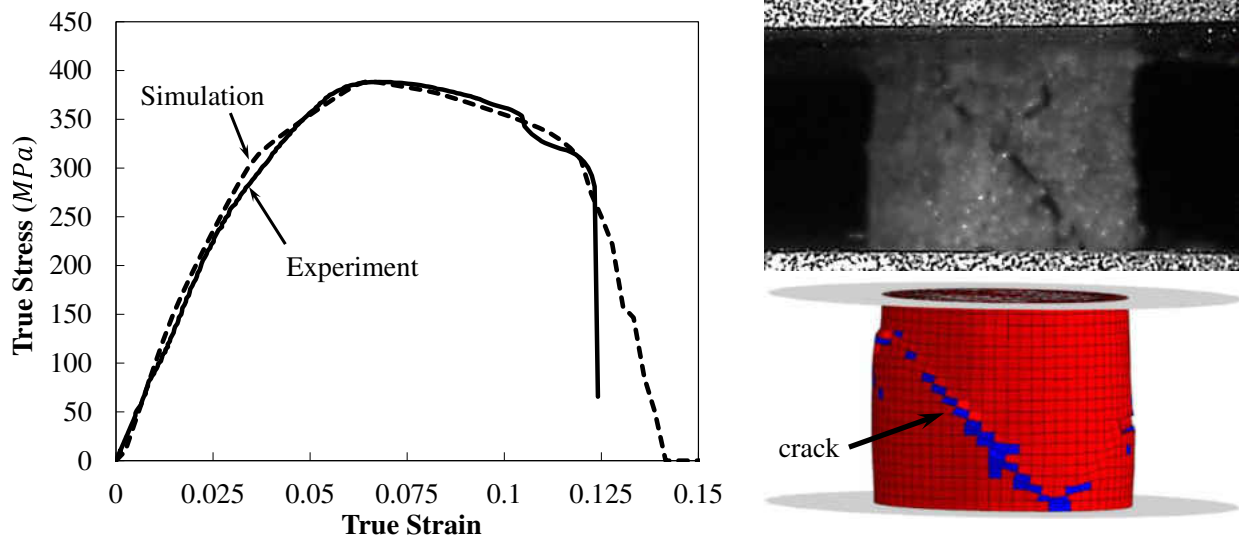
Figure 63: Comparison between numerical simulation and test results of upsetting tests for Mg/SiC nano composites with 10% volume fraction of SiC

6.3.2.3 Uniaxial Tension

The tension simulation is pretty similar to the one of MMNC 15% material. The results are illustrated in Figure 64. The Young's modulus was set exactly the same as experiment, but the displacement to fracture was over predicted. The possible reason of the higher failure strength and larger failure strain compared to experiment was that there were manufacture defects on surfaces of the tension specimen. Only one tensile test was conducted for this material. Also, the same softening coefficient for compression simulation was used for tensile case which may not be sufficient. Further details will be provided in the discussion section.
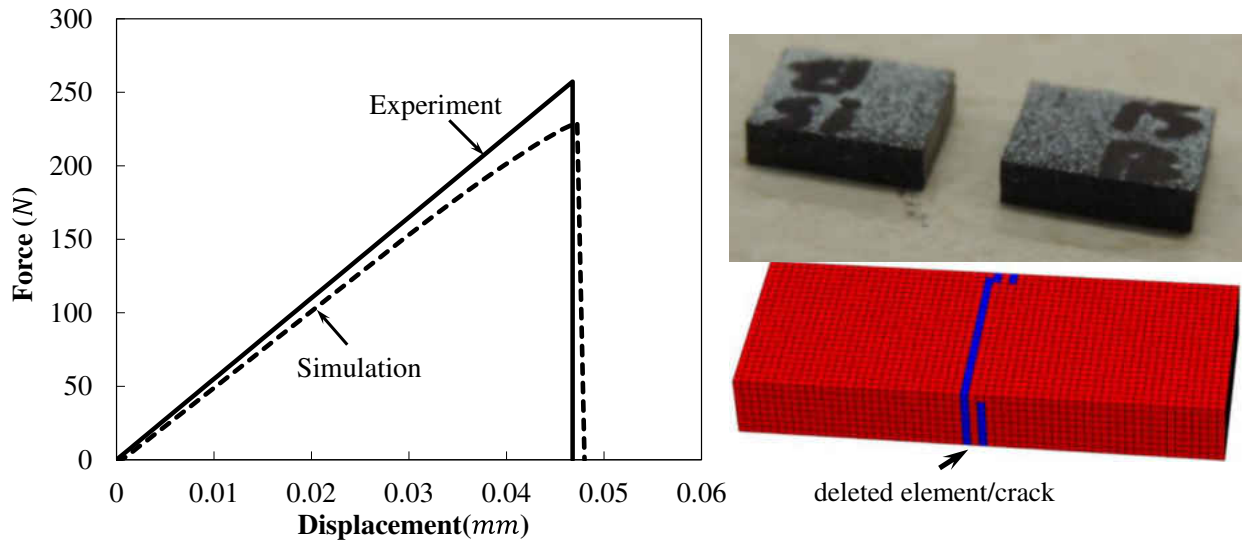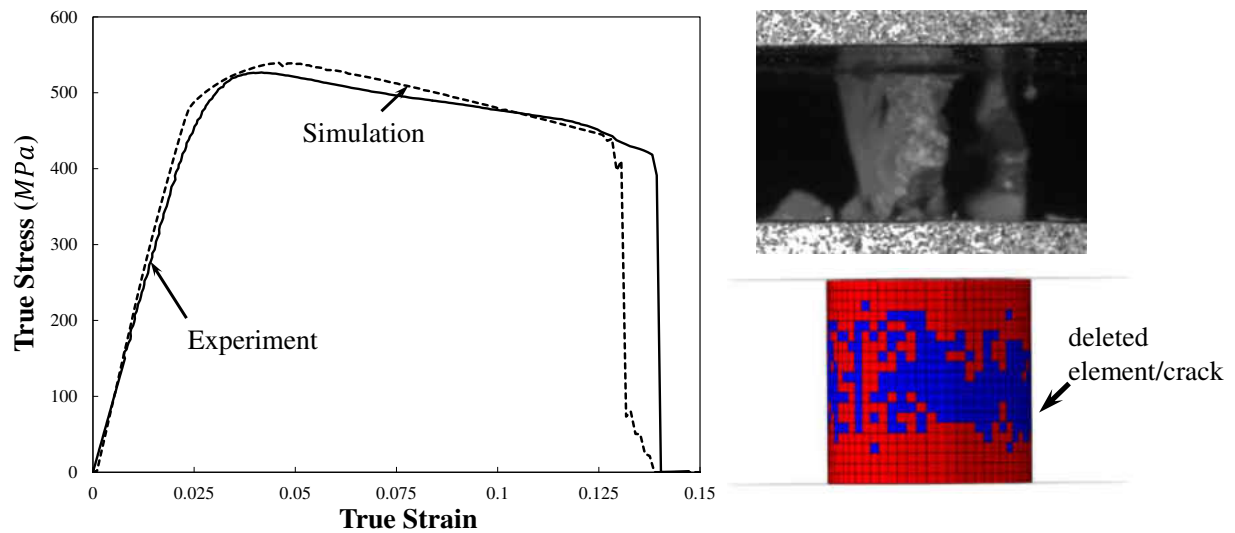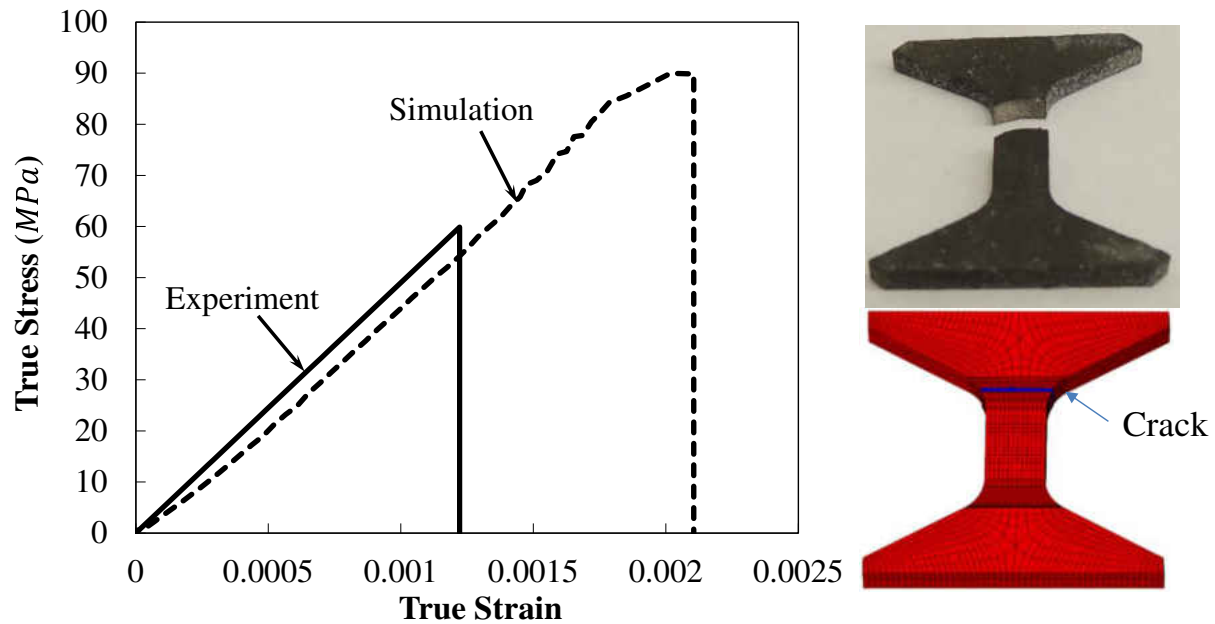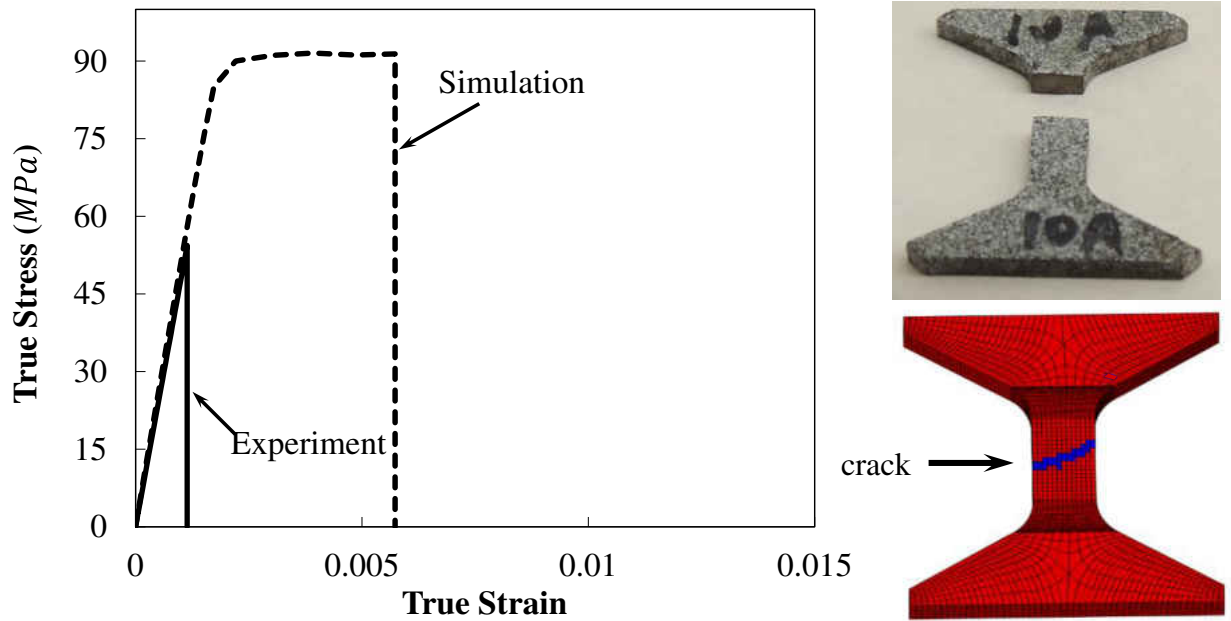
Figure 64: Comparison between numerical simulation and test results of uniaxial tensile tests for Mg/SiC nano composites with 10% volume fraction of SiC

CHAPTER 7 VALIDATION OF PROPOSED MODEL ON PMCS LAMINATES

7.1 Single Stringer Compression Specimen

The single stringer compression specimen experiment data are obtained from the reference (Bisagni, Vescovini, & Dávila, 2011). A brief introduction to the experimental setup will be included here and further details can be found from the reference.

Aeronautical panels are stiffened with stringers in the axial direction and the configuration of the stringer influence the buckling and post-buckling behavior. A single stringer compression is a repeating unit that can represent the whole structure. The single-stringer compression specimen is shown in Figure 65. The specimen is comprised of a skin and stringer. The skin consists of an 8-ply quasi-isotropic laminate with a stacking sequence of $[45°/90°/-45°/0°]s$. The total thickness of the skin is 1 mm. The stringer consists of a 7-ply laminate with a symmetric stacking sequence of $[-45°/0°/45°/0°/45°/0°/-45°]$. The total thickness of stringer is 0.875 mm. Both the skin and the stringer are made from IM7/8552 graphite-epoxy material which are the same as the unidirectional carbon fiber composites investigated in Chapter two and Chapter five. Totally six specimens are manufactured and tested. In three of the specimens, a Teflon insert was introduced between skin and stringer to assess the effect of initial defects on the residual strength. The two ends of the specimen were encased in potting with a mixture of epoxy resin and aluminum powder. Axial compression loadings are applied to the ends of the specimen where tabs are attached.
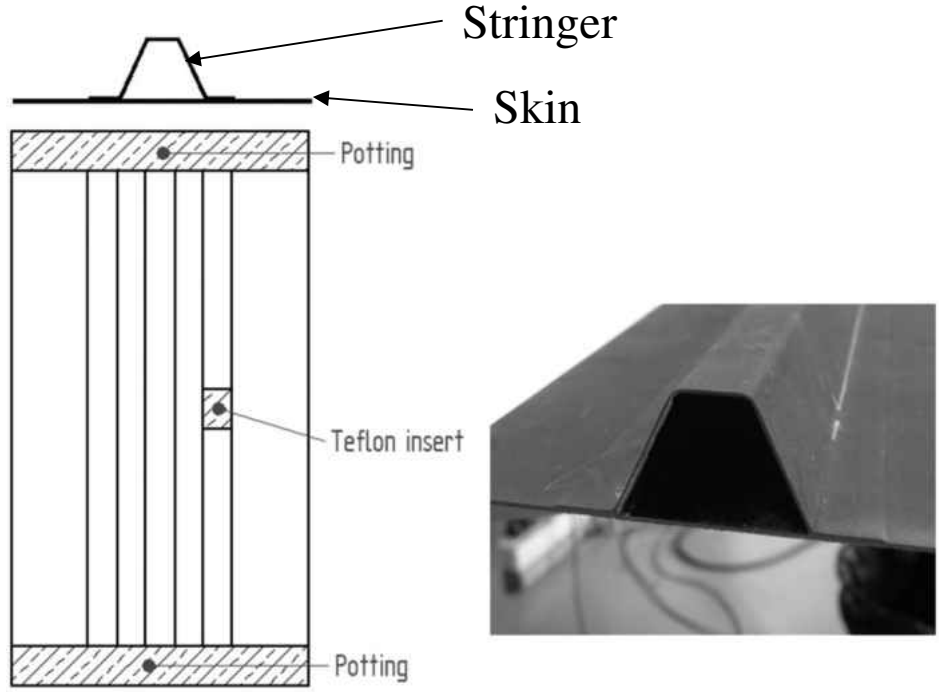
Figure 65: An illustration of a single-stringer compression specimen (left) and a figure of hat stiffener end (right) (reprint from (Bisagni et al., 2011))

7.2 Model setup

The loading condition on the single stringer is a compression loading. The skin and stringer are modeled as separate part and stick together using the cohesive element in between. If there is Teflon insert in the specimen, this Teflon part will be modelled with very weak strength in the cohesive element. The cohesive element part is shown here for better illustration. The cross-section is shown to better reveal the model configuration. The skin and stringer are modeled using the proposed model discussed in Chapter 5.
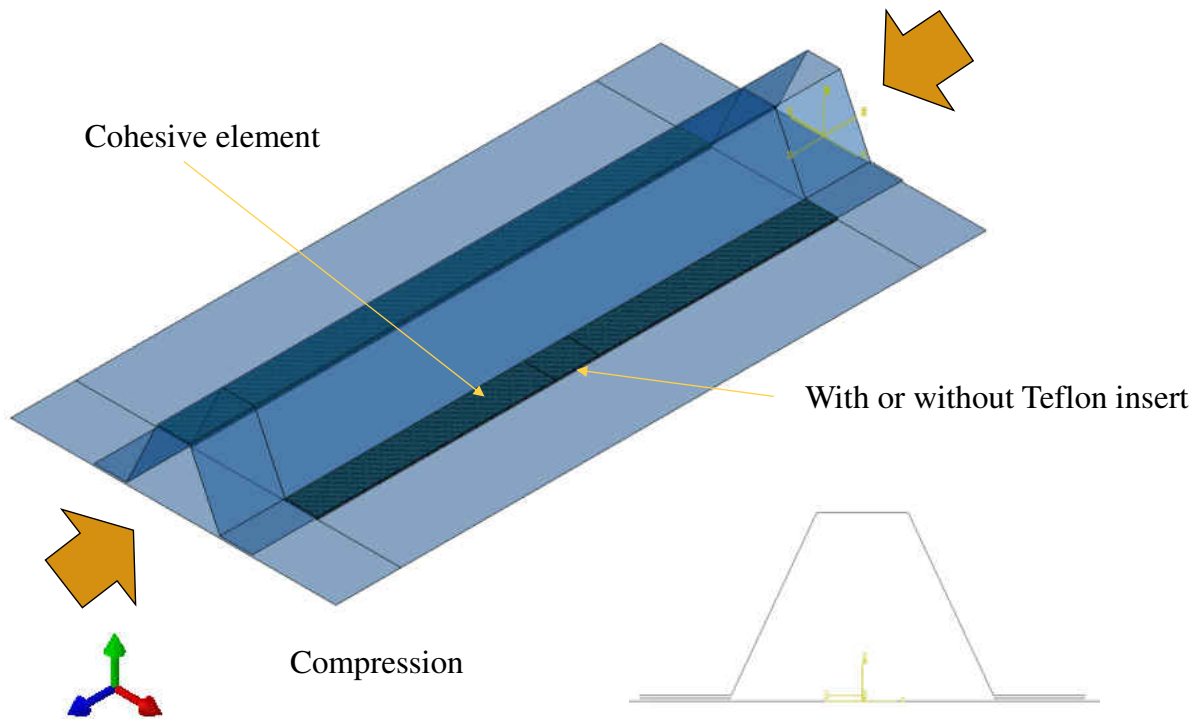
Figure 66: An illustration and a cross-section of a single stringer compression specimen

7.3 Cohesive element method

Similar to the unidirectional carbon fiber composites, a cohesive element method is applied to the laminates other than the cohesive surface method for the interface. A linear elastic traction-separation behavior is applied. The stress of cohesive element is related to the relative displacement between interface. ε are nominal strain which are defined as the corresponding separations δ divided by the original thickness of the cohesive element. The default value of the original constitutive thickness is 1.0 if traction-separation response is specified, which ensures that the nominal strain is equal to the separation. While the stress reaches the critical stress, damage initiates. The damage evolution follows after the initiation and total failure happens when reaching critical displacement. The left figure show the cohesive element location. The right figure shows the double linear behavior of the cohesive element.

$$t = \begin{Bmatrix} t_n \\ t_s \\ t_t \end{Bmatrix} = \begin{bmatrix} E_{nn} & E_{ns} & E_{nt} \\ E_{ns} & E_{ss} & E_{st} \\ E_{nt} & E_{st} & E_{tt} \end{bmatrix} \begin{Bmatrix} \varepsilon_n \\ \varepsilon_s \\ \varepsilon_t \end{Bmatrix} = E\varepsilon, \tag{49}$$

where nominal strain $\varepsilon_n = \frac{\delta_n}{T_0}, \varepsilon_s = \frac{\delta_s}{T_0}, \varepsilon_t = \frac{\delta_t}{T_0}$.

7.4 Simulation results

Buckling is shown in different levels of loads on specimen with Teflon insert (Figure 67). In the figure, the structural response of the specimen under 15 kN and 35 kN loads are shown in both experiments and simulations. Under 15 kN, both the experiments and the simulations shows slight buckling with small curvature while under 35 kN, both of experiments and simulations shows severe buckling with large curvature.
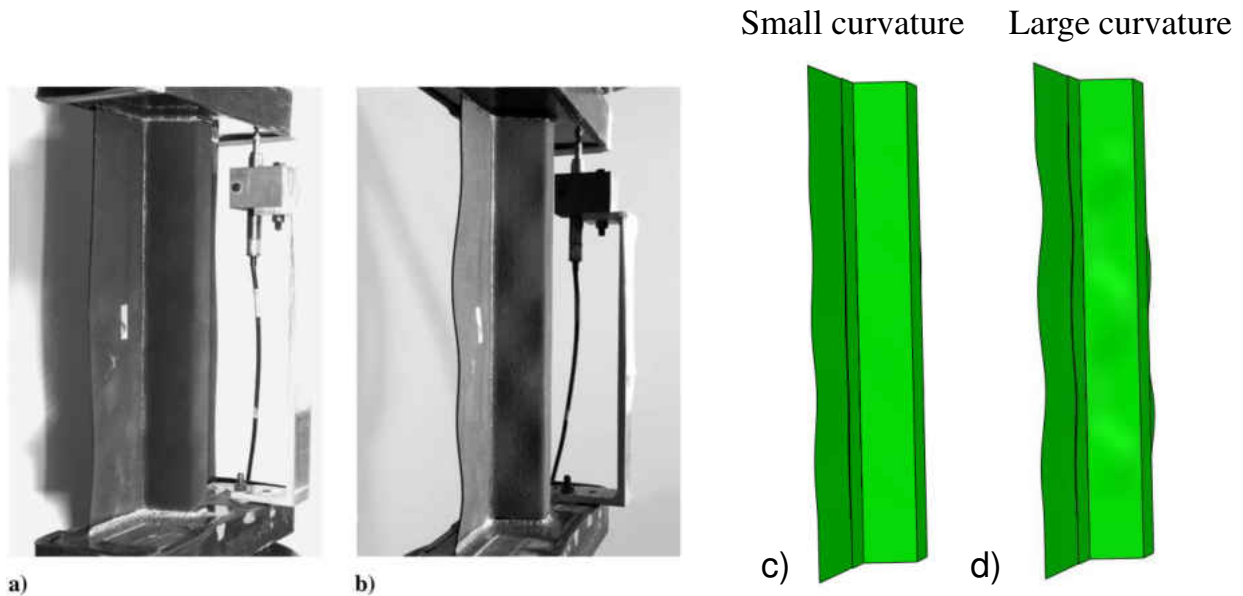
Figure 67: Structural response of a single-stringer specimen with Teflon insert at two load levels: from experiments a) 15 kN b) 35 kN and from simulation c) 15 kN d) 35 kN (experimental figure (a) and (b) reprint from (Bisagni et al., 2011))

Figure 68 shows the failure modes of the initially pristine specimen and specimen with Teflon insert. Skin/stringer separations are shown in both of the specimens. And the simulation well reproduce this phenomenon. Also, for the specimen with Teflon insert, the stringer crippled at 0° which are shown in the simulation. However, in the initially pristine specimen, the stringer crippled at 45° which is not shown in simulation. However, the crippling at 45° is not necessary for all the cases. The crippling at 0° of initially pristine specimen is shown in Figure 69.
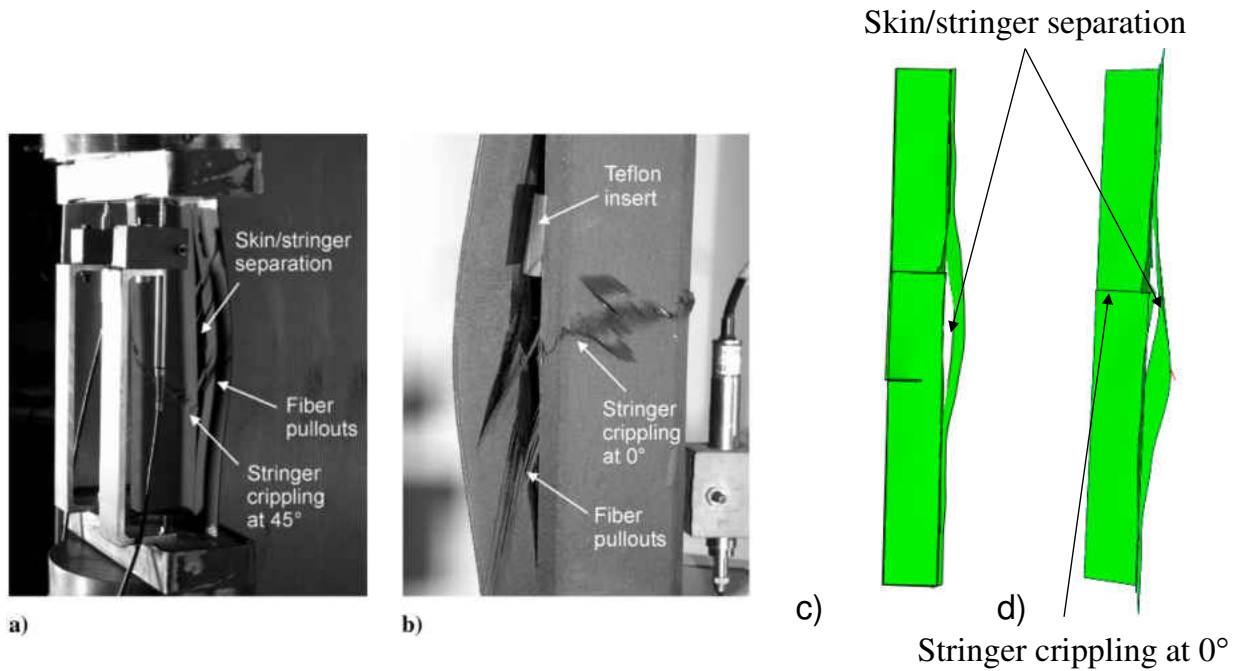
Figure 68: Failure modes in different panels: of experiment a) initially pristine specimen; b) specimen with Teflon insert and of simulation c) initially pristine specimen; d) specimen with Teflon insert
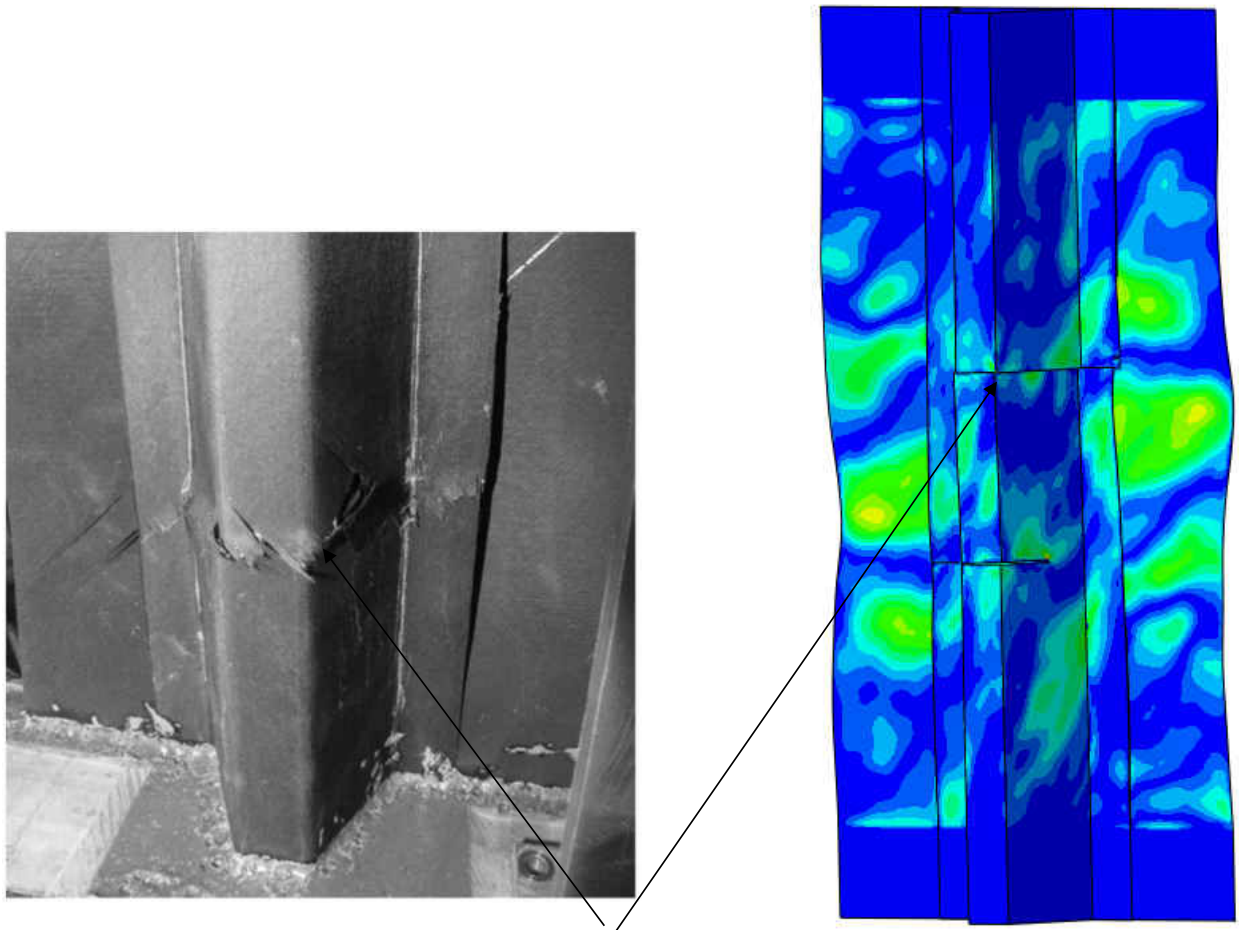
Stringer crippling at 0°

Figure 69: Comparison between experimental and numerical collapse modes of a nominally pristine specimen. The test figure is adopted from (Bisagni et al., 2011)

A comparison between our simulations with the simulation using CDM (continuum damage model) is shown in Figure 70. The simulations are for the nominally pristine specimen. The simulation steps from the 5 loadings of the process are extracted. At point A with applied force around 3kN, no buckling is shown. With increasing force from 7kN to 24kN, buckling is shown in the simulations. When reaching the maximum force around 38kN, severe buckling is shown in both simulations. And in the end, when total failure happens at point E, skin-stringer separation is observed.
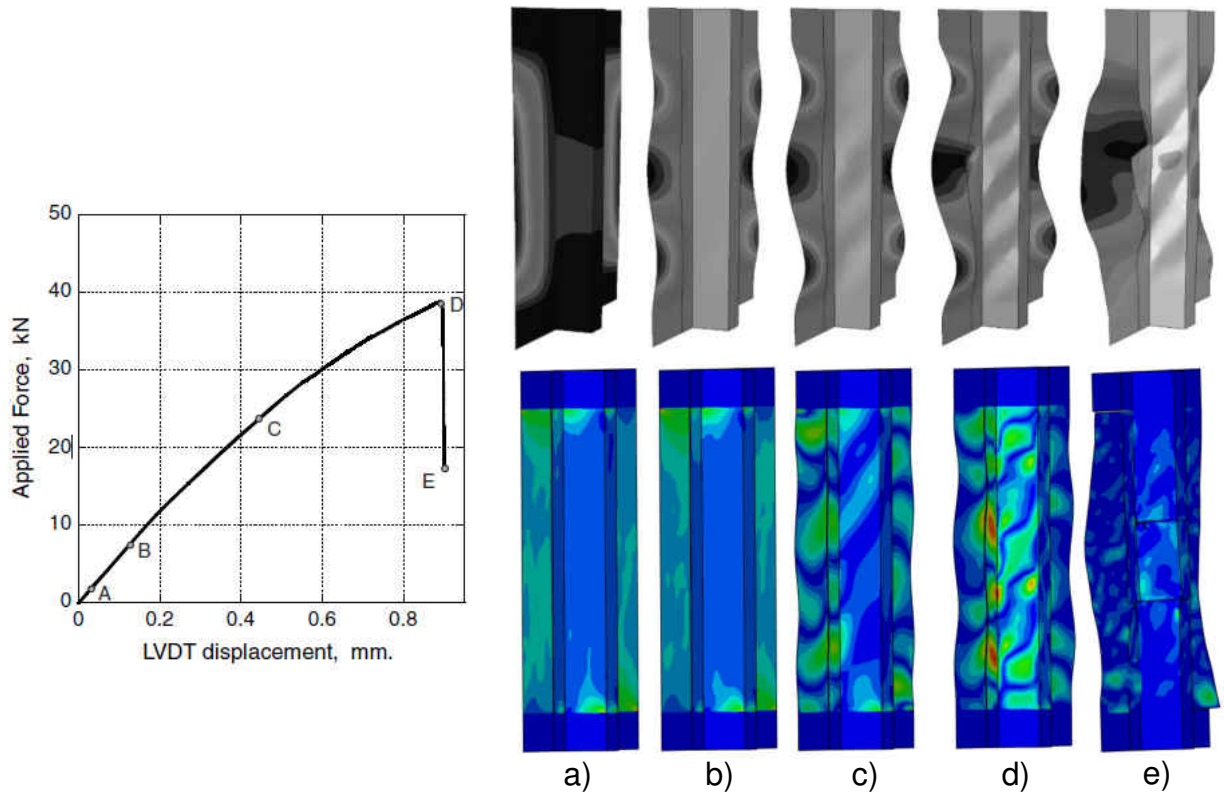
Figure 70: Force-displacement curve of a nominally pristine specimen (left); A comparison between the proposed model results (lower right) and continuum damage model results (upper right) Left and upper right figures are adopted from (Bisagni et al., 2011)

The comparison of the force-displacement curves between experiments and simulation are shown in Figure 71. The left figure are the results from the reference which utilized the continuum damage model. The solid lines are the simulation while the dashed lines are the experiments. The simulation using CDM method capture most of the features of the experimental curves. Like their simulations have similar strength of the pristine specimen and specimen with defect respectively. The slope of the curves are close but not exactly when it goes to higher forces where degradation is severe. In the right figure, the results of our proposed model are shown. Solid lines are the experiments and dashed lines are our simulation results. Our results captures the features better compared with the CDM model. Our proposed model well captured

the slopes of the both curves in all force ranges. In addition, we capture the strength of the specimen with and without defect better. To sum up, our proposed model behaves better in the modeling of the laminates.

Continuum damage model
From reference
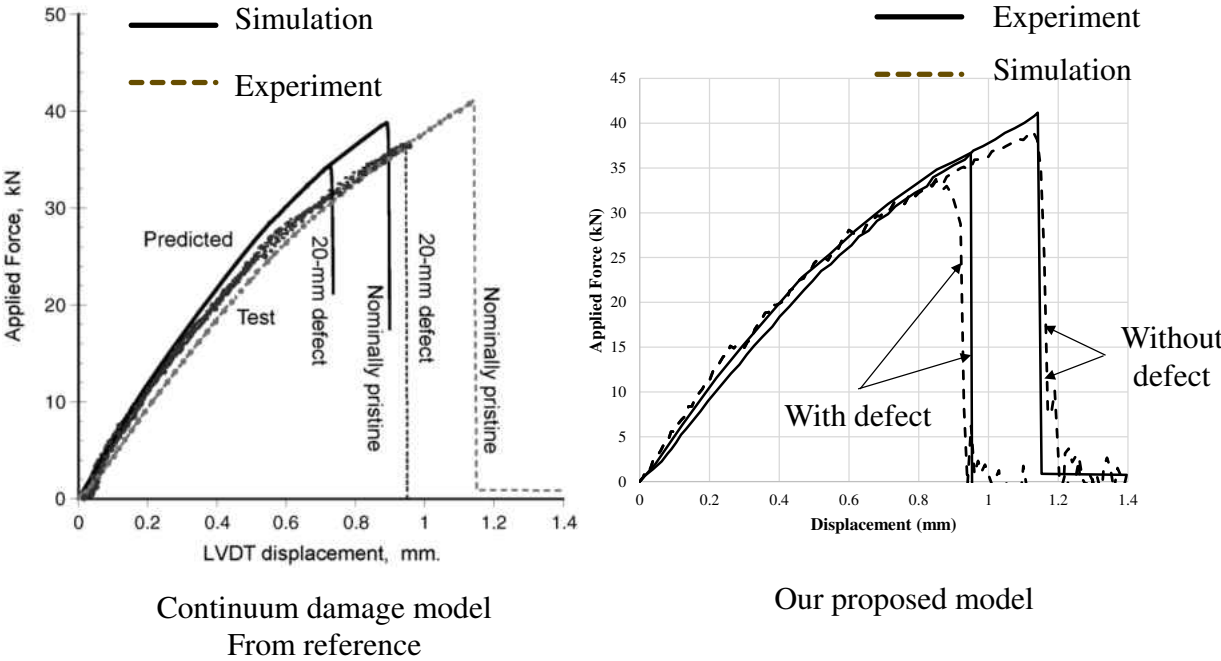
Our proposed model

Figure 71: Comparison between force-displacement curves from experiments and simulation (left) reference (right) our proposed model. The left figure is adopted from (Bisagni et al., 2011).

CHAPTER 8 CONCLUSIONS AND FUTURE STUDIES

8.1 Summary of contribution

A wide range of composite materials have been extensively studied in this dissertation, which include experimental work, analytical study, and numerical simulations. The key contributions can be summarized as follows.

- A comprehensive set of experiments have been done on different composite, including cold drawing of single fiber composite, biaxial loading on polymer matrix composites and multi-loading conditions on metal matrix nano composites. Interesting phenomenon like necking propagation with uniformly chopped nano-rods is found in cold-drawing of single fiber composite as well as thin film composite. A comprehensive set of experiment have been done on unidirectional carbon fiber composites including tensile, compressive, shear, combined tensile and shear and combined compressive and shear loadings. Strong asymmetric behaviors between tension and compression were observed. Material plasticity and material softening are found dependent on loading conditions. Uniaxial compression, three-point bending as well as uniaxial tension loading conditions are applied to metal matrix composites. Asymmetric material property is found in tensile and compressive loading as well.

- A combination of material models including necking propagation model, brittle cracking model and interfacial model are tuned and used to reproduce the interesting necking propagation with uniformly chopped nano-rods phenomenon. Good correlation between experiment and simulation was observed in terms of material hardening and fracture.

- A material modelling framework is proposed for the composite simulation. The framework is composed of elasticity, plasticity, damage initiation, post-failure softening and fracture stages under multiaxial loading conditions and considering their asymmetries. The framework can describe almost all the material behaviors of composite materials. This modeling framework has been applied to polymer matrix composite and metal matrix composite and it can give reasonable predictions for the material studied in this dissertation. And the framework has the potential application for a wide range of composites as well.

- A parameter ψ is proposed to describe the loading condition of unidirectional carbon fiber composites. This parameter can distinguish compression dominate, shear dominate and tension dominate loading conditions which facilitate material modeling in unidirectional fiber reinforced composites and has been applied in the modelling of unidirectional carbon fiber composites in this dissertation.

- The stress-based MMC fracture model is proposed based on the original MMC model proposed by Bai and Wierzbichi in 2010. The proposed model is found to fit better for the fracture locus of metal matrix nano composites.

8.2 Recommended Future Studies

In the present dissertation, a comprehensive set of experiments has been conducted and models have been developed for predicting mechanical behaviors of composite materials. There are several more topics suggested for the future research.

- Investigation of single fiber composite and thin film composite in a micro-scale such as single fiber pullout test. The interfacial material property is essential in determining the behavior of both cladding and core material. Single fiber pullout test could provide the detailed material property of interfacial layer and therefore contribute to the overall material behavior prediction.

- Application of the modelling framework to more composite materials, such as ceramic matrix composites. Composites can be grouped into three categorized including polymer matrix composites, metal matrix composites and ceramic matrix composites. Both polymer matrix composites and metal matrix composites are studied in this dissertation and ceramic matrix composites is the one to be studied.

- Further validation of the modeling framework to laminates with complex configuration of lamina arrangement. A validation of the proposed material modeling framework is conducted on single stringer compression specimen. However, there are more complex configuration of laminate composites like 3D woven composites which are also widely used. To extend the application of the framework, more validation of the proposed framework will help.

- Investigation of the impact loadings on the carbon fiber composites and evaluation the proposed model. Impact loading needs to be studied in applications like automobiles and

121

aircrafts. This loading could cause catastrophic failure of the material and therefore essential in material study.

REFERENCES

ABAQUS. (2011). 6.11. SIMULIA,"User's manual. *Inc. and Dassault Systemes*.

An, L., Qu, J., Luo, J., Fan, Y., Zhang, L., Liu, J., . . . Blau, P. J. (2011). Aluminum nanocomposites having wear resistance better than stainless steel. *J. Mater. Res., 26 (19)*, 2479-2483.

Anand, L., & Gurtin, M. E. (2003). A theory of amorphous solids undergoing large deformations, with application to polymeric glasses. *International Journal of Solids and Structures, 40*(6), 1465-1487.

Arsenault, R. J., & Shi, N. (1986). Dislocation generation due to differences between the coefficients of thermal expansion. *Mater. Sci. \& Eng., 81*, 175-187.

Arsenault, R. J., Wang, L., & Feng, C. R. (1991). Strengthening of composites due to microstructural changes in the matrix. *Acta Mater., 39*, 47-57.

Ashby, M. F. (1971). *Strengthening Methods in Crystals*: Elsevier, Amsterdam.

Azizi, R., Legarth, B. N., & Niordson, C. F. (2013). A new macroscopically anisotropic pressure dependent yield function for metal matrix composite based on strain gradient plasticity for the microstructure. *Journal of the Mechanics and Physics of Solids, 61*(4), 991-1009.

Bagchi, A., Lucas, G., Suo, Z., & Evans, A. (1994). A new procedure for measuring the decohesion energy for thin ductile films on substrates. *Journal of Materials Research, 9*(07), 1734-1741.

Bai, Y., & Wierzbicki, T. (2008). A new model of metal plasticity and fracture with pressure and Lode dependence. *International Journal of Plasticity, 24*, 1071-1096.

Bai, Y., & Wierzbicki, T. (2010). Application of extended Mohr-Coulomb criterion to ductile fracture. *International Journal of Fracture, 161*, 1-20.

Barai, P., & Weng, G. J. (2011). A theory of plasticity for carbon nanotube reinforced composites. *International Journal of Plasticity, 27*(4), 539 - 559.

Barbero, E. J., & Lonetti, P. (2002). An inelastic damage model for fiber reinforced laminates. *Journal of Composite Materials, 36*(8), 941-962.

Beese, A. M., Luo, M., Li, Y., Bai, Y., & Wierzbicki, T. (2010). Partially coupled anisotropic fracture model for aluminum sheets. *Engineering Fracture Mechanics, 77*(7), 1128-1152.

Benzeggagh, M., & Kenane, M. (1996). Measurement of mixed-mode delamination fracture toughness of unidirectional glass/epoxy composites with mixed-mode bending apparatus. *Composites Science and Technology, 56*(4), 439-449.

Berthelot, J.-M. (2012). *Composite materials: mechanical behavior and structural analysis*: Springer Science & Business Media.

Beuth, J., & Klingbeil, N. (1996). Cracking of thin films bonded to elastic-plastic substrates. *Journal of the Mechanics and Physics of Solids, 44*(9), 1411-1428.

Bisagni, C., Vescovini, R., & Dávila, C. G. (2011). Single-stringer compression specimen for the assessment of damage tolerance of postbuckled structures. *Journal of Aircraft, 48*(2), 495.

Bisagni, C., & Walters, C. (2008). Experimental investigation of the damage propagation in composite specimens under biaxial loading. *Composite structures, 85*(4), 293-310.

Brewer, J. C., & Lagace, P. A. (1988). Quadratic stress criterion for initiation of delamination. *Journal of Composite Materials, 22*(12), 1141-1155.

Brown, E., Bray, J., & Santarelli, F. (1989). Influence of stress-dependent elastic moduli on stresses and strains around axisymmetric boreholes. *Rock mechanics and rock engineering, 22*(3), 189-203.

Brünig, M., Gerke, S., & Hagenbrock, V. (2013). Micro-mechanical studies on the effect of the stress triaxiality and the Lode parameter on ductile damage. *International Journal of Plasticity, 50*, 49-65.

Camanho, P. P., Maimí, P., & Dávila, C. (2007). Prediction of size effects in notched laminates using continuum damage mechanics. *Composites Science and Technology, 67*(13), 2715-2727.

Canaday, H. (2015). Composites vs. Metals. *Aerospace America*.

Car, E., Oller, S., & Oñate, E. (2000). An anisotropic elastoplastic constitutive model for large strain analysis of fiber reinforced composite materials. *Computer Methods in Applied Mechanics and Engineering, 185*(2), 245-277.

Cazacu, O. (1999). On the choice of stress-dependent elastic moduli for transversely isotropic solids. *Mechanics research communications, 26*(1), 45-54.

Chawla, K. K. (2006). *Metal matrix composites*: Wiley Online Library.

Chawla, K. K. (2012). *Composite materials: science and engineering*: Springer Science & Business Media.

Chen, B., Hwang, J., Chen, I., Yu, G., & Huang, J.-H. (2000). A tensile-film-cracking model for evaluating interfacial shear strength of elastic film on ductile substrate. *Surface and Coatings Technology, 126*(2), 91-95.

Chen, B., Hwang, J., Yu, G., & Huang, J. (1999). In situ observation of the cracking behavior of TiN coating on 304 stainless steel subjected to tensile strain. *Thin Solid Films, 352*(1), 173-178.

Chen, X., & Liu, Y. (2001). Multiple-cell modeling of fiber-reinforced composites with the presence of interphases using the boundary element method. *Computational Materials Science, 21*(1), 86-94.

Chow, C., & Yang, F. (1997). Three-dimensional inelastic stress analysis of center notched composite laminates with damage. *International Journal of Damage Mechanics, 6*(1), 23-50.

Clough, R. B., & McDonough, W. G. (1996). The measurement of fiber strength parameters in fragmentation tests by using acoustic emission. *Composites Science and Technology, 56*(10), 1119-1127.

Clyne, T. W., & Withers, P. J. (1995). *An Introduction to Metal Matrix Composites*: Cambridge University Press, Cambridge, UK.

Company, T. B. (2008). COMPOSITES IN THE AIRFRAME AND PRIMARY STRUCTURE. Retrieved from http://www.boeing.com/commercial/aeromagazine/articles/qtr_4_06/article_04_2.html

CompositesGroup, T. Advantages of Composites. Retrieved from http://www.premix.com/why-composites/adv-composites.php

Cox, H. (1952). The elasticity and strength of paper and other fibrous materials. *British journal of applied physics, 3*(3), 72.

Djordjević, I. M., Sekulić, D. R., Mitrić, M. N., & Stevanović, M. M. (2010). Non-Hookean elastic behavior and crystallite orientation in carbon fibers. *Journal of Composite Materials*.

Donadon, M. V., De Almeida, S. F. M., Arbelo, M. A., & de Faria, A. R. (2009). A three-dimensional ply failure model for composite structures. *International Journal of Aerospace Engineering, 2009*.

Donaldson, S. (1985). Fracture toughness testing of graphite/epoxy and graphite/PEEK composites. *Composites, 16*(2), 103-112.

Đorđević, I. M., Sekulić, D. R., & Stevanović, M. M. (2007). Non-linear elastic behavior of carbon fibres of different structural and mechanical characteristic. *Journal of the Serbian Chemical Society, 72*(5), 513-521.

Drzal, L. T., & Rich, M. J. (1985). Effect of graphite fiber/epoxy matrix adhesion on composite fracture behavior. *Research Advances in Composites in the United States and Japan, ASTM STP, 864*, 16-26.

Ferkel, H., & Mordike, B. (2001). Magnesium strengthened by SiC nanoparticles. *Materials Science and Engineering: A, 298*(1), 193-199.

Fishman, S. G. (1986). Interfaces in composites. *J. Matels, 38*, 26.

Flom, Y., & Arsenault, R. J. (1985). Deformation in Al-SiC composites due to thermal stresses. *Mater. Sci. \& Eng., 75*, 151-167.

Franklin, H. G. (1968). Classic theories of failure of anisotropic materials. *Fibre Science and Technology, 1*(2), 137-150.

Fraser, W., Ancker, F., DiBenedetto, A., & Elbirli, B. (1983). Evaluation of surface treatments for fibers in composite materials. *Polymer Composites, 4*(4), 238-248.

Fritzen, F., Forest, S., Böhlke, T., Kondo, D., & Kanit, T. (2012). Computational homogenization of elasto-plastic porous metals. *International Journal of Plasticity, 29*, 102-119.

Furuyama, M., Higuchi, M., Kubomura, K., Sunago, H., Jiang, H., & Kumar, S. (1993). Compressive properties of single-filament carbon fibres. *Journal of Materials Science, 28*(6), 1611-1616.

Goyal, V. K., Johnson, E. R., & Davila, C. G. (2004). Irreversible constitutive law for modeling the delamination process using interfacial surface discontinuities. *Composite structures, 65*(3), 289-305.

Gurson, A. L. (1975). *Plastic flow and fracture behavior of ductile materials incorporating void nucleation, growth and interaction.* Brown University.

Gurson, A. L. (1977). Continuum theory of ductile rupture by void nucleation and growth, Part I — Yield criteria and flow rules for porous ductile media. *Journal of Engineering Materials and Technology, 99*, 2-15.

Gustafson, T. W., Panda, P. C., Song, G., & Raj, R. (1997). Influence of microstructural scale on plastic flow behavior of metal matrix composites. *Acta Mater., 45*, 1633-1643.

Habibi, M., Hamouda, A., & Gupta, M. (2012). Enhancing tensile and compressive strength of magnesium using ball milled Al+ CNT reinforcement. *Composites Science and Technology, 72*(2), 290-298.

Hahn, H. (1983). A mixed-mode fracture criterion for composite materials. *Composites Technology Review, 5*(1), 26-29.

Hahn, H., & Johannesson, T. (1984). A correlation between fracture energy and fracture morphology in mixed-mode fracture of composites. *Mechanical behaviour of materials-IV*, 431-438.

Hahn, H. T., & Tsai, S. W. (1973). Nonlinear elastic behavior of unidirectional composite laminae. *Journal of Composite Materials, 7*(1), 102-118.

Hamilton, R., Efstathiou, C., Sehitoglu, H., & Chumlyakov, Y. (2006). Thermal and stress-induced martensitic transformations in NiFeGa single crystals under tension and compression. *Scripta Materialia, 54*(3), 465-469.

Hancock, J. W., & Mackenzie, A. C. (1976). On the mechanisms of ductile failure in high-strength steels subjected to multi-axial stress-states. *Journal of the Mechanics and Physics of Solids, 24*(2-3), 147-160.

Hashemi, S., Kinloch, A., & Williams, J. (1990). The effects of geometry, rate and temperature on the mode I, mode II and mixed-mode I/II interlaminar fracture of carbon-fibre/poly (ether-ether ketone) composites. *Journal of Composite Materials, 24*(9), 918-956.

Hashin, Z. (1980). Failure criteria for unidirectional fiber composites. *Journal of Applied Mechanics, 47*(2), 329-334.

Hashin, Z., & Rotem, A. (1973). A fatigue failure criterion for fiber reinforced materials. *Journal of Composite Materials, 7*(4), 448-464.

Hayakawa, K., Murakami, S., & Liu, Y. (1998). An irreversible thermodynamics theory for elastic-plastic-damage materials. *European Journal of Mechanics-A/Solids, 17*(1), 13-32.

Hesabi, Z. R., Simchi, A., & Reihani, S. M. S. (2006). Structural evolution during mechanical milling of nanometric and micrometric Al2O3 reinforced Al matrix composites. *Mater. Sci. \& Eng., A, 428*, 159-168.

Hillerborg, A., Modéer, M., & Petersson, P.-E. (1976). Analysis of crack formation and crack growth in concrete by means of fracture mechanics and finite elements. *Cement and concrete research, 6*(6), 773-781.

Hinton, M., Kaddour, A., & Soden, P. (2002). A comparison of the predictive capabilities of current failure theories for composite laminates, judged against experimental evidence. *Composites Science and Technology, 62*(12), 1725-1797.

Hinton, M. J., Kaddour, A. S., & Soden, P. D. (2004). *Failure criteria in fibre reinforced polymer composites: the world-wide failure exercise*: Elsevier.

Hoffman, O. (1967). The brittle strength of orthotropic materials. *Journal of Composite Materials, 1*(2), 200-206.

Hong, S. J., Kim, H. M., Huh, D., Suryanarayana, C., & Chun, B. S. (2003). Effect of clustering on the mechanical properties of SiC particulate-reinforced aluminum alloy 2024 metal matrix composites. *Mater. Sci. \& Eng. A, 347*, 198-204.

Hui, C., Shia, D., & Berglund, L. (1999). Estimation of interfacial shear strength: an application of a new statistical theory for single fiber composite test. *Composites Science and Technology, 59*(13), 2037-2046.

Ibrahim, I. A., Mohamed, F. A., & Lavernia, E. J. (1991). Particle reinforced metal matrix composites - A review. *J. Mater. Sci., 26*, 1137-1156.

Ibrahim, I. A., Mohamed, F. A., & Lavernia, E. J. (1991). Particulate reinforced metal matrix composites - a review. *Journal of Materials Science, 26*, 1137-1156.

Jambor, A., & Beyer, M. (1997). New cars—new materials. *Materials & Design, 18*(4), 203-209.

Jarausch, K., Kiely, J., Houston, J. E., & Russell, P. (2000). Defect-dependent elasticity: nanoindentation as a probe of stress state. *Journal of Materials Research, 15*(08), 1693-1701.

Jia, Y., & Bai, Y. (2016a). Ductile fracture prediction for metal sheets using all-strain-based anisotropic eMMC model. *International Journal of Mechanical Sciences, 115*, 516-531.

Jia, Y., & Bai, Y. (2016b). Experimental study on the mechanical properties of AZ31B-H24 magnesium alloy sheets under various loading conditions. *International Journal of Fracture, 197*(1), 25-48.

Jia, Y., Long, X., Wang, K., & Bai, Y. (2013). *Calibration of plasticity and fracture of magnesium alloy sheets under biaxial loading conditions.* Paper presented at the International Symposium on Plasticity and its Current Applications, Bahamas.

Johnson, A., Hayes, S., & Jones, F. (2005). An improved model including plasticity for the prediction of the stress in fibres with an interface/interphase region. *Composites Part A: Applied Science and Manufacturing, 36*(2), 263-271.

Johnson, G. R., & Cook, W. H. (1985). Fracture characteristics of three metals subjected to various strains, strain rates, temperatures and pressures. *Engineering Fracture Mechanics, 21*(1), 31-48.

Jones, R. M. (1977). Stress-strain relations for materials with different moduli in tension and compression. *AIAA Journal, 15*(1), 16-23.

Kachanov, L. (1958). Time of the rupture process under creep conditions. *Isv. Akad. Nauk. SSR. Otd Tekh. Nauk, 8*, 26-31.

Kamat, S. V., Rollett, A. D., & Hirth, J. P. (1991). Plastic-deformation in Al-alloy matrix-alumina particulate composites. *Scripta Metall. Mater., 25*, 27-32.

Kang, Y., & Chan, S. L. I. (2004). Tensile properties of nanometric Al2O3 particle-reinforced aluminum matrix composites. *Mater. Chem. Phys., 85*, 438-443.

Kim, J.-Y., Jang, D., & Greer, J. R. (2012). Crystallographic orientation and size dependence of tension–compression asymmetry in molybdenum nano-pillars. *International Journal of Plasticity, 28*(1), 46-52.

Kim, K. T., Cha, S. I., Hong, S. H., & Hong, S. H. (2006). Microstructures and tensile behavior of carbon nanotube reinforced Cu matrix nanocomposites. *Materials Science and Engineering: A, 430*(1â€“2), 27 - 33.

Kim, K. T., Eckert, J., Menzel, S. B., Gemming, T., & Hong, S. H. (2008). Grain refinement assisted strengthening of carbon nanotube reinforced copper matrix nanocomposites. *Applied Physics Letters, 92*(12), 121901 -121901-121903.

Kouzeli, M., & Mortensen, A. (2002). Size dependent strengthening in particle reinforced aluminum. *Acta Mater., 50*, 39-51.

Kouzeli, M., Weber, L., Marchi, C. S., & Mortensen, A. (2001). Quantification of microdamage phenomena during tensile straining of high volume fraction particle reinforced aluminum. *Acta Mater., 49*, 497-505.

Kwon, Y., & Liu, C. (1997). Study of damage evolution in composites using damage mechanics and micromechanics. *Composite structures, 38*(1), 133-139.

Lecarme, L., Tekog, C., & Pardoen, T. (2011). Void growth and coalescence in ductile solids with stage III and stage IV strain hardening. *International Journal of Plasticity, 27*(8), 1203-1223.

Lee, J. D. (1982). Three dimensional finite element analysis of damage accumulation in composite laminate *Fracture of Composite Materials* (pp. 291-306): Springer.

Lei, X., & Lissenden, C. J. (2007). Pressure Sensitive Nonassociative Plasticity Model for DRA Composites. *Journal of Engineering Materials and Technology, 129*(2), 255-264.

Li, H., Fu, M., Lu, J., & Yang, H. (2011). Ductile fracture: experiments and computations. *International Journal of Plasticity, 27*(2), 147-180.

Li, T., Huang, Z., Xi, Z., Lacour, S. P., Wagner, S., & Suo, Z. (2005). Delocalizing strain in a thin metal film on a polymer substrate. *Mechanics of Materials, 37*(2), 261-273.

Li, T., & Suo, Z. (2007). Ductility of thin metal films on polymer substrates modulated by interfacial adhesion. *International Journal of Solids and Structures, 44*(6), 1696-1705.

Li, X., Yang, Y., & Weiss, D. (2008). Theoretical and experimental study on ultrasonic dispersion of nanoparticles for strengthening cast aluminum alloy A356. *Metal. Sci. Tech., 26(2)*, 12-20.

Li, Y., Luo, M., Gerlach, J., & Wierzbicki, T. (2010). Prediction of shear-induced fracture in sheet metal forming. *Journal of Materials Processing Technology, 210*(14), 1858-1869.

Li, Y., Ramesh, K. T., & Chin, E. S. C. (2000). The compressive viscoplastic response of an A359/SiCp metal-matrix composite and of the A359 aluminum alloy matrix. *International Journal of Solids and Structures, 37*(51), 7547 - 7562.

Li, Y., Ramesh, K. T., & Chin, E. S. C. (2004). Comparison of the plastic deformation and failure of A359/SiC and 6061-T6/Al2O3 metal matrix composites under dynamic tension. *Materials Science and Engineering: A, 371*(1â€"2), 359 - 370.

Li, Y., Wierzbicki, T., Sutton, M., Yan, J., & Deng, X. (2011). Mixed mode stable tearing of thin sheetÂ AI 6061-T6 specimens: experimental measurements and finite element simulations using a modified Mohr-Coulomb fracture criterion. *International Journal of Fracture, 168*, 53-71.

Lin, W.-P., & Hu, H.-T. (2002). Nonlinear analysis of fiber-reinforced composite laminates subjected to uniaxial tensile load. *Journal of Composite Materials, 36*(12), 1429-1450.

Liu, P., & Zheng, J. (2010). Recent developments on damage modeling and finite element analysis for composite laminates: a review. *Materials & Design, 31*(8), 3825-3834.

Liu, Y., Xu, N., & Luo, J. (2000). Modeling of interphases in fiber-reinforced composites under transverse loading using the boundary element method. *Journal of Applied Mechanics, 67*(1), 41-49.

Lloyd, D. J. (1994). Particle reinforced aluminium and magnesium matrix composites. *International Materials Reviews, 39 (1).*

Lonetti, P., Barbero, E. J., Zinno, R., & Greco, F. (2004). Interlaminar Damage Model for Polymer Matrix Composites. *Journal of Composite Materials, 38*(9), 799-800.

Long, X., Bai, Y., Algarni, M., Choi, Y., & Chen, Q. (2015). Study on the strengthening mechanisms of Cu/CNT nano-composites. *Materials Science and Engineering: A, 645*, 347-356.

Lu, N., Suo, Z., & Vlassak, J. J. (2010). The effect of film thickness on the failure strain of polymer-supported metal films. *Acta Materialia, 58*(5), 1679-1687.

Luo, M., Dunand, M., & Mohr, D. (2012). Experiments and modeling of anisotropic aluminum extrusions under multi-axial loading – Part II: Ductile fracture. *International Journal of Plasticity, 32–33*(0), 36-58. doi:http://dx.doi.org/10.1016/j.ijplas.2011.11.001

Luo, M., & Wierzbicki, T. (2010). Numerical failure analysis of a stretch-bending test on dual-phase steel sheets using a phenomenological fracture model. *International Journal of Solids and Structures, 47*(22-23), 3084 - 3102.

Maa, R.-H., & Cheng, J.-H. (2002). A CDM-based failure model for predicting strength of notched composite laminates. *Composites Part B: Engineering, 33*(6), 479-489.

Maimí, P., Camanho, P. P., Mayugo, J., & Dávila, C. (2007). A continuum damage model for composite laminates: Part I–Constitutive model. *Mechanics of Materials, 39*(10), 897-908.

Malcher, L., Pires, F. A., & De Sá, J. C. (2014). An extended GTN model for ductile fracture under high and low stress triaxiality. *International Journal of Plasticity, 54*, 193-228.

Manoharan, M., Lim, S., & Gupta, M. (2002). Application of a model for the work hardening behavior to Mg/SiC composites synthesized using a fluxless casting process. *Materials Science and Engineering: A, 333*(1), 243-249.

Matzenmiller, A., Lubliner, J., & Taylor, R. (1995). A constitutive model for anisotropic damage in fiber-composites. *Mechanics of Materials, 20*(2), 125-152.

McClintock, F. A. (1968). A criterion of ductile fracture by the growth of holes. *Journal of Applied Mechanics, 35*, 363-371.

Melanitis, N., Tetlow, P., Galiotis, C., & Smith, S. (1994). Compressional behaviour of carbon fibres. *Journal of Materials Science, 29*(3), 786-799.

Milan, M., & Bowen, P. (2004). Tensile and fracture toughness properties of SiCp reinforced Al alloys: Effects of particle size, particle volume fraction, and matrix strength. *Journal of materials engineering and performance, 13*(6), 775-783.

Miracle, D. B. (2005). Metal matrix composites- From science to technological significance. *Composites Science and Technology, 65*(15â€"16), 2526 - 2540.

Mises, R. v. (1913). Gottinger Nachrichten. *Math.Phys.Klasse*, 582.

Mortensen, A., & Llorca, J. (2010). Metal Matrix Composites. *Annual Review of Materials Research, 40*, 243-270.

Mula, S., Padhi, P., Panigrahi, S. C., Pabi, S. K., & Ghosh, S. (2009). On structure and mechanical properties of ultrasonically cast Al-2%Al2O3 nanocomposites. *Mater. Res. Bull, 44*, 1154-1160.

Mummery, P., & Derby, B. (1991). The Influence of microstructure on the fracture behavior of particulate metal matrix composites. *Mater. Sci. \& Eng., A, 135*, 221-224.

Murakami, S., & Kamiya, K. (1997). Constitutive and damage evolution equations of elastic-brittle materials based on irreversible thermodynamics. *International Journal of Mechanical Sciences, 39*(4), 473-486.

Nan, C. W., & Clarke, D. R. (1996). The influence of particle size and particle fracture on the elastic/plastic deformation of metal matrix composites. *Acta Mater., 44*, 3801-3811.

Netravali, A., Henstenburg, R., Phoenix, S., & Schwartz, P. (1989). Interfacial shear strength studies using the single‐filament‐composite test. I: Experiments on graphite fibers in epoxy. *Polymer Composites, 10*(4), 226-241.

Netravali, A., Schwartz, P., & Phoenix, S. (1989). Study of interfaces of high‐performance glass fibers and DGEBA‐based epoxy resins using single‐fiber‐composite test. *Polymer Composites, 10*(6), 385-388.

Ohsawa, T., Nakayama, A., Miwa, M., & Hasegawa, A. (1978). Temperature dependence of critical fiber length for glass fiber‐reinforced thermosetting resins. *Journal of Applied Polymer Science, 22*(11), 3203-3212.

Okabe, T., Takeda, N., Kamoshida, Y., Shimizu, M., & Curtin, W. (2001). A 3D shear-lag model considering micro-damage and statistical strength prediction of unidirectional fiber-reinforced composites. *Composites Science and Technology, 61*(12), 1773-1787.

Olsson, M., & Ristinmaa, M. (2003). Damage evolution in elasto-plastic materials-material response due to different concepts. *International Journal of Damage Mechanics, 12*(2), 115-139.

Orifici, A., Herszberg, I., & Thomson, R. (2008). Review of methodologies for composite material modelling incorporating failure. *Composite Structures, 86*(1), 194-210.

Pinho, S., Iannucci, L., & Robinson, P. (2006). Physically based failure models and criteria for laminated fibre-reinforced composites with emphasis on fibre kinking. Part II: FE implementation. *Composites Part A: Applied Science and Manufacturing, 37*(5), 766-777.

Pozdnyakova, I., Bruno, G., Efremov, A. M., Clausen, B., & Hughes, D. (2009). Stress‐Dependent Elastic Properties of Porous Microcracked Ceramics. *Advanced Engineering Materials, 11*(12), 1023-1029.

Prabhu, B., Suryanarayana, C., An, L., & Vaidyanathan, R. (2006). Synthesis and characterization of high volume fraction Al-Al2O3 nanocomposite powders by high-energy milling. *Mater. Sci. Eng. A-Structural Materials Properties, Microstructure and Processing, 425*, 192-200.

Prangnell, P. B., Downes, T., Stobbs, W. M., & Withers, P. J. (1994). The deformation of discontinuously reinforced MMCs – I. The initial yielding behavior. *Acta Mater., 10*, 3425-3436.

Puck, A., & W, S. (1969). On failure mechanisms and failure criteria of filament-wound glass-fibre/resin composites. *Plastics & Polymers, 37*(127), 33-&.

Ran, J., Fu, M., & Chan, W. (2013). The influence of size effect on the ductile fracture in micro-scaled plastic deformation. *International Journal of Plasticity, 41*, 65-81.

Ravichandran, K. S. (1994). A simple model of deformation behavior of two phase composites. *Acta Metall. Mater., 42*, 1113-1123.

Rice, J. R., & Tracey, D. M. (1969). On the ductile enlargement of voids in triaxial stress fields. *Journal of the Mechanics and Physics of Solids, 17*, 201-217.

Saravanan, R., & Surappa, M. (2000). Fabrication and characterisation of pure magnesium-30 vol.% SiC P particle composite. *Materials Science and Engineering: A, 276*(1), 108-116.

Schapery, R. (1990). A theory of mechanical behavior of elastic media with growing damage and other changes in structure. *Journal of the Mechanics and Physics of Solids, 38*(2), 215-253.

Schipperen, J. (2001). An anisotropic damage model for the description of transverse matrix cracking in a graphite–epoxy laminate. *Composite structures, 53*(3), 295-299.

Schleicher, F. (1926). Der spannonggszustand and der flieffgrenze plastizitatsbedingqung. *Z. Angew. Math. Mech., 6*, 199–216.

Shao, J., Xiao, B., Wang, Q., Ma, Z., & Yang, K. (2011). An enhanced FEM model for particle size dependent flow strengthening and interface damage in particle reinforced metal matrix composites. *Composites Science and Technology, 71*(1), 39-45.

Shen, J., Yin, W., Wei, Q., Li, Y., Liu, J., & An, L. (2013). Effect of ceramic nanoparticle reinforcements on the quasistatic and dynamic mechanical properties of magnesium-based metal matrix composites. *Journal of Materials Research, 28*(13), 1835-1852.

Shi, N., & Arsenault, R. J. (1994). Plastic-flow In SiC/Al composites – strengthening and ductility. *Ann. Rev. Mater. Sci., 24*, 321-357.

Shia, D., Hui, C., & Phoenix, S. (2000). Statistics of fragmentation in a single-fiber composite under matrix yielding and debonding with application to the strength of multi-fiber composites. *Composites Science and Technology, 60*(11), 2107-2128.

Shioya, M., & Takaku, A. (1995). Estimation of fibre and interfacial shear strength by using a single-fibre composite. *Composites Science and Technology, 55*(1), 33-39.

Sun, C., & Chen, J. (1989). A simple flow rule for characterizing nonlinear behavior of fiber composites. *Journal of Composite Materials, 23*(10), 1009-1020.

Suresh, S. (2013). *Fundamentals of metal-matrix composites*: Elsevier.

Tang, F., Hagiwara, M., & Schoenung, J. M. (2005). Microstructure and tensile properties of bulk nanostructured Al-5083/SiCp composites prepared by cryomilling. *Mater. Sci. Eng., 407*, 306-314.

Tong, L. (1997). An assessment of failure criteria to predict the strength of adhesively bonded composite double lap joints. *Journal of Reinforced Plastics and Composites, 16*(8), 698-713.

Tsai, S. W. (1968). Strength theories of filamentary structures. *Fundamental aspects of fiber reinforced plastic composites*, 3-11.

Tsai, S. W., & Hahn, H. T. (1981). Introduction to composite materials, 1980. *Lancaster, Pennsylvania, Technomic, 453*.

Tsai, S. W., & Wu, E. M. (1971). A general theory of strength for anisotropic materials. *Journal of Composite Materials, 5*(1), 58-80.

Tvergaard, V. (1989). Material Failure by Void Growth to Coalescence. In J. W. Hutchinson & T. Y. Wu (Eds.), (Vol. Volume 27, pp. 83-151): Elsevier.

Tvergaard, V., & Hutchinson, J. W. (2002). Two mechanisms of ductile fracture: void by void growth versus multiple void interaction. *International Journal of Solids and Structures, 39*(13-14), 3581-3597.

Tvergaard, V., & Needleman, A. (1984). Analysis of the cup-cone fracture in a round tensile bar. *Acta Materialia, 32*, 157-169.

van Dreumel, W. (1982). *A short note on the compressive behaviour of aramid fibre reinforced plastics*. Retrieved from

Van Dreumel, W. H., & Kamp, J. L. (1977). *Non Hookean behaviour in the fibre direction of carbonfibre composites and the influence of fibre waviness on the tensile properties*. Retrieved from

Varna, J., Joffe, R., & Berglund, L. A. (1996). Interfacial toughness evaluation from the single-fiber fragmentation test. *Composites Science and Technology, 56*(9), 1105-1109.

Vasudevan, A. K., Richmond, O., Zok, F., & Embury, J. D. (1989). The influence of hydrostatic pressure on the ductility of Al-SiC composites. *Materials Science and Engineering: A, 107*(0), 63 - 69.

Vaziri, R., Olson, M., & Anderson, D. (1991). A plasticity-based constitutive model for fibre-reinforced composite laminates. *Journal of Composite Materials, 25*(5), 512-535.

Volinsky, A., Moody, N., & Gerberich, W. (2002). Interfacial toughness measurements for thin films on substrates. *Acta Materialia, 50*(3), 441-466.

Vyas, G., Pinho, S., & Robinson, P. (2011). Constitutive modelling of fibre-reinforced composites with unidirectional plies using a plasticity-based approach. *Composites Science and Technology, 71*(8), 1068-1074.

Wang, X., Jiang, M., Zhou, Z., Gou, J., & Hui, D. (2017). 3D printing of polymer matrix composites: a review and prospective. *Composites Part B: Engineering, 110*, 442-458.

Wang, X., Sparkman, J., & Gou, J. (2017). Electrical actuation and shape memory behavior of polyurethane composites incorporated with printed carbon nanotube layers. *Composites Science and Technology, 141*, 8-15.

wang, x., xu, x., Zhou, Z., & Gou, J. (2017). Shape Memory Polymer Composite Coatings with Enhanced Mechanical and Antimicrobial Properties. *Pigment & Resin Technology*(just-accepted), 00-00.

Wu, J. M., & Li, Z. Z. (2000). Nanostructured composites obtained by mechanically driven reduction reaction of CuO and Al powder mixture. *J. Alloys and Compounds, 299*, 9-16.

Xiang, Y., Li, T., Suo, Z., & Vlassak, J. J. (2005). High ductility of a metal film adherent on a polymer substrate. *Applied Physics Letters, 87*(16), 161910.

Xie, M., & Adams, D. F. (1995). A plasticity model for unidirectional composite materials and its applications in modeling composites testing. *Composites Science and Technology, 54*(1), 11-21.

Xu, Q., & Qu, S. (2015). Irreversible deformation of metal matrix composites: A study via the mechanism-based cohesive zone model. *Mechanics of Materials, 89*, 72-84.

Yamada, S., & Sun, C. (1978). Analysis of laminate strength and its distribution. *Journal of Composite Materials, 12*(3), 275-284.

Yanaka, M., Tsukahara, Y., Nakaso, N., & Takeda, N. (1998). Cracking phenomena of brittle films in nanostructure composites analysed by a modified shear lag model with residual strain. *Journal of Materials Science, 33*(8), 2111-2119.

Yang, Y., Lan, J., & Li, X. (2004). Study on bulk aluminum matrix nanocomposite fabricated by ultrasonic dispersion of nano-sized SiC particles in molten aluminum alloy. *Mater. Sci. \& Eng., A, 380*, 378-383.

Yang, Y., & Li, X. (2007). Ultrasonic cavitation-based nanomanufacturing of bulk aluminum matrix nanocomposites. *Trans. ASME, 129*, 252-255.

Yar, A. A., Montazerian, M., Abdizadeh, H., & Baharvandi, H. R. (2009). Microstructure and mechanical properties of aluminum alloy matrix composite reinforced with nano-particle MgO. *J. Alloys. Comp., 484*, 400-404.

Yu, S., & Dakoulas, P. (1993). General stress-dependent elastic moduli for cross-anisotropic soils. *Journal of geotechnical engineering, 119*(10), 1568-1586.

Yuan, M., Yang, Y., Li, C., Heng, P., & Li, L. (2012). Numerical analysis of the stress–strain distributions in the particle reinforced metal matrix composite SiC/6064Al. *Materials & Design, 38*, 1-6.

Zhandarov, S., Pisanova, E., & Dovgyalo, V. (1992). Measurement of fiber-matrix adhesion by testing single-fiber composites. *Mekhanika Kompozitnykh Materialov, 3*, 384-403.

Zhang, H., Maljkovic, N., & Mitchell, B. S. (2002). Structure and interfacial properties of nanocrystalline aluminum/mullite composites. *Mater. Sci. \& Eng., A, 326*, 317-323.

Zhang, H., Ramesh, K. T., & Chin, E. S. C. (2005). Effects of interfacial debonding on the rate-dependent response of metal matrix composites. *Acta Materialia, 53*(17), 4687 - 4700.

Zhang, H., Ramesh, K. T., & Chin, E. S. C. (2008). A multi-axial constitutive model for metal matrix composites. *Journal of the Mechanics and Physics of Solids, 56*(10), 2972 - 2983.

Zhang, Z., & Li, T. (2008). Effects of grain boundary adhesion and grain size on ductility of thin metal films on polymer substrates. *Scripta Materialia, 59*(8), 862-865.